Mechanical Behavior of Al-SiC Nanolaminate Composites

Using Micro-Scale Testing Methods

by

Carl Randolph Mayer

A Dissertation Presented in Partial Fulfillment
of the Requirements for the Degree
Doctor of Philosophy

Approved April 2016 by the
Graduate Supervisory Committee:

Nikhilesh Chawla, Chair
Hanqing Jiang
Jon Molina-Aldareguia
Jagannathan Rajagopalan

ARIZONA STATE UNIVERSITY

May 2016

ABSTRACT

Nanolaminate composite materials consist of alternating layers of materials at the nanoscale (≤100 nm). Due to the nanometer scale thickness of their layers, these materials display unique and tailorable properties. This enables us to alter both mechanical attributes such as strength and wear properties, as well as functional characteristics such as biocompatibility, optical, and electronic properties. This dissertation focuses on understanding the mechanical behavior of the Al-SiC system. From a practical perspective, these materials exhibit a combination of high toughness and strength which is attractive for many applications. Scientifically, these materials are interesting due to the large elastic modulus mismatch between the layers. This, paired with the small layer thickness, allows a unique opportunity for scientists to study the plastic deformation of metals under extreme amounts of constraint.

Previous studies are limited in scope and a more diverse range of mechanical characterization is required to understand both the advantages and limitations of these materials. One of the major challenges with testing these materials is that they are only able to be made in thicknesses on the order of micrometers so the testing methods are limited to small volume techniques. This work makes use of both microscale testing techniques from the literature as well as novel methodologies. Using these techniques we are able to gain insight into aspects of the material's mechanical behavior such as the effects of layer orientation, flaw dependent fracture, tension-compression asymmetry, fracture toughness as a function of layer thickness, and shear behavior as a function of layer thickness.

i

ACKNOWLEDGMENTS

TABLE OF CONTENTS

LIST OF TABLES

LIST OF FIGURES

viii

CHAPTER 1

INTRODUCTION

The purpose of this research is to explore the mechanical properties of a relatively new

class of nanoscale composite materials. Composites are materials which consist of a

blend of at least two chemically and physically distinct phases, which when used

together, can achieve higher performance than either of the individual constituents. This

approach is commonly seen at the bulk scale in systems such as glass or carbon fibers

embedded in epoxy resins or silicon carbide particles embedded in aluminum. Since

reducing the size of materials to the nanoscale can be used to increase the strength

compared to their bulk counterparts (eg. Carbon nanotubes are many times stronger than

carbon fibers), incorporating nanoscale components into composite materials is a

promising method for obtaining ultra-high performance materials.

Laminate composites are utilized across length scales in both natural composites, such as

geological fomations and abalone shells, and engineered composites, such as aerospace

and nanolaminate composites, as shown in Figure 1. The particular nanoscale composite

this work focuses on consists of alternating thin layers (10-100 nm) of aluminum and

silicon carbide. When paired together, the strength and stiffness of silicon carbide

combined with the toughness of aluminum allow for an attractive mix of strength,

damage tolerance and wear properties. However, one of the downsides of these materials

is that the current fabrication process is very time intensive, which limits the overall

thickness to around 0.01-0.02 mm. While this thickness could still be useful and relevant

as a coating material for cutting tools or other applications, it makes traditional methods

for determining the strength and other mechanical properties impossible to implement.
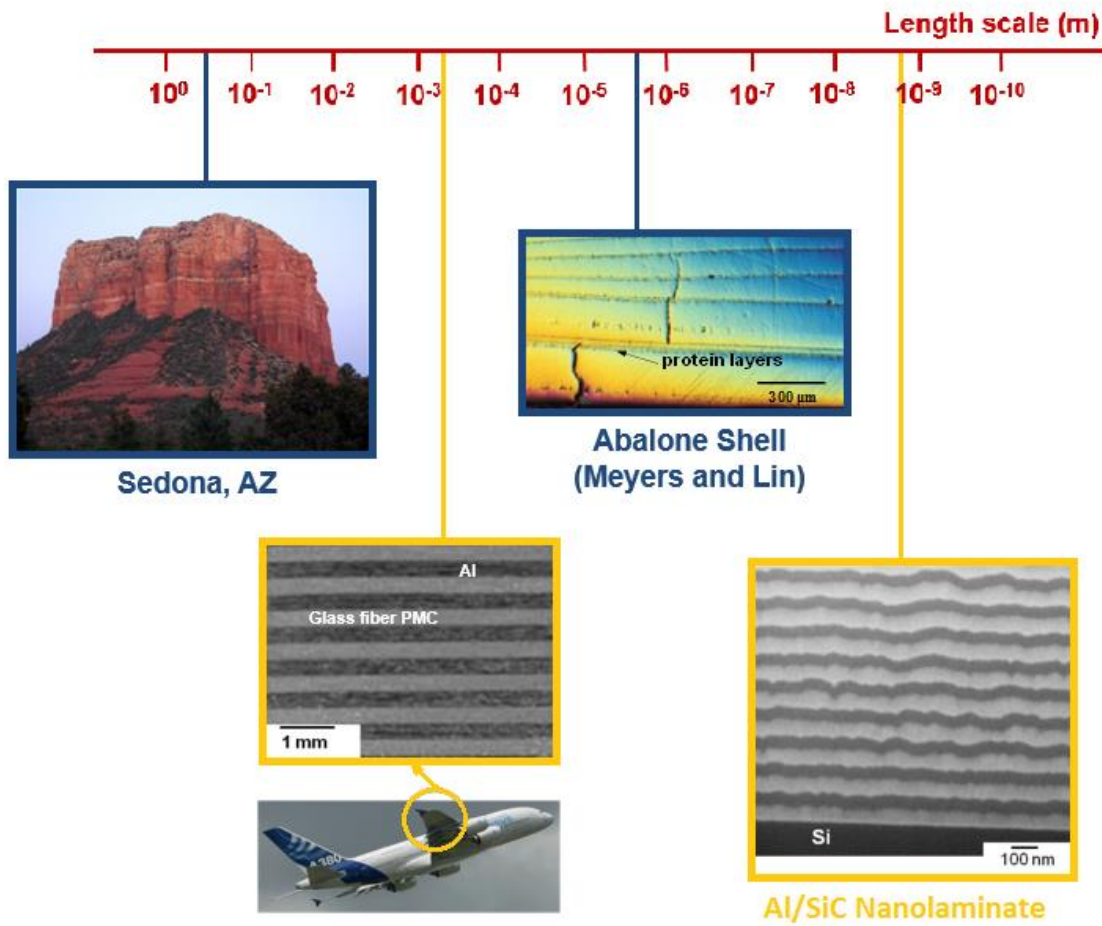
Figure 1. Examples of natural and manmade laminate composite structures over a wide range of length scales (after Chawla, 2008).

This limitation restricts the types of strength measurements we can perform to what is known as micromechanical testing. This type of test is specifically aimed at determining mechanical properties from very small volumes of material. These techniques range in complexity from simply pushing a sharp pyramid into a flat surface while measuring the load and displacement to applying loads to fairly complex geometries to induce a particular stress state. Using these methods we have been able to answer many of the questions about the mechanical properties of this material system including:

- How the strength differs under various loading conditions such as compression, tension, and shear

- How the orientation of the layers affects the mechanical properties

- What is the toughness and flaw tolerance of the material

- How the nanostructure affects the mechanical response of the material

By implementing a range of different types of micromechanical tests on a single material system, as done in this work, valuable information is also provided about the testing methods themselves. By comparing the results, we are able to identify some of the limitations and accuracy of these methods, which helps to give confidence to other research using the same techniques on other materials.

CHAPTER 2

LITERATURE REVIEW

There is an ever growing body of research on both nanolaminate composites as well as micro-scale testing techniques. A review of the most pertinent studies are provided in the following sections as background.

2.1 Nanolaminate Materials

Nanolaminate composites, defined as a composite consisting of dissimilar layers of materials having individual layer thicknesses on the order of nanometers, have become an area of interest in many avenues of materials research due to their unique properties, which are distinct from their macroscale counterparts. These avenues include electronics applications, where their observed giant magneto-resistance behavior can be taken advantage of (Daughton et al., 1994), optical applications, where the x-ray reflectivity is able to be enhanced and tailored according to wavelength (Stearns et al., 1993), and biomedical applications, where the nanolaminate's improved biocompatibility can allow the implantation of devices into the harsh environments found inside the body (Li et al., 2010). This work however, is concerned with the implications of these nanostructures on the mechanical behavior of nanolaminates. Improvement of the mechanical properties in these types of materials compared to the bulk has been observed in a wide range of material combinations, where increases in strength (Lotfian et al., 2012, Singh et al., 2010b), hardness (Chawla et al., 2008, Wu et al., 2006), toughness (Wiklund et al., 1997), and wear resistance (Martinez et al., 2003, Singh and Chawla, 2012) have been observed.

Due to the range of material systems accessible through thin film deposition processes, a wide array of material combinations have utilized this type of nanostructure in the hopes of improving various properties. These include:

- Metal-metal systems (Abadias et al., 2007, Carpenter et al., 2012, Chen et al., 2012, Han et al., 2014, Li et al., 2012, Li et al., , Lloyd and Molina-Aldareguia, 2003, Mara et al., 2008, Misra et al., 2005, Misra et al., 2004, Shingu et al., 2001, Wang and Misra, 2011, Was and Foecke, 1996),

- Metal-ceramic systems (Abadias et al., 2007, Bhattacharyya et al., 2011, Chawla et al., 2008, Deng et al., 2005, Martinez et al., 2003, Jamison and Shen, 2015, Lotfian et al., 2012, Lotfian et al., 2013, Lotfian et al., 2014, Lotfian, 2014, Romero et al., 2004, Singh and Chawla, 2012, Singh et al., 2010c, Singh et al., 2010a, Singh et al., 2010b, Sun et al., 2010, Tang et al., 2008, Tang et al., 2010a, Tang et al., 2010b, Verma and Jayaram, 2014, Wu et al., 2006),

- Ceramic-ceramic systems (Barshilia et al., 2005, Chu and Barnett, 1995, Freyman and Chung, 2008, Helmersson et al., 1987, Holleck et al., 1990, Lloyd and Molina-Aldareguia, 2003, Schlogl et al., 2013, Shinn et al., 1992, Wiklund et al., 1997, Wolfe et al., 2002, Yashar et al., 1999, Zhang et al., 2013a)

As the material system of interest in this work is a metal-ceramic combination, insights can be drawn from the wide range of studies focusing on metal-metal and ceramic-ceramic systems as well. Unfortunately, a consistent terminology for these materials has not yet been adopted in the literature. These materials have been referred as nanolaminates predominantly in the metal-ceramic literature, nanoscale multilayers

predominantly in the metal-metal literature, and superlattices in some of the early ceramic-ceramic literature.

The strengthening of metal-ceramic nanolaminates can be attributed to three main considerations. The first of these relates to the metallic layers, namely the changes in deformation mechanisms which occur as the layer thickness and grain size decrease. The second of these is the fact that the interface acts as a barrier to both dislocations brittle crack propogation through the layers. Finally there is also strengthening due to the constraint imposed on the compliant metallic layers by the stiff ceramic layers.

The deformation mechanisms in the metallic layers change as a function of layer thickness, yielding a nonlinear dependence of strength on layer thickness. A schematic representation of the strength and mechanisms as a function of layer thickness are shown in Figure 2 (Wang and Misra, 2011). Works by Wang, Misra, and others (Wang and Misra, 2011, Misra et al., 2005) detail these changes in mechanism for the Cu-Nb system, but the results are applicable to the metallic phase of the metal-ceramic systems.
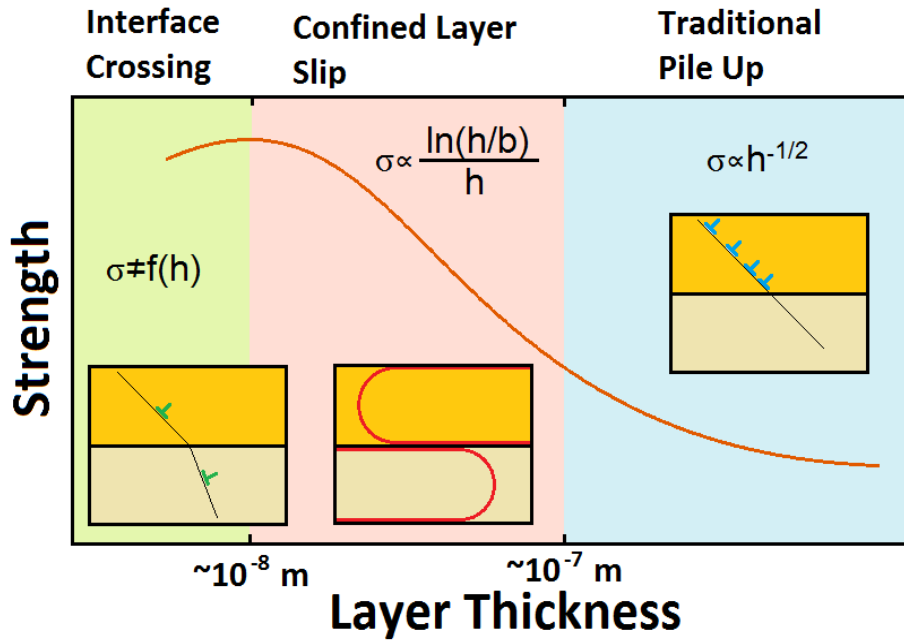
Figure 2. Schematic representation of different deformation mechanisms based on the layer thickness (top) (Wang and Misra, 2011). The bottom graph shows the experimental flow stress (estimated from the hardness divided by 2.7) vs the inverse root of the layer thickness for Cu-Nb multilayers. The Hall-Petch relation is shown to describe the behavior for layers larger than around 50 nm. Reprinted from (Misra et al., 2005).

7

At large layer sizes dislocations are able to pile up as normally expected in bulk materials. Since the layers typically consist of only one grain in the thickness dimension, the strength vs layer thickness in the pile up regime follows the relation (where h is the layer thickness) that would be expected when considering Hall-Petch strengthening. This is also seen in the experimental flow stress data as shown in Figure 2 (Misra et al., 2005). As the layer thickness decreases, there is not enough distance for dislocations to pile up. At intermediate thicknesses ranging from a few nanometers to around 50 nm, deformation is able to occur through confined layer slip. Confined layer slip occurs when force is applied to a threading dislocation (one which is pinned on two adjacent interfaces) which causes the dislocation to bow between the layers. When the resolved shear stress exceeds the energy for increasing the dislocation line length on the interface, the dislocations propagate through the layers leaving dislocation lines along the interface (Misra et al., 2005).

The metal-ceramic interface causes one notable difference between what is outlined in Figure 2 and what would occur in metal ceramic systems. The interface crossing regime, which usually occurs at layer thicknesses below a few nanometers in metal-metal systems, would not be applicable. As dislocation motion in crystalline ceramics is exceptionally unfavorable and impossible in amorphous cases, the metal ceramic interface is effectively impenetrable for dislocations. The only other deformation pathways available for the ceramic layers are brittle fracture and the formation of shear bands. In addition to impeding dislocation motion in the metal layer, the interface acts as a barrier to brittle fracture as well. In metal-ceramic systems this would largely be due to

the crack blunting effect when passing through the ductile metal layers. However, even in ceramic-ceramic systems where there is no plastic blunting effect, the high density of interfaces help to deflect cracks as shown in Figure 3 leading to improved toughness (Wiklund et al., 1997).
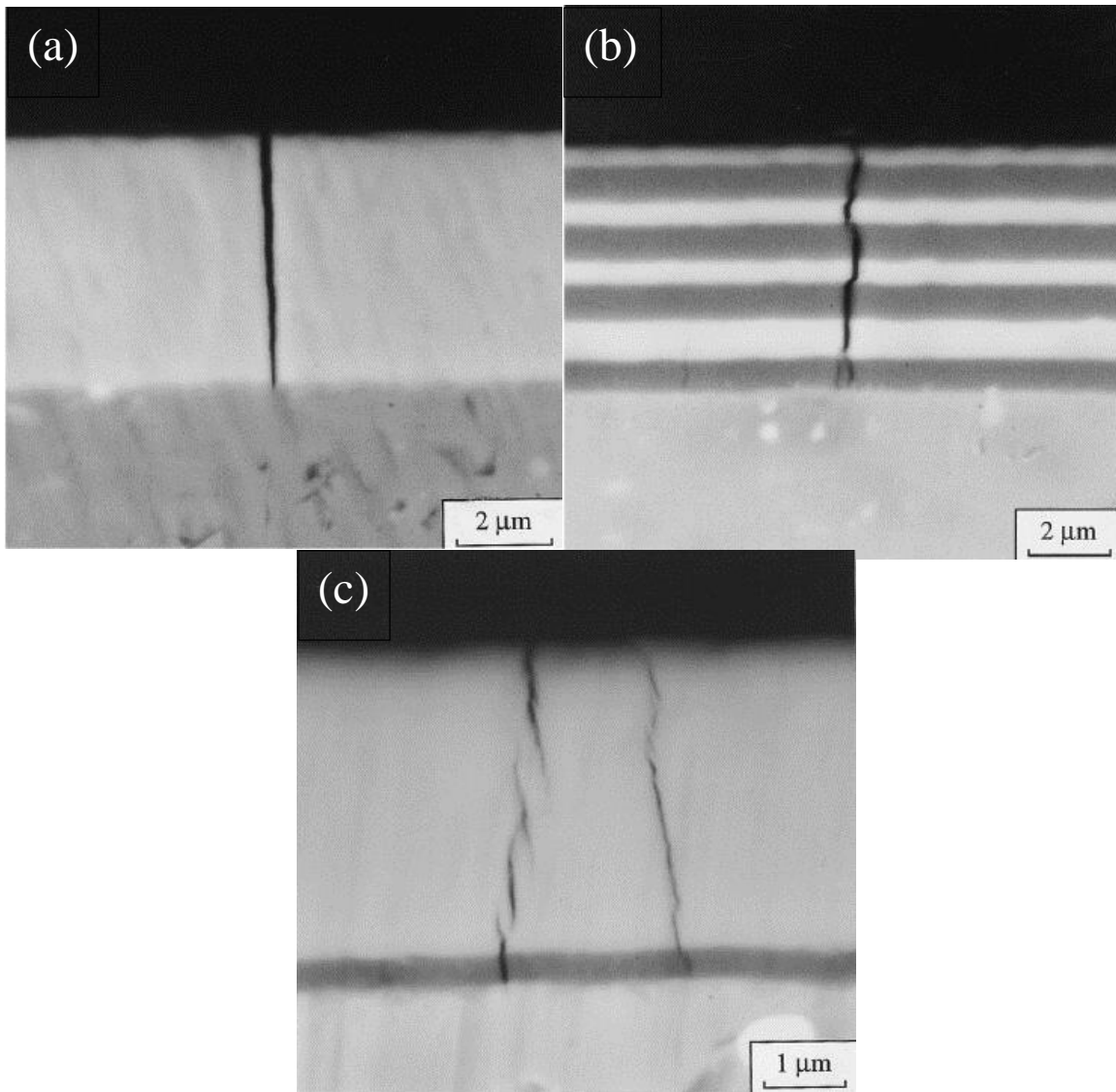
Figure 3. Images showing crack deflection in a single layer NbN film (a), micro scale NbN-TiN layers (b), and nano scale NbN-TiN layers (c). Reprinted from (Wiklund et al., 1997)

The final contribution to the strength of these is from the effect of constraint. Constraint of deformation occurs when stresses are applied to adjacent materials with different stress strain behavior. In order to keep the interface between the two intact, hydrostatic stresses build up (Llorca et al., 1991), which delays the onset of plasticity in the weaker layer. As the metal and ceramic phases generally have very different elastic properties and strong interfaces (Chawla et al., 2008), this constraint helps to increase the apparent strength of the ductile layers. Additionally, once plastic strain does begin to develop, the buildup of hydrostatic stresses greatly increases the strain hardening rate, as shown by studies using FEM simulations of laminate structures (Lotfian et al., 2013, Tang et al., 2010b).

2.2 Micromechanical Testing Methods

Micro-scale testing techniques have become an increasingly popular area of interest, as there are a wide variety of applications which can make use of the information. Firstly, as in the case of nanolaminates, these techniques are required for materials which have limited volumes. Secondly, the ability to obtain site specific properties of individual constituents can be very advantageous to the modelling community. This small scale constituitive behavior is able to be combined with microstructural information to improve the accuracy of simulations and improve the understanding of each constituent's role in the macroscopic deformation behavior (Chawla et al., 2006, Qidwai et al., 2009, Sidhu and Chawla, 2006). Finally, the damage induced by these techniques is small enough that in many cases macroscale components could be returned to service following characterization, allowing for quasi-nondestructive monitoring of components throughout their service life.

Instrumented indentation forms the backbone of nearly all of these techniques, where the load and displacement are able to be measured while forming an impression in the surface. Significant advances in the load and displacement measurement capabilities have allowed smaller and smaller volumes to be tested with the same accuracy. The most straightforward of these techniques, and the first to be developed, is nanoindentation (Oliver and Pharr, 2004). This technique utilizes a sharp indenter, usually having a Berkovich geometry (3 sided pyramid) to make impressions in the sample while measuring the load and displacement. The hardness and effective modulus can be quantified using the unloading slope of the curve, shown schematically in Figure 4, according to the following equations (Oliver and Pharr, 2004):

$$E_{eff} = \frac{S}{2\beta}\sqrt{\frac{\pi}{A}} \quad \text{and} \quad H = \frac{P_{max}}{A}, \tag{1}$$

where β is a dimensionless constant, A is the contact area between the indenter and the material (dependent on the indenter geometry and displacement), and P_{max} is the maximum applied load. More modern techniques utilize a superimposed harmonic load to provide these properties as a function of indentation depth (Chawla et al., 2008, Oliver and Pharr, 2004, Singh et al., 2014, Li and Bhushan, 2002). This technique is advantageous since it requires no sample preparation beyond having a relatively flat and scratch free sample, but unfortunately is unable to provide a uniform and uniaxial stress state (Chawla et al., 2008), making mechanistic interpretations of the results more difficult.

11
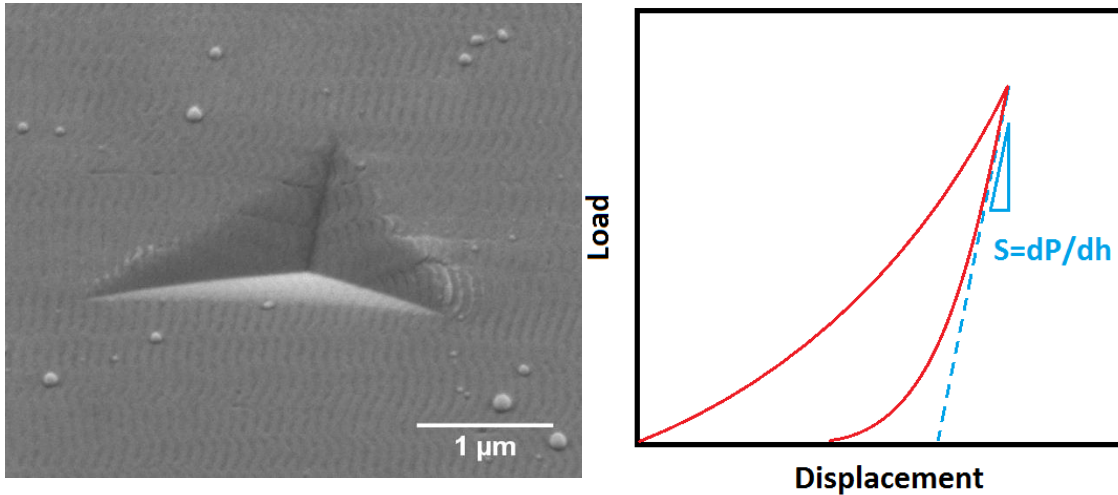
Figure 4. SEM image of an impression made using a berkovich indenter (left) and a schematic of a typical load-displacement curve used to calculate the hardness and modulus (right)

The micropillar compression technique attempts to remove the uncertainty associated with the stress state by creating a micrometer scale cylindrical pillar that is then compressed using a nanoindenter equipped with a flat punch instead of a sharp tip. This allows an actual stress-strain curve to be recorded (in contrast to only a hardness value provided by indentation), providing additional information about the hardening behavior of the material. The most commonly utilized technique for creating these cylindrical pillars, shown in Figure 5 (a), is FIB milling, where an ion beam is used to remove an annular pattern of material, leaving a free standing pillar (Singh et al., 2010b, Lotfian et al., 2013, Greer et al., 2005, Guo et al., 2014, Jiang and Chawla, 2010, Mayer et al., 2015b, Moser et al., 2007, Shim et al., 2009, Soler et al., 2014, Zhang et al., 2013b). Lathe-milling, where the sample is milled at a low incident angle and rotated in small increments, is also commonly used (Uchic et al., 2009, Uchic and Dimiduk, 2005, Singh et al., 2010b) and allows pillars to be made with very little taper as shown in Figure 5 (b).

12

However this approach has the disadvantages of increased FIB damage, redeposition, and fabrication time, which can be more detrimental than the small amount of taper retained using annular milling. Other techniques such as lithography and selective etching have been used to generate these structures as well but the FIB process allows a much wider array of samples to be characterized.
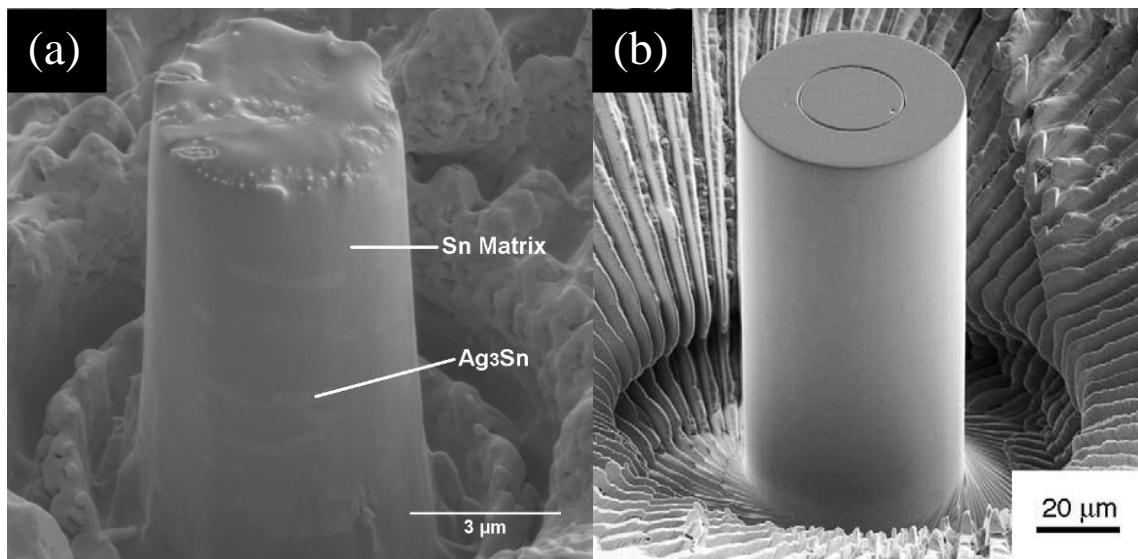
Figure 5. FIB milled micropillars fabricated using annular milling (a) and lathe milling (b). Reprinted from (Mayer et al., 2015b) and (Uchic and Dimiduk, 2005), respectively.

The tensile behavior of materials is also important, as there can be large differences compared to the compressive behavior obtained through pillar compression, especially in brittle materials where compressive stresses help prevent crack propagation. A popular technique for applying tensile stresses on a micro scale is cantilever beam testing (Yang et al., 2014, Kupka and Lilleodden, 2012, Gong and Wilkinson, 2009, Ding et al., 2012, Ding et al., 2014), which uses an indenter to apply a bending moment to a horizontal beam as shown in Figure 6 (a). Although the stress state is not uniform throughout the

sample, this technique provides a relatively simple method for generating a tensile stress in the material, requiring only standard nanoindentation equipment. In addition to cantilever beam testing, advances in SEM in situ indentation capabilities have enabled direct tensile testing of microscale materials (Kim et al., 2009, Kiener et al., 2007). Dogbone shaped samples are cut and allow a C shaped indenter tip to pull the sample in tension as shown in Figure 6 (b).
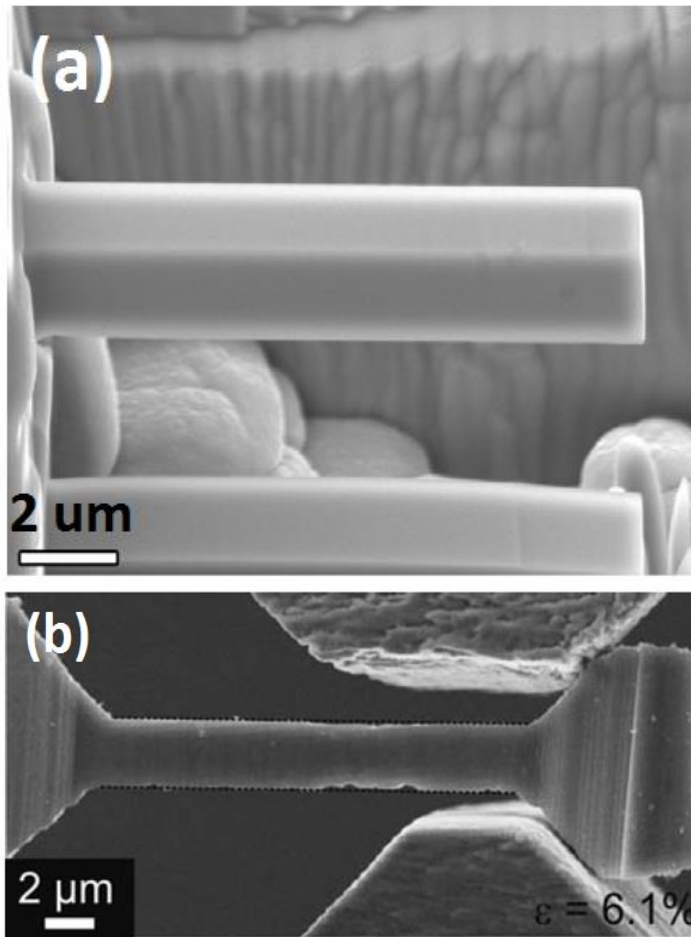
Figure 6. Micro scale testing geometries used to apply tensile stresses. Cantilever beams (a) are put in bending using a sharp tip while dogbone geometries (b) are able to be pulled directly in tension. Reprinted from (Yang et al., 2014) and (Kiener et al., 2007), respectively.

A wide variety of micromechanical testing methods have been employed to determine the fracture toughness of materials as well. The simplest method is based off the size of cracks which form around sharp indents as seen in Figure 7 (a) (Anstis et al., 1981, Casellas et al., 2007), however this technique is limited to extremely brittle materials as most materials require quite large impressions in order to develop cracks. More recent methods have enabled testing of smaller, less brittle materials to be tested. The most common of these techniques are single cantilever bending (Jaya et al., 2015, Matoy et al., 2009, Di Maio and Roberts, 2005, Wurster et al., 2012, Iqbal et al., 2012, Best et al., 2016), clamped beam bending (Jaya et al., 2015, Jaya and Jayaram, 2014, Jaya et al., 2012), double cantilever compression (Jaya et al., 2015, Liu et al., 2013b), and pillar splitting (Jaya et al., 2015, Sebastiani et al., 2015), shown in Figure 7 (b-e), respectively. The most thorough comparison of these techniques was carried out by Jaya et al. (2015), who utilized a range of different methods to characterize the fracture toughness of (100) Si. It was shown that all four geometries mentioned above resulted in fracture toughness values ranging from 0.75 - 0.89 MPa√m depending on the technique, which is commensurate with bulk literature values. Even though every technique can provide similar results, they each have advantages and disadvantages which need to be considered for a given application. Pillar splitting for example, requires the least FIB preparation, but cannot be used to test individual interfaces. The double cantilever compression and clamped beam bending can provide stable crack growth but require in situ capabilities to obtain the precise alignment required for testing. Single edge notch beams, which are the most widely used geometry, are able to be tested ex situ but current analysis methods require samples which display elastic-brittle behavior.

15
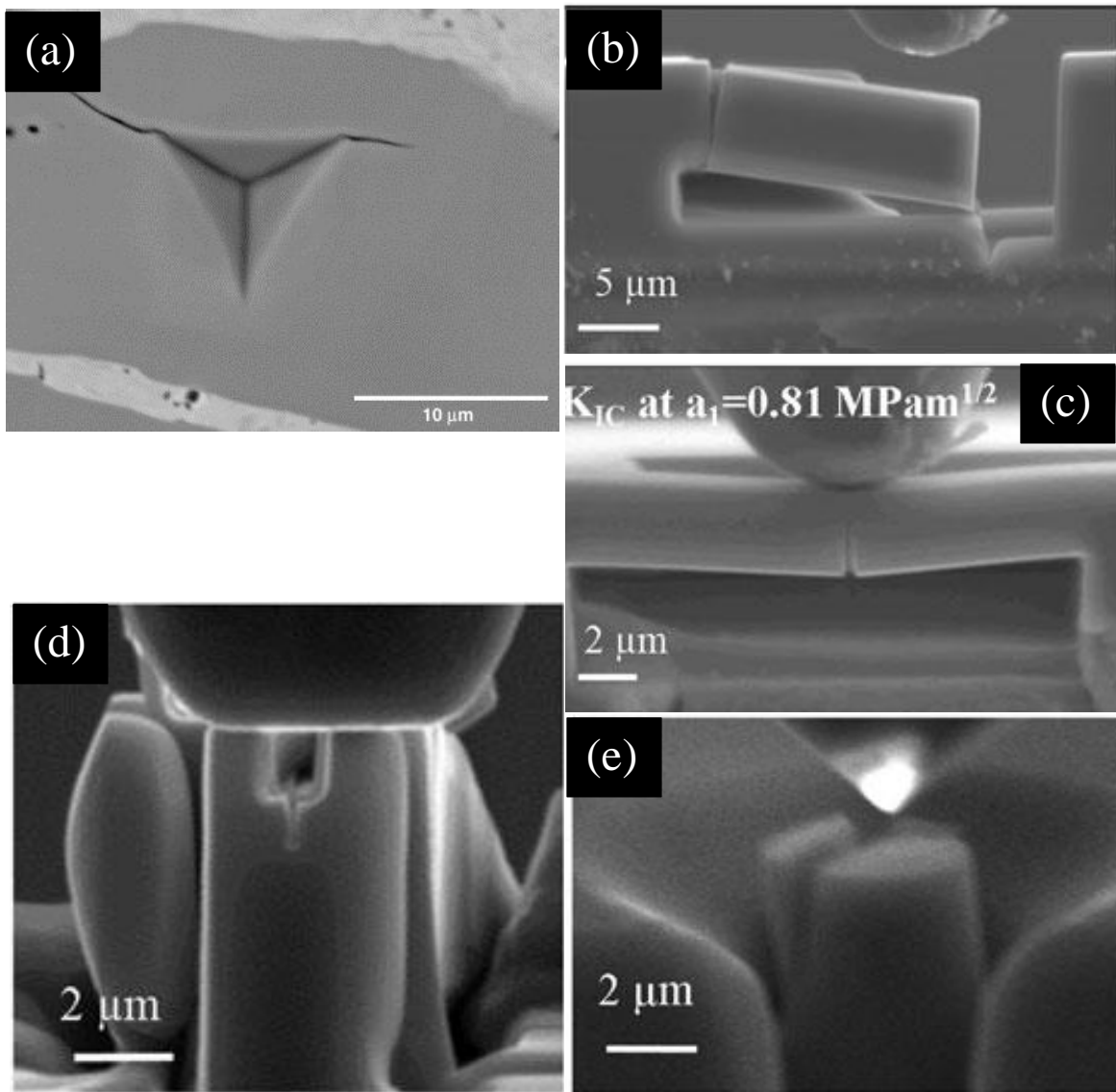
Figure 7. Fracture toughness measurement techniques at the micro scale including indentation crack length (a), single cantilever bending (b), clamped beam bending (c), double cantilever compression (d), and pillar splitting (e). (a) was reprinted from (Casellas et al., 2007), while (b-e) was reprinted from (Jaya et al., 2015).

Due to the experimental difficulties associated with shear testing, only a handful of attempts have been made to characterize this type of loading at the micro scale (Heyer et al., 2014, Li et al., 2012, Pfetzing-Micklich et al., 2011). The method used previously on nanolaminate materials (Li et al., 2012, Liu et al., 2013a) makes use of pillar compression, but with the interface oriented at 45°. The resolved shear stress causes the interface to fail, as shown in Figure 8 (a). The drawback of this approach is that it is only applicable to testing interfaces with very low relative strengths and, as the stress state is not pure shear, there is some question regarding the effect of the compressive stress component on the behavior. Other studies have utilized the geometry shown in Figure 8 (b), which provides a stress state which is nearly pure shear by using a suspended beam attached to the surrounding material by two narrowed regions (Heyer et al., 2014). When an indentation load is applied to the central area, a shear stress develops in the thinner ligaments. However this technique is imperfect as any deviation of the indenter from the exact center of the beam will change the distribution of stress in the two shear sections.
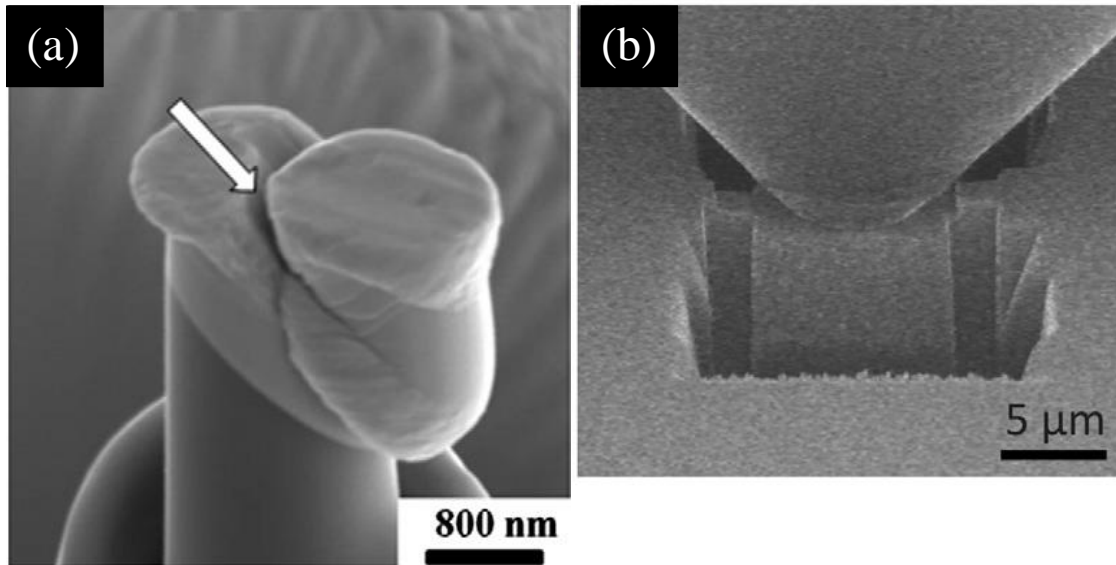
Figure 8. Micro scale testing geometries used for characterizing the shear behavior of a material. Reprinted from (Liu et al., 2013a) and (Heyer et al., 2014), respectively.

One concern regarding the accuracy of these types of tests is the damage induced by the ion beam. Ion beam irradiation has been shown to introduce microstructural changes to the surface that can affect the mechanical behavior of materials (Shim et al., 2009, Bei et al., 2007, El-Awady et al., 2009). This damage can be due to both the high energy bombardment of the ions as well as the specific chemistry of the ions used. Because of their high kinetic energy, the ion beam impacting the sample surface leads to a higher concentration of defects such as dislocation loops, implanted ions, self intersticials, and vacancies (Idrissi et al., 2011), as well as a thin amorphized layer (Kiener et al., 2007). The three most common FIB sources available are Ga, He, and Xe, each have particular considerations that need to be taken into account for milling these miniature testing geometries. Although Ga ions are by far the most widely used, because it is reactive, the implanted ions can locally form an alloy with various samples. This is especially

18

concerning with regard to metals such as Al, which is susceptable to Ga liquid metal embrittlement (Schmidt et al., 2002, Rajagopalan et al., 2014). Due to its relative non-reactive nature, He ions have also been utilized. The lower mass of the ions leads to much less damage to the surface but also result in a much lower milling rate. Another drawback to the He ion source is that at high doses, swelling of the sample surface can occur because He ions are implanted faster than they can leave the surface, leading to a buildup of pressure in the material (Best et al., 2016). Xe ions are also fairly non-reactive compared to Ga and the larger ion size makes the milling rate much higher, but the spot size is greater leading to less precise cuts (Best et al., 2016, Delobbe et al., 2014).

Although further work is needed to accurately quantify the effect of the ion beam damage in the Al-SiC nanolaminate system, qualitative observations have indicated that the effect is minimal. First, TEM observations from Lotfian et al. (2013) do not show any irradiation induced dislocation loops after milling, as shown in Figure 9. Second, the same image shows that there is a thin surface film on FIB milled micropillars, presumably from ion beam redeposition, amorphization, or oxidation, with thicknesses of approximately 5 nm on the aluminum and 3 nm on the SiC. Considering the size of the testing geometries used in these studies, this thickness of surface film would have a negligible effect on the measured mechanical response. Finally, the embrittlement of the Al phase due to diffusion of Ga to the interfaces is also a concern. This segregation significantly weakens the interface, leading to brittle interfacial fracture behavior. In an unpublished study by Yang and Molina (Yang and Molina-Aldaregua, 2016), TEM based EDS line scans showed a maximum of 2 at% increase in concentration across the Al-SiC

boundary (Figure 10). It should be noted that this represents an extreme upper bound

estimate for the Ga concentrations because, as the TEM foils are only ~100 nm in

thickness, even a small penetration depth would correspond to large proportion of the

sample volume. In terms of mechanical response, even this concentration is expected to

have a minimal effect on the behavior. Studies characterizing the Ga concentration at

embrittled boundaries show concentrations of approximately 10-25 at% Ga depending

on the orientation (Kobayashi et al., 2006). Finally the deformation behavior of these

nanolaminates observed using FIB milled geometries shows very little evidence of the

brittle intergranular fracture characteristic of Ga embrittlement even in small diameter

micorpillars (see Chapter 4).
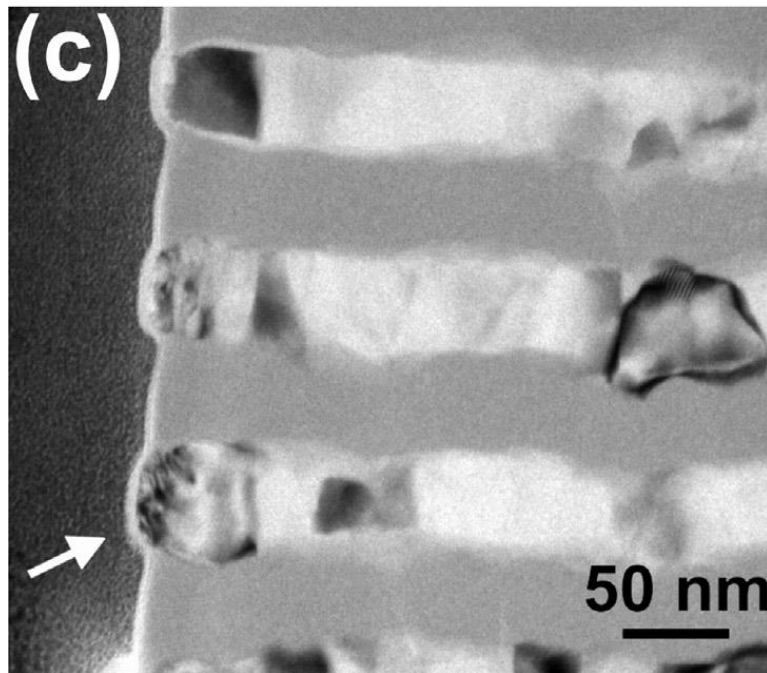
Figure 9: TEM cross section of the edge of an Al-SiC pillar showing a

few nm thick amorphized surface layer and little other damage.

Reprinted from (Lotfian et al., 2013).
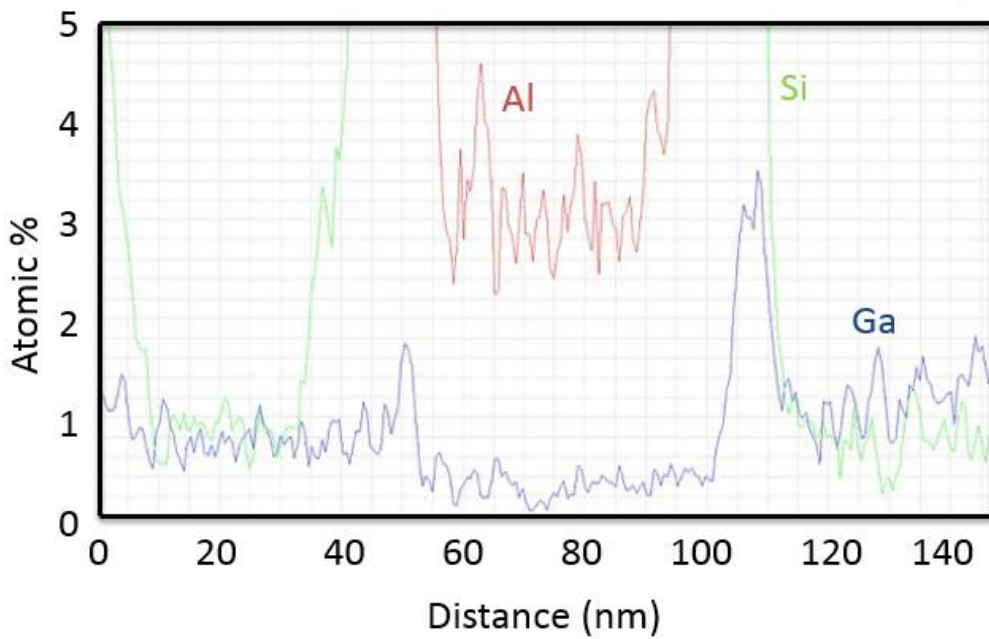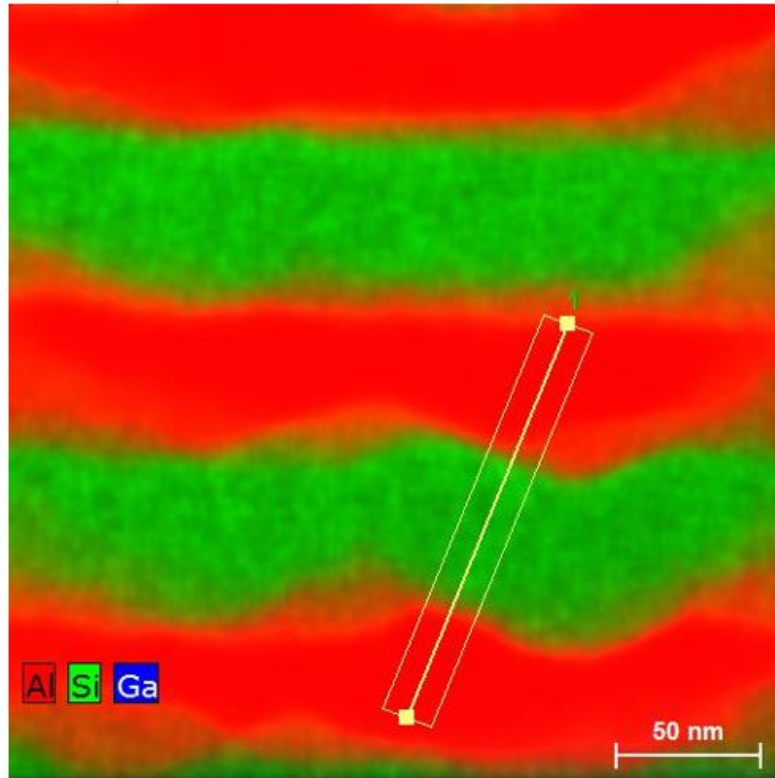
Figure 10: TEM EDS compositional map, line profile, and high angle annular dark field image showing a small amount of Ga segregation at the interface between Al and SiC. From (Yang and Molina-Aldareguia, unpublished work)

2.3 Sample Fabrication

The fabrication of the particular Al-SiC nanolaminates used in the following chapters has been thoroughly documented in the literature previously (Yang et al., 2015). Magnetron sputtering was used to fabricate nanolaminate materials consisting of Al and SiC layers with individual layer thicknesses ranging from 2 to 100 nm. The base pressure of the sputtering unit was 10^{-7} Torr. Argon (Ar) was used as the sputter gas and all depositions were carried out at an Ar working pressure of 3.0 mTorr (0.4 Pa). The pure aluminum target (>99.99% purity, Kurt J. Lesker, Clairton, PA) was sputtered at a DC power of 95 W. SiC layers were deposited from a SiC target made by hot isostatic pressing (>99.5% purity, Kurt J. Lesker, Clairton, PA) using identical argon pressure and a RF sputter power of 215 W. The targets were pre-sputtered for about 10 min at 40 W for Al and 95 W for SiC to remove any oxides and contamination prior to nanolaminate deposition. The sample holder was continuously rotated during sputtering to obtain a uniform layer thickness. The deposition rates were approximately 7.5 nm/min for Al and 3.9 nm/min for SiC. Alternating Al and SiC layers were deposited by means of a computer controlled shutter system to build up the multilayer structure.

The multilayer thickness and the individual layer thicknesses were characterized using TEM cross sectional images, as shown in Figure 11 (Yang et al., 2015). Three separate sample series, outlined in Table 1, were fabricated in order to separate the effects of volume fraction from increased constraint on the mechanical behavior. In series 1, the SiC layer thickness was kept constant at 50 nm and the Al layer thickness was varied between 10 and 100 nm. In series 2, the Al layer thickness was kept constant at 50 nm

22

and the SiC layer thickness was ranged between 2 and 100 nm. Finally the volume

fraction of both Al and SiC was fixed at 50% in series 3 and the layer thicknesses were

varied between 10 and 100 nm. The last column in Table 1 indicates the volume fraction

of Al in each nanolaminate, according to the nominal layer thicknesses.
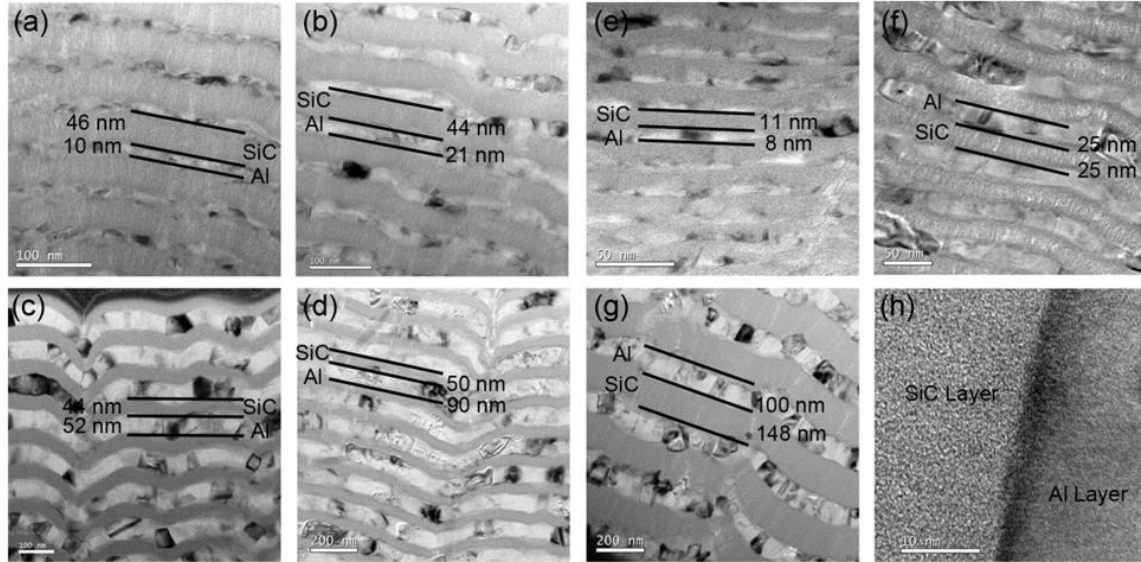
Figure 11. Bright Field TEM images of Series I samples: (a) Al10SiC50, (b) Al25SiC50, (c) Al50SiC50, (d) Al100SiC50. BF-TEM of Series II samples: (e) Al10SiC10, (f) Al25SiC25, (g) Al100SiC100; (h) HR-TEM of Al100SiC100. Reprinted from (Yang et al., 20152016)

Table 1. Number of layers and layer thicknesses in the three series of nanolaminates under study. Samples from series S2 were not measured using TEM so the nominal values for the thickness are given.

Series	Sample	Thickness (µm)	Number of bilayers	t_{Al} (nm)	t_{SiC} (nm)	VAl
S1	Al10SiC50	~15	250	10±1	46±3	0.17
	Al25SiC50	~13.3	175	21±1	44±2	0.33
	Al50SiC50	~15	150	52±2	44±2	0.50
	Al100SiC50	~15	100	90±8	48±3	0.67
S2	Al50SiC2	~13.5	260	50	2	0.96
	Al50SiC10	~15	250	50	10	0.83
	Al50SiC25	~13	175	50	25	0.67
	Al50SiC100	~15	100	50	100	0.33
S3	Al100SiC100	~17	85	100±6	148±5	0.50
	Al25SiC25	~14	280	25±4	25±7	0.50
	Al10SiC10	~12	600	8±1	11±2	0.50

24

CHAPTER 3

MICROMECHANICAL AND *IN SITU* SHEAR TESTING OF AL-SIC NANOLAMINATE COMPOSITES IN A TRANSMISSION ELECTRON MICROSCOPE

3.1 Introduction

Quantifying shear properties of the interfaces in nanolaminates is a challenge. A few methods have been utilized previously to quantify the shear properties on the microscale, although there are inherent experimental issues associated with these techniques.

Previous work by Li et al.(Li et al., 2012) on metal-metal nanolaminate composites utilized pillars milled with interfaces inclined 45º to resolve the maximum amount of shear stress on the interface. The drawback of this geometry is that in addition to the shear stress resolved on the interface, there is also a large normal stress component superimposed on the shear stress. The *in situ* characterization in that work utilized pillars which were inclined relative to the flat punch. While this does generate a shear stress, there is also a large bending moment on the pillars. The use of these methods is limited to interfaces with very low shear strengths relative to the normal strength so that the normal and bending stresses have a minimal effect.

Other studies by Pfetzing-Micklich et al.(Pfetzing-Micklich et al., 2011) and Heyer et al. (Heyer et al., 2014) also made shear strength measurements using a FIB milled geometry having a large beam supported on either side by a thinned region that will shear when a load is applied to the center of the beam. Although this geometry allows for a fairly

homogeneous shear stress state, alignment of the indenter is critical. Any deviation of the indenter from the center of the beam would induce a bending stress and/or an unequal load distribution between the two gauge sections. Additionally, this type of geometry is not ideal for *in situ* TEM studies because both gauge sections cannot be easily viewed simultaneously.

The double notched interlaminar shear test involves a specimen notched on opposite sides, and loaded in compression, such that the longitudinal plane between the notches is subjected to pure shear (Zweben et al., 1979, Chawla et al., 2012, Kedward, 1972). This test has been used extensively in bulk fiber reinforced composites, where shear failure between plies occurred consistently (Zweben et al., 1979, Chawla et al., 2012). The microscale equivalent of this geometry is very attractive as it would have a few advantages over the alternative approaches listed above. These include a nearly pure shear stress state, a single gauge section, tolerance to imperfect alignment, and the ability to easily view the fracture surface post mortem.

This testing method was performed on samples with 100 nm and 50 nm Al layer thicknesses in order to determine how the shear behavior changes at different layer thicknesses and therefore different levels of constraint. In addition, double notch samples were also made on TEM foils and fractured *in situ,* in order to to elucidate the failure mechanisms. The *in situ* characterization technique allowed for the crack path to be observed in relation to the layers and individual grains.

3.2 Materials and Experimental Procedure

Two types of samples with different individual layer thicknesses were used in this study. The first sample consisted of 50 nm Al layers and 50 nm SiC layers, whereas the second consisted of 100 nm Al layers and 50 nm SiC layers.

Shear testing of the interface required that the films be oriented parallel to the loading axis. Therefore, the samples were mounted in epoxy edge on. Mechanical polishing to a final polish of 0.05 µm colloidal silica was then carried out on 2 faces to expose a 90° corner. The amount of material that needs to be removed using the FIB is dependent on the rounding at the edge. This rounding was kept to a manageable level by carefully hand polishing using SiC abrasive paper and only using the colloidal silica slurry the minimum amount of time to obtain a smooth surface finish.

Fabrication of the double notch shear pillars (Figure 12) was performed using a dual beam SEM-FIB (FEI Nova 200). Milling from two orthogonal directions was required to fabricate double notch pillars, necessitating the polished and square corner mentioned above. An ion beam current of 20 nA was used to quickly remove material to provide sufficient clearance for the indenter tip (an approximately 25 µm diameter trench) and to form a rough square pillar. To cut the notches, reduce the taper of the pillars and clean the pillar faces, decreasing ion beam currents ranging from 3 nA to 50 pA were used to provide increasing milling accuracy and surface quality. The notches were cut and the top was flattened by milling perpendicular to the original direction. The dimensions of the samples were 3-5 µm square cross sections with a notch separation of approximately 2

28

μm (gauge section). The distance between the top of the pillar and the first notch was made to be larger than the gauge section to ensure that failure would occur in the gauge section. For each of the two different layer thicknesses combinations, two double notch pillars were fabricated and tested to failure.
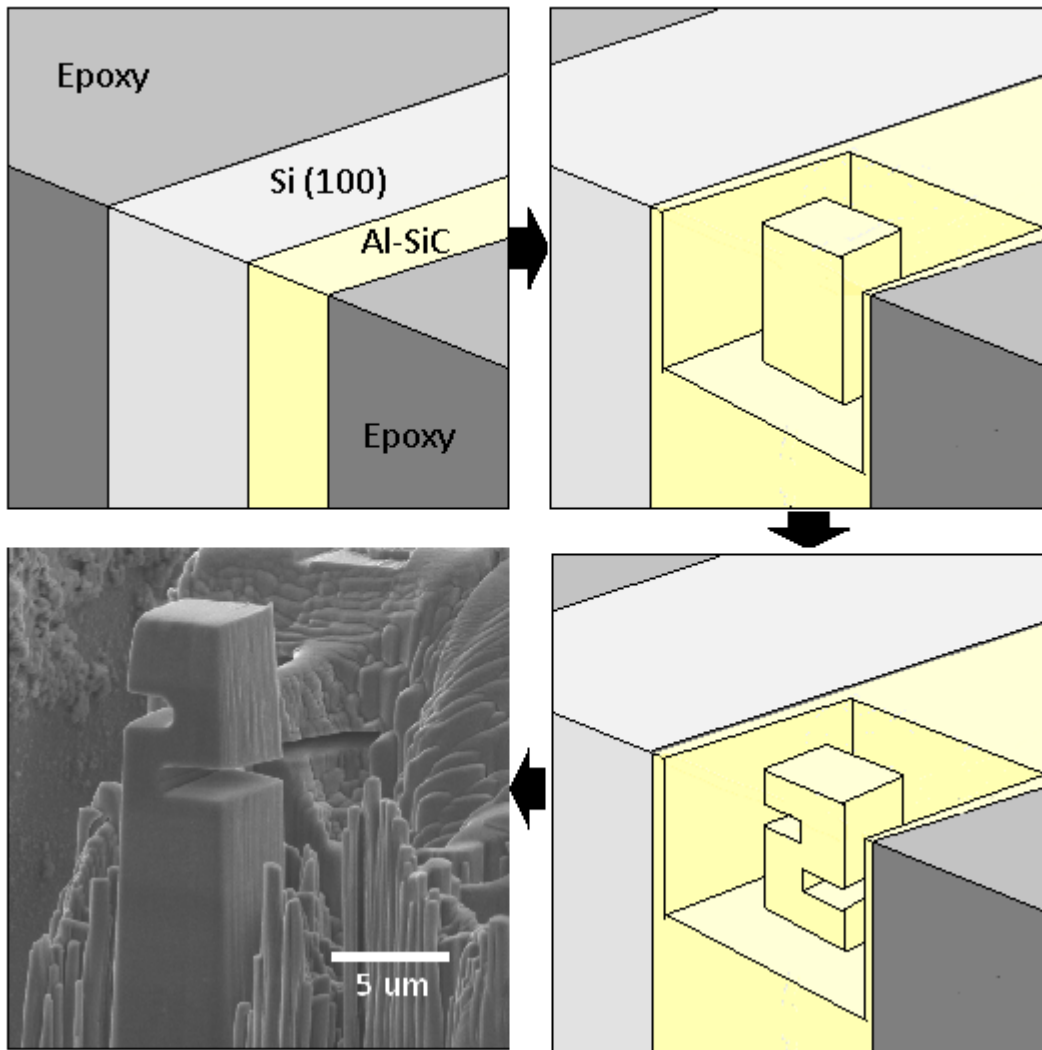
Figure 12. An outline of the milling procedure for double notch pillars. A corner is milled from the top to create a square pillar with access to the side. The notches and top are then milled from the front.

The compression of the double notch shear pillars was carried out using a commercial nanoindenter equipped with a flat punch indenter (Nanoindenter XP, Agilent). The flat punch used was diamond with a square section having side lengths of 10 µm. In order to preserve the fracture surface after testing, the displacement of the pillar should not exceed the size of the notches. Therefore, displacement control was used in all tests to prevent continued compression of the pillar following failure of the gauge section. All tests were carried out using a displacement rate of 10 nm/s to a total depth of 1000 nm. Following compression, the fracture surfaces of the double notch pillars were observed by scanning electron microscopy (SEM).

TEM sample preparation was carried out using a FIB lift-out procedure. The initial steps of the TEM sample preparation procedure is identical to traditional lift out method, as explained elsewhere (Lekstrom et al., 2008, Tomus and Ng, 2013). The only deviation from traditional liftout required for this particular application was the "welding" of the foil, using platinum, to the end of the TEM grid post along the entire length of the sample as shown in Figure 13 (a) and (b). This provides greater mechanical support during straining than the traditional method of welding to the side of the grid post. After the sample was attached to the grid, the sample was thinned to approximately 200 nm for electron transparency. To make the faces of the foil more parallel, small tilting angles and ion beam currents as low as 10 pA at 30 keV were used at the final stages to reduce the taper. The TEM grids were then held perpendicular to the ion beam and the majority of the foil was removed, leaving the double notch shape (Figure 13(c)).
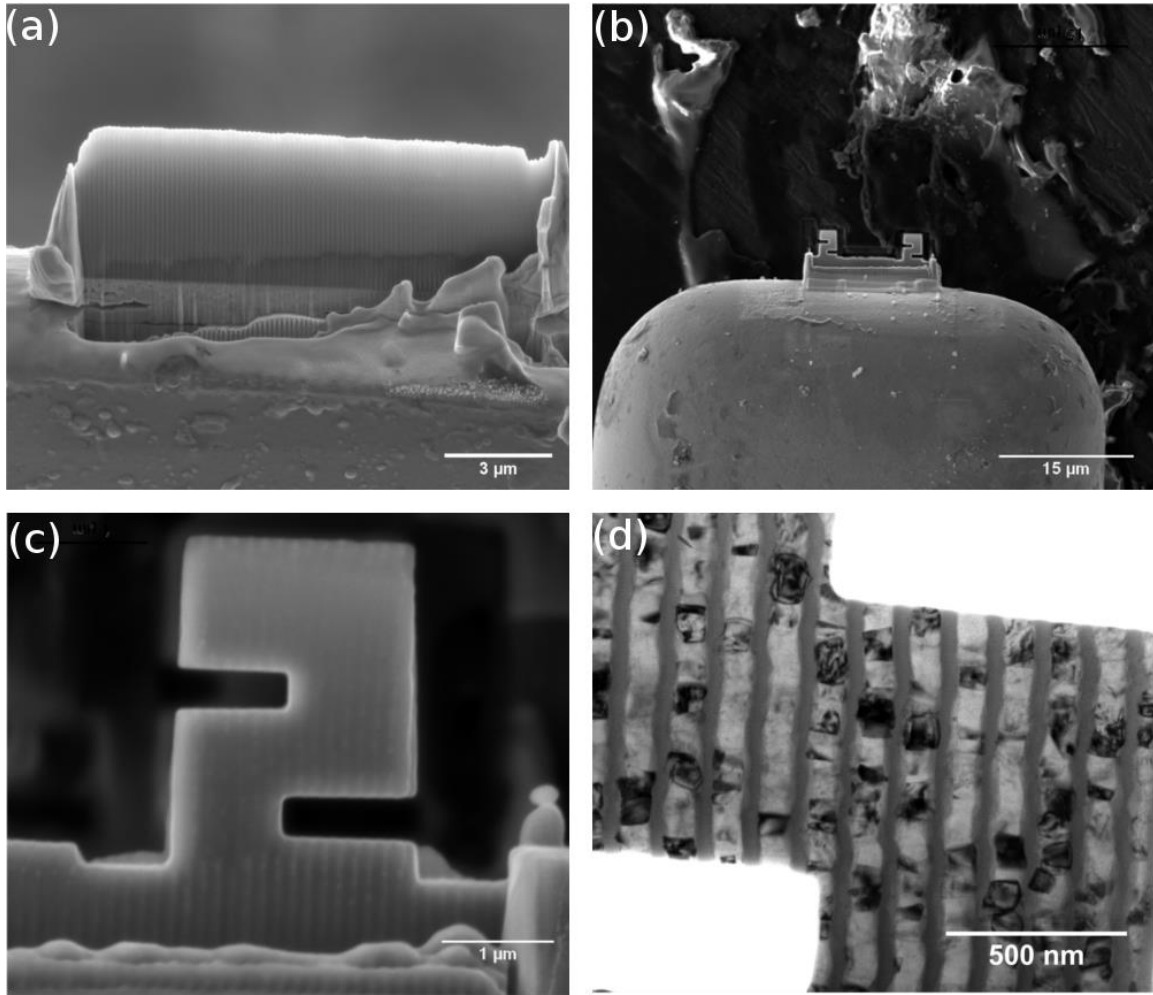
Figure 13. Details of TEM double notch specimens. A) TEM foil after being attached and thinned. B) Low magnification image showing the position of samples on TEM grid post C) Detailed view of double notch geometry. D) TEM image of gauge section before deformation.

Deformation was carried out in a FEI Tecnai F300 TEM using an in situ indentation sample holder (NanoFactory Instruments, Goteborg, Sweden). The basic components of the holder are illustrated in Figure 14. The indenter is held by spring clips to the end of a piezoelectric tube used for positioning of the indenter. The TEM grid is glued to a wire which is held in a sample holding fixture by a set screw. The microscope was operated at 300 keV accelerating voltage in bright field TEM mode (Figure 13 (d)). Tungsten wire sharpened using an electropolishing bath of NaOH in NaNH3 operated at 10-20 VAC was used as an indenter for applying the load to the top of the sample. Images and video were recorded using Digital Micrograph (Gatan Inc.) during straining and after fracture.
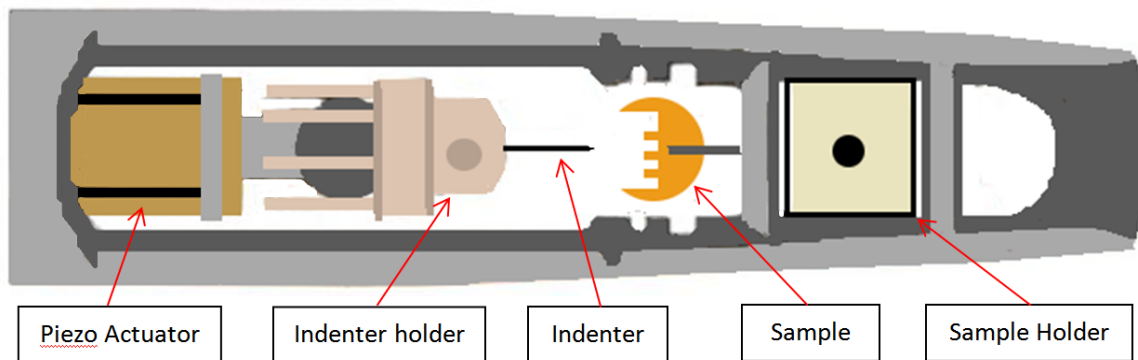
Figure 14. Schematic of in situ TEM holder showing the basic components of the system.

3.3 Results and Discussion

The shear stress vs. shear strain curves, obtained from the load displacement data for the notched pillars, is shown in Figure 15. The shear stress was calculated based on the fracture area measured after failure and the load at fracture. In order to calculate the shear strain, the displacement of only the shear section was isolated from the rest of the components of the sample. The displacements taken into consideration are shown in Figure 16. These displacements are additive, therefore, the displacement of the gauge can be written as

$$d_{gauge} = d_{total} - d_{top} - d_{bottom} - 2d_{notch} - d_{base} - d_{indenter}. \tag{2}$$

Assuming all of the components remain elastic except the gauge section, the displacements of the various components can be calculated using Hooke's Law for the top bottom and notch displacements and the Sneddon correction for the indenter and base displacements. Using Hooke's law the displacements are given by

$$d = \frac{Ph}{AE}, \tag{3}$$

where P is the applied load, E is the modulus and h and A are the height and cross sectional area of each section respectively. The Sneddon correction accounts for the displacement of a flat punch into an elastic halfspace which is given by

$$d = \frac{P\sqrt{\pi}(1 - v^2)}{2E\sqrt{A}}, \tag{4}$$

where v and E are the Poisson's ratio and Young's modulus of the halfspace (Singh et al., 2010b). This correction may slightly underestimate the displacement due to the proximity of the pillars to the edge of the sample.
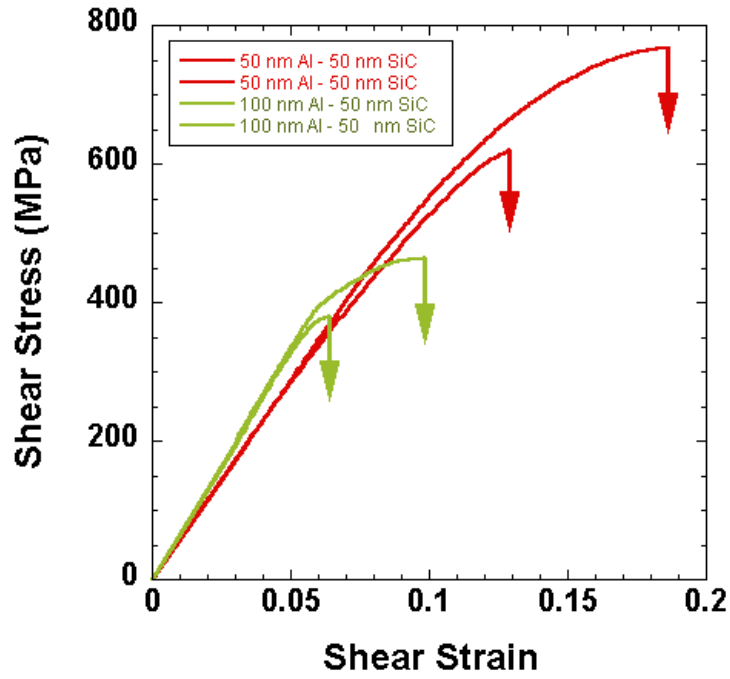
Figure 15. Shear stress vs. shear strain response of double notch geometry showing higher fracture stress in 50 nm Al – 50 nm SiC samples compared to the 100 nm Al – 50 nm SiC samples.
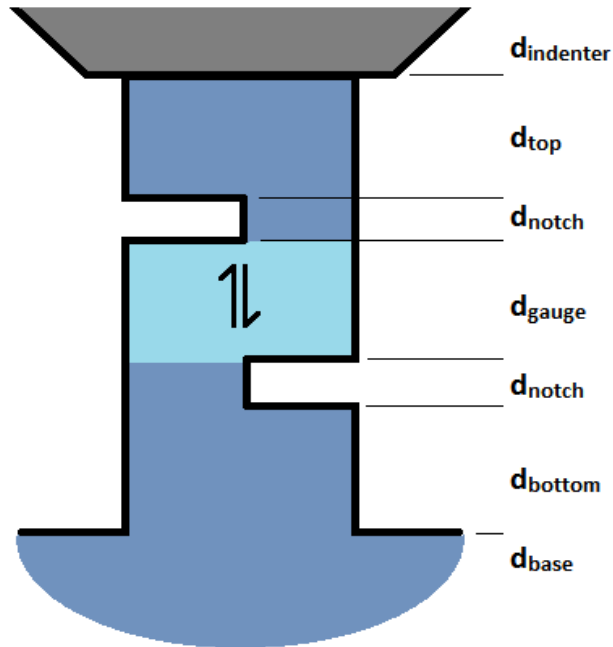
Figure 16. Schematic of the components of the double notch geometry which contribute to the measured displacement

The 50nm Al – 50 nm SiC and 100 nm Al – 50 nm SiC samples exhibited average shear strengths of 690±54 and 423±29 MPa, respectively. Although only two samples of each type were tested, the limited data still shows statistical significance. Assuming both samples exhibit the same variance from experimental variables and the distribution of shear strengths of these materials are normal, a Student's T test shows greater than 95% confidence that the 50 nm Al – 50 nm SiC samples have a higher shear strength than the 100 nm Al – 50 nm SiC.

Geometric effects can also play a role in the material response. Due to the waviness of the layers, a straight notch cut through the nanolaminate sample will not fall on a single layer or interface, making the applied shear stress not on a single continuous layer or interface. Additionally, the radius of the notch corners can affect the amount of stress concentration at the top and bottom of the shear area. These effects were kept to a minimum by using the same fabrication steps for all samples, however small variations may contribute to the differences in strength between tests on the same laminate type.

It is expected that the thinner Al layer should exhibit greater strengths due to the increase in constraint and decrease in grain size. Constraint increases the strength of the aluminum layer because it creates a triaxial tensile stress state which decreases the Von Mises effective stress in the lower stiffness aluminum layer. Hardness measurements of nanocrystaline Al made by RF sputtering show an increase in strength with decreasing grain size commensurate with the Hall-Petch relation over the grain sizes investigated

35

here (Farhat et al., 1996). Since the grain size is approximately proportional to the layer thickness, the predicted increase in strength when comparing the 100 nm Al layer to the 50 nm Al layer is a factor of 1.41 according to the Hall-Petch relation. This is less than the factor of 1.6 increase seen experimentally, indicating that there is some contribution from the increased constraint of the Al layers.

Determining whether the failure occurred within the Al layer, within the SiC layer, or at the interface was not possible using traditional SEM/FIB techniques. Compositional analysis using energy dispersive spectroscopy (EDS) could not be performed because the interaction depth of the electron beam is larger than the layer thickness, causing characteristic x-rays to be emitted from both the Al and SiC layers. Additionally, since the top portion of the pillar is not attached following fracture, only the fracture surface on the base side of the pillar was available for analysis.

Uncertainty in fracture path necessitated the use of the *in situ* TEM techniques. Video frames showing the progression of deformation and fracture through the 50 nm Al – 50 nm SiC sample are shown in Figure 17 (a-d). Images of the fractured TEM samples are shown in Figure 18. In the 50 nm Al – 50 nm SiC sample, the fracture path followed the Al-SiC interface for the majority of the sample but occasionally fractured through the Al layer, and then continued on the adjacent interface. In the 100 nm Al – 50 nm SiC sample, on the other hand, the fracture path was within the Al layer across the whole sample, leaving the interface intact.
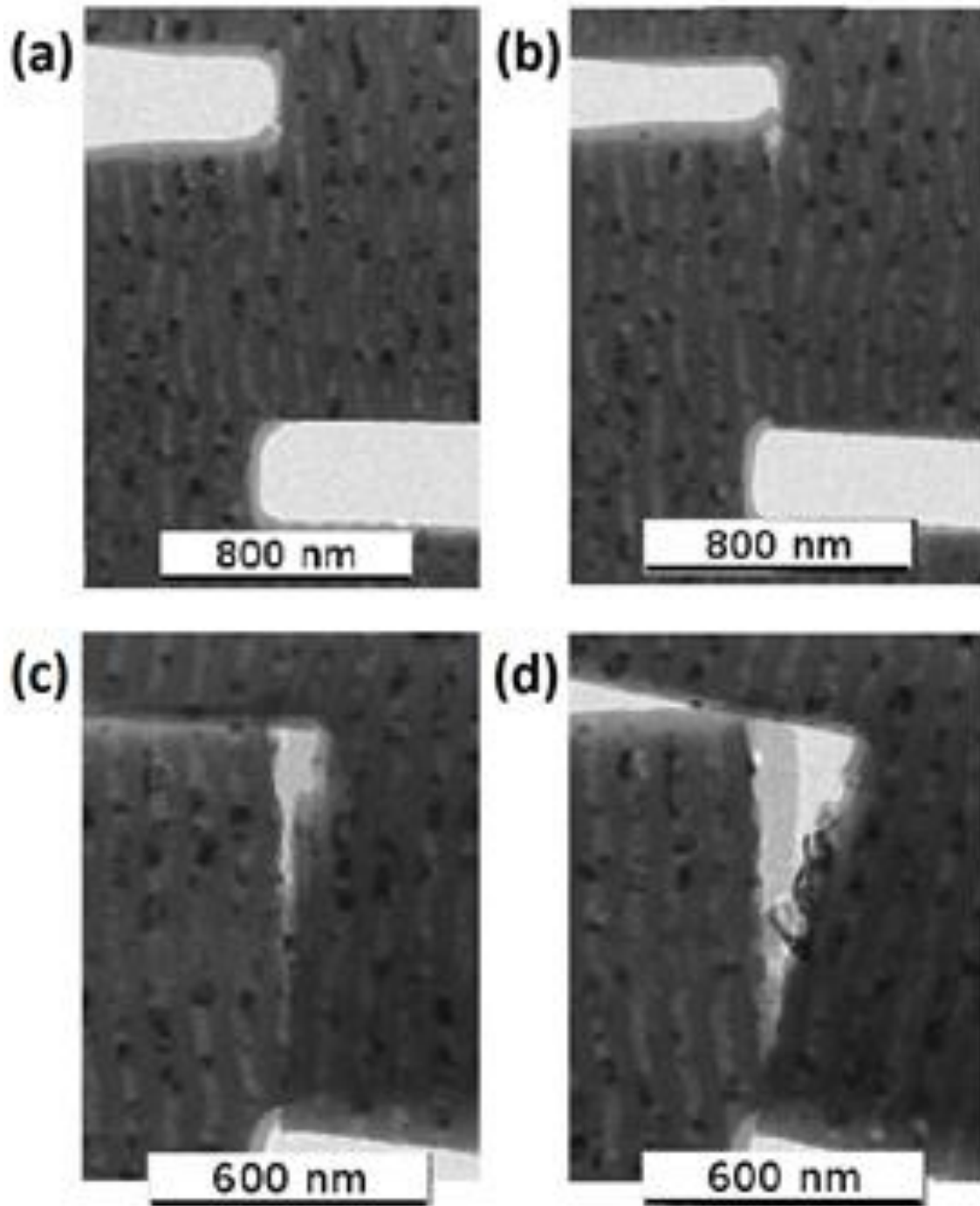
Figure 17. Video frames showing the progression of deformation of the 50nm Al – 50 nm SiC sample.
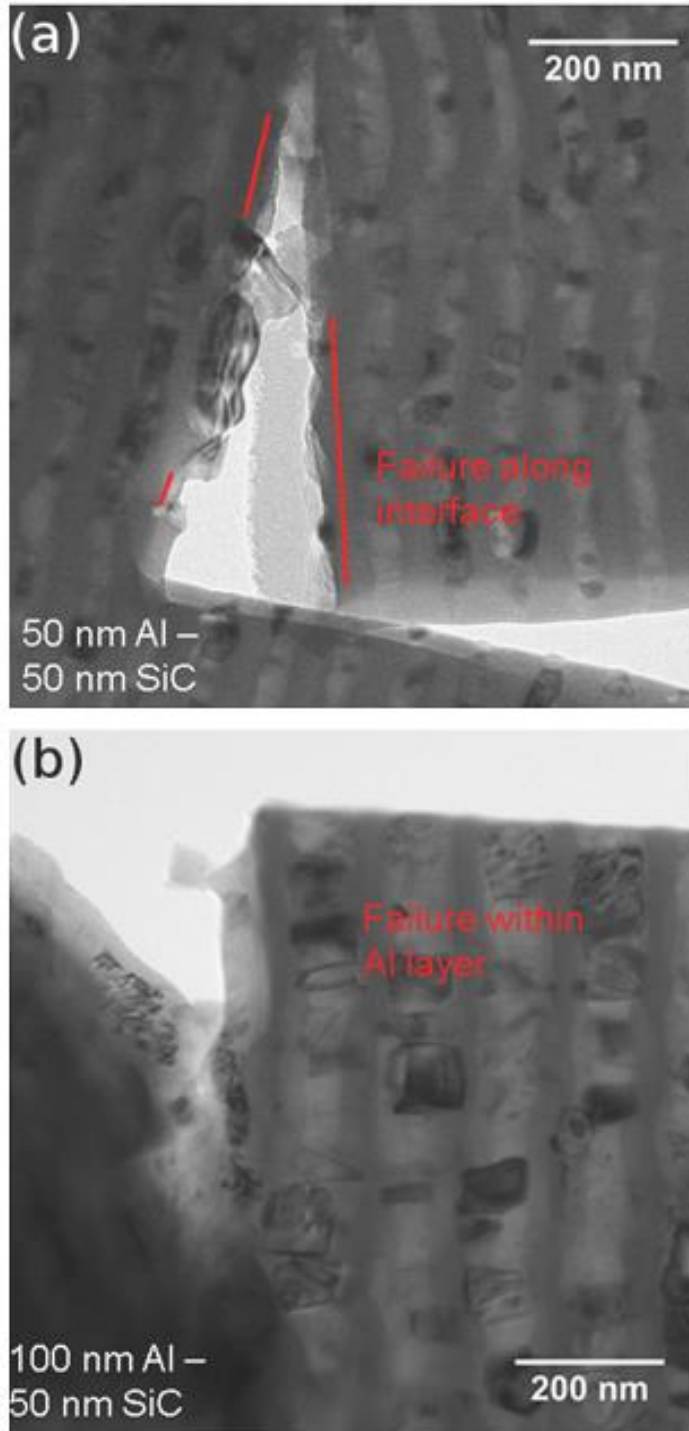
Figure 18. TEM micrographs showing fractured in situ samples. In the 50 nm Al – 50 nm SiC (a) sample the crack path follows the interface the majority of the distance while in the 100 nm Al – 50 nm SiC sample (b) the crack is within the Al layer the entire length.

The fracture surfaces of the *ex situ* tests, as seen in Figure 19, show characteristically different fracture surfaces. The ductile failure surface seen in the 100 nm Al – 50 nm SiC sample would be expected for failure within the aluminum layer, while a more brittle failure as seen in the 50 nm Al – 50 nm SiC sample would be expected for failure at the interface. The 50 nm Al – 50 nm SiC sample surfaces show fine surface roughness and occasional cracking, presumably in the adjacent SiC layer. The fine surface roughness is likely due to the extremely high constraint in these samples. Similar features are seen in tearing topography fracture surfaces, where the constraint in the material creates a highly triaxial state of stress, thereby limiting the size of voids that are formed and generating a surface with very fine roughness (Thompson and Chesnutt, 1979, Williams et al., 2002). The surface of the 100 nm Al – 50 nm SiC shows a fracture surface with larger elongated dimples which is characteristic of greater plasticity in the aluminum layer.

This gives us insight into the interface strength of these materials and the effect of constraint on the deformation behavior. Since the layers are oriented such that the shear stress is in plane with the lamina, the fracture strength is dictated by the strength of the weakest layer.
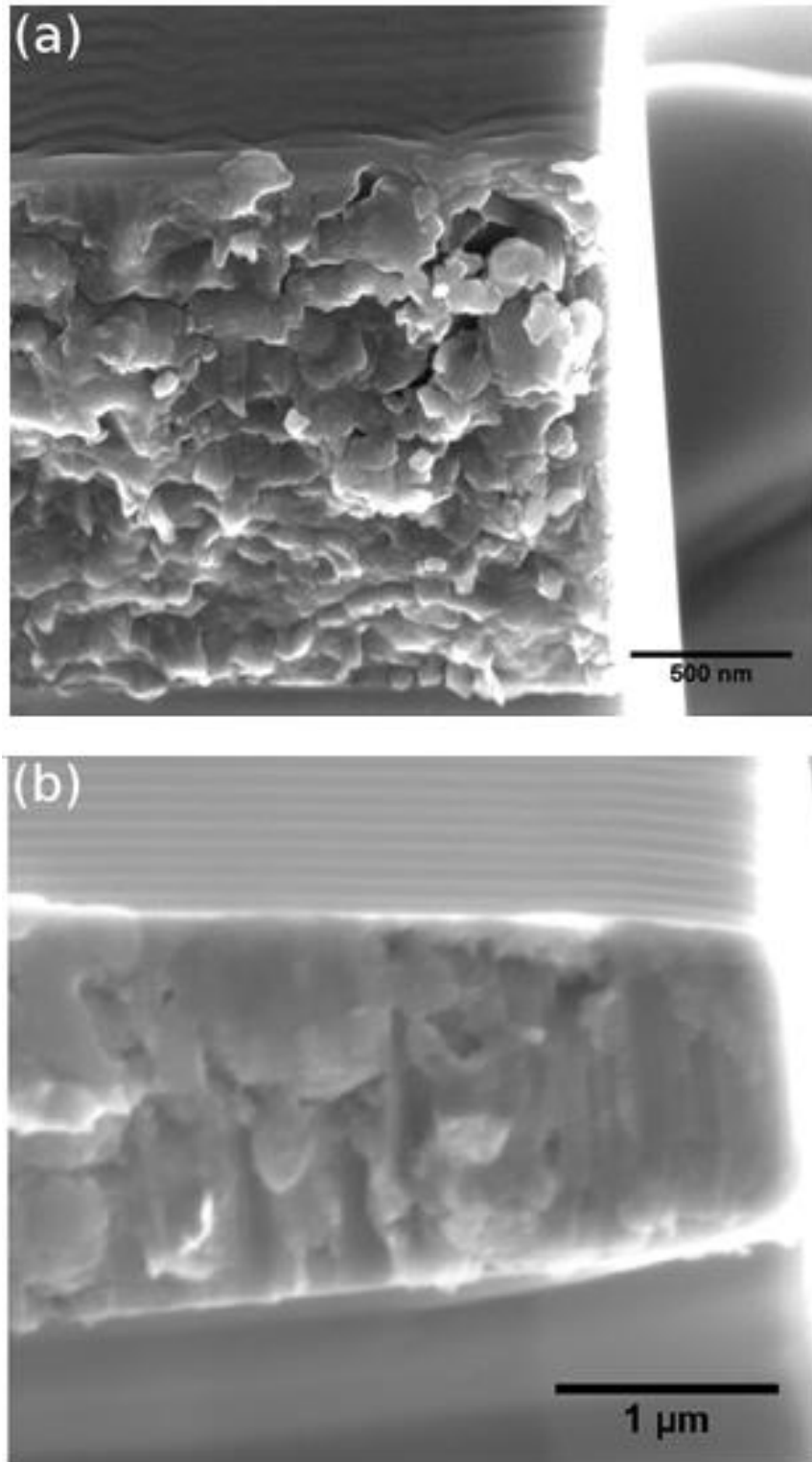
Figure 19. Fracture surfaces of double notch pillar showing fine roughness due to interface failure in the Al – 50 nm SiC sample (a), and ductile shearing in the 100 nm Al – 50 nm SiC sample (b).

The failure of the 50 nm Al – 50 nm SiC TEM samples along the interface shows that the shear strength of the constrained aluminum layer is greater than that of the interface, because failure takes place at the interface. The shear strength of these materials may increase with decreasing Al layer thickness due to strengthening from constraint and decreasing grain size until it reaches a critical value where the interface is the strength limiting factor.

3.4 Summary

In this work, *ex situ* and *in situ* characterization of the shear deformation behavior of Al - SiC nanolaminate composites was carried out. A novel *ex situ* micromechanical testing method quantified the shear strength of two layer thickness combinations which show characteristically different fracture behavior. *In situ* TEM shear testing was used to determine the fracture path through the composite, showing the fracture strength of the 50 nm Al – 50 nm SiC samples is limited by the interfacial shear strength while the fracture strength of the 100 nm Al – 50 nm SiC samples is limited by the strength of the Al layer.

CHAPTER 4

ORIENTATION DEPENDENCE OF AL-SIC NANOLAMINATES UNDER INDENTATION LOADING

4.1 Introduction

Although there is a growing body of research investigating the mechanical properties of these materials in the direction normal to the layers, there is very little work examining the effect of layer orientation relative to the loading axis.

Isostress and isostrain loading are the most classical conditions to understand the mechanical properties of composite materials because they provide bounds for the elastic behavior. For a given composite volume fraction, as a first approximation, the isostress condition is expected to have the lowest stiffness while the isostrain condition leads to the highest stiffness (Agarwal and Broutman, 1990). While the previous work on nanolaminates focuses on loading in the perpendicular orientation (Chawla et al., 2008, Mara et al., 2008, Tang et al., 2010b, Bhattacharyya et al., 2011, Chen et al., 2012), which approximates isostress deformation, no studies have compared this to the deformation in other orientations.

Recent modeling studies by Jamison and Shen (Jamison and Shen, 2015) have shown the effect of initial layer waviness on the plane strain deformation of these structures. Under idealized uniaxial loading conditions parallel to the layers their modelling showed a large drop in stiffness as layer curvature increased while perpendicular to the layers, the effect

is smaller but not negligible. The effect of this waviness on the mechanical properties

has been largely overlooked, with the vast majority of previous modeling efforts

assuming perfectly flat microstructures (Chawla et al., 2008, Lotfian et al., 2013, Singh

et al., 2010b). Additionally, Verma and Jaryam (Verma and Jayaram, 2014) showed that

under indentation loading normal to the film, the layer curvature increases the tensile

stresses that develop causing an increase in delamination. However, their work only

looked at the specific case of thick ceramic layers (~150 nm ZrN) paired with thin

metallic layers (~10 nm Zr), which do not show the buckling behavior observed in our

work when the layers are able to co-deform.

This work expands on the current literature by determining the deformation behavior of

metal-ceramic multilayers under loading over a range of orientations using finite element

modeling (FEM) and comparing this behavior to what is observed experimentally using

indentation in the parallel, inclined at 45º and perpendicular orientations. To my

knowledge, this has not been investigated in any nanolaminate system previously. As the

previous work by Jamison and Shen indicated that the mechanical properties of these

materials can be highly sensitive to the initial waviness, the FEM simulations in this work

utilize both idealized flat microstructures and more realistic wavy microstructures.

4.2 Materials and Experimental Procedure

Characterization of the perpendicular orientation was carried out directly on the deposited

surface without further sample preparation. For the parallel and inclined directions, a

diced wafer section, approximately 5 x 5 mm2, was mounted in epoxy such that the film

would be oriented 90 and 45 degrees, respectively, from the epoxy surface. To expose

the edge of the film for testing, the mounted sample was then ground using SiC paper of

decreasing grit sizes, and final polishing was carried out using 0.05 µm colloidal silica.

Indentations were performed using a commercial nanoindenter (Nanoindenter XP,

Agilent) equipped with a Berkovich geometry diamond tip (displacement controlled, 5

second hold time). The system was left to stabilize until the drift rate was less than 0.05

nm/s. The continuous stiffness measurement (CSM) technique was used in order to

determine the modulus and hardness as a function of indentation depth by superimposing

a small harmonic load (Li and Bhushan, 2002). Since the sample width was limited to the

multilayer thickness in the parallel and inclined cases, indentation depths were limited to

500 nm in order to minimize the contribution from the adjacent Si wafer and mounting

epoxy. To obtain accurate results from this shallow indentation depth, the dynamic

contact module (DCM) head was used, allowing higher load and displacement resolution

(Pharr et al., 2009). For direct comparison, the same 500 nm depth was used for

indentations in the perpendicular direction as well. The modulus and hardness values

were calculated in the depth range of 100-200 nm for all tests. About 15 indentations

were conducted in each of the orientations. A dual beam SEM/FIB was used to cross-

section the indentations to see the difference in deformation behavior in both directions

and to compare to FEM results.

Two-dimensional (2D) multilayer models were constructed for the finite element analysis

using the program ABAQUS (Version 6.12, Dassault Systemes Simulia Corp.,

Providence, RI). These simulations are not my own work and were perfomed by my collaborators Yang Lingwei and Jon Molina Aldareguia from IMDEA Materials and Professor Yu-Lin Shen from the University of New Mexico. However, their results provide valuable insight into my experimental work and are included for completeness and clarity.

The model geometry assumes a width and height of 10 µm and 50 µm, respectively, containing explicit 50 nm-thick layers of Al and SiC and a total of 328,000 four-noded linear plane-strain elements. Indentation was simulated by pressing a rigid angular indenter, with a half-angle of 68°, onto the top face of the material. Ten multilayer scenarios were considered: both flat and wavy layers in orientations with 0 (parallel), 10, 20, 45, and 90 (perpendicular) degree angles between the loading axis and the layer direction. The undulations in the wavy layers were modeled as a sinusoidal waveform with a wavelength of 0.5 µm and an amplitude of 15 nm. The bottom boundary was fixed in space, and the two lateral boundaries were unconstrained during deformation. The elastic-plastic properties of Al and SiC, obtained from experimental measurements, were identical to those used in a previous study (Tang et al., 2010b). The Young's moduli for Al and SiC were 59 GPa and 277 GPa, respectively, and the corresponding Poisson's ratios were 0.33 and 0.17, respectively. The yield strengths of Al and SiC were 200 MPa and 8770 MPa, respectively, with initial strain hardening for Al included leading to a constant flow stress of 400 MPa (Tang et al., 2010b).

As the true indentation modulus is unable to be calculated using the 2D plane strain model, an effective indentation modulus is calculated to approximate the true value. The effective indentation modulus was calculated through the following scaling law, obtained from dimensional analysis that:

$$S = \alpha \frac{E}{(1 - v^2)\sqrt{A}}$$

(5)

where S is the initial stiffness of the unloading portion of the simulated load-displacement curve, E and v are the elastic constants of the material, A is the indentation contact area and α is the proportionality constant obtained through an axisymmetric FE simulation of the Al/SiC nanolaminate under perpendicular loading.

4.3 Results and Discussion

Both the hardness and modulus values measured using nanoindentation show an increasing trend as the layers become more aligned with the loading axis, as shown in Table 1. Using laminate theory (Agarwal and Broutman, 1990), the elastic modulus variation with loading direction should vary according to:

$$E = E_L \left[cos^4\theta + \frac{E_L}{E_T} sin^2\theta + \frac{1}{4}\left(\frac{E_L}{G_{LT}} - 2v_{LT}\right) sin^2 2\theta \right]$$

(6)

where θ is the loading angle, E_L is the longitudinal (isostrain) modulus, E_T is the transverse (isostress) modulus, G_{LT} is the in-plane shear modulus obtained from the inverse rule of mixtures of the constituent layers and v_{LT} is the in-plane Poisson's modulus, obtained from the rule of mixtures of the constituents. The theoretical perpendicular (isostress) and parallel (isostrain) moduli are also given in Table 2. In

46

comparing the experimental and theoretical values, it is observed that the modulus is less dependent on orientation than the analytical solution, with the predicted isostrain modulus being significantly higher than the value measured using nanoindentation. This difference can be rationalized by the limitations inherent with indentation techniques as well as by the deviation from ideal flat layers in the material microstructure. Modeling helps shed light onto both of these concerns by simulating an indenter geometry as well as allowing for imperfections in the microstructure.

Table 2. Hardness and modulus values determined using nanoindentation for different orientations as well as the calculated modulus values using classical laminate theory.

Orientation	90°	45°	0°
H_{ind} (GPa)	4.8±0.4	6.1±0.2	6.9±0.3
E_{ind} (GPa)	111±8	114±3	126±4
E_{calc} (GPa)	97	100	168

As seen in the SEM image of the undeformed microstructure (Figure 20 (a)), the as-deposited layers show periodic waviness, which is an artifact of the columnar growth morphology followed by the Al layers (Singh et al., 2010a). This microstructural detail strongly affects the deformation behavior under loading conditions parallel and inclined to the layers. The waviness allows a buckling type of behavior to occur at much lower stresses than what would be expected for a perfectly flat structure because the preexisting undulations allow bending of the SiC layers to occur much more easily. This buckling behavior can be seen in the FIB cross section of the parallel (Figure 20 (b)) and inclined (Figure 20 (d)) indentations, in contrast to indentations in the perpendicular direction (Figure 20 (c)) which deform by plastic flow in the Al layers and localized shear bands.

47
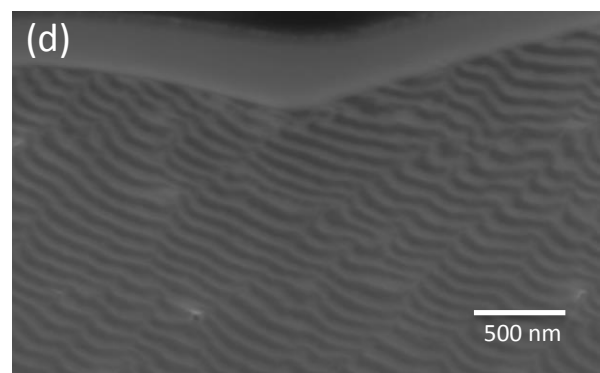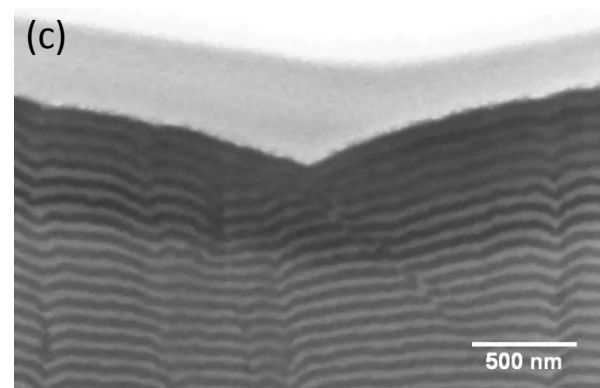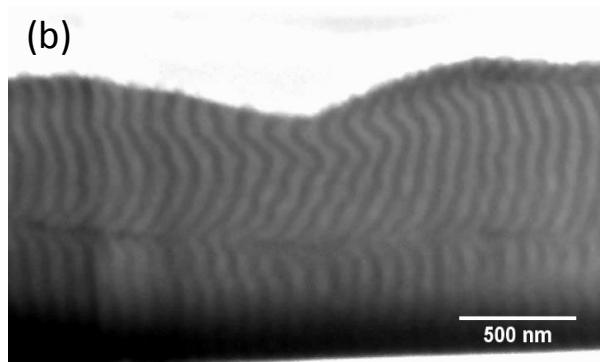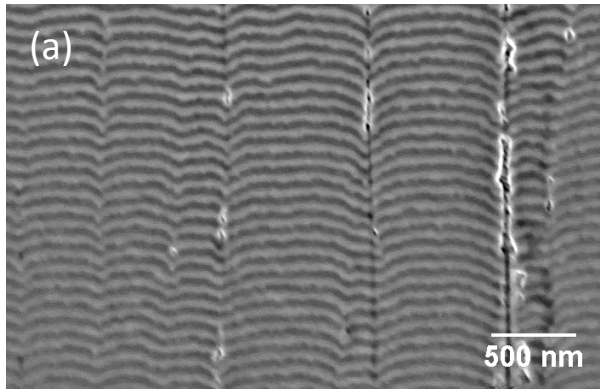
Figure 20. SEM image of the undeformed nanolaminate microstructure (a) as well as the damaged regions underneath 0° (b), 90° (c), and 45° (d) indentations.

48

This buckling behavior due to the layer waviness is also observed when modeling indentations in all orientations except the perpendicular case, as shown in Figure 21. Indentation at inclined angles showed a combination of behaviors, with the right indenter face producing buckling behavior as in the parallel orientation and the left face causing plastic flow of the Al layers as in the perpendicular orientation. In addition to changing the morphology of the deformation, this buckling behavior has a large effect on the mechanical response of the multilayer. This change in behavior due to the layer geometry can qualitatively be seen by considering the SiC layers to be curved beams, where the apparent stiffness of these beams sharply decrease under axial loading with decreased radius (Gonzalez and LLorca, 2005). As seen in Figure 22, although the waviness decreases the stiffness of the material in all orientations, the largest effect is observed around 20 degrees between the layers and the loading axis. The difference in the modeled modulus was shown to be up to 20 percent, highlighting that even small changes in the nanostructural details can have a significant impact on the resultant mechanical behavior.
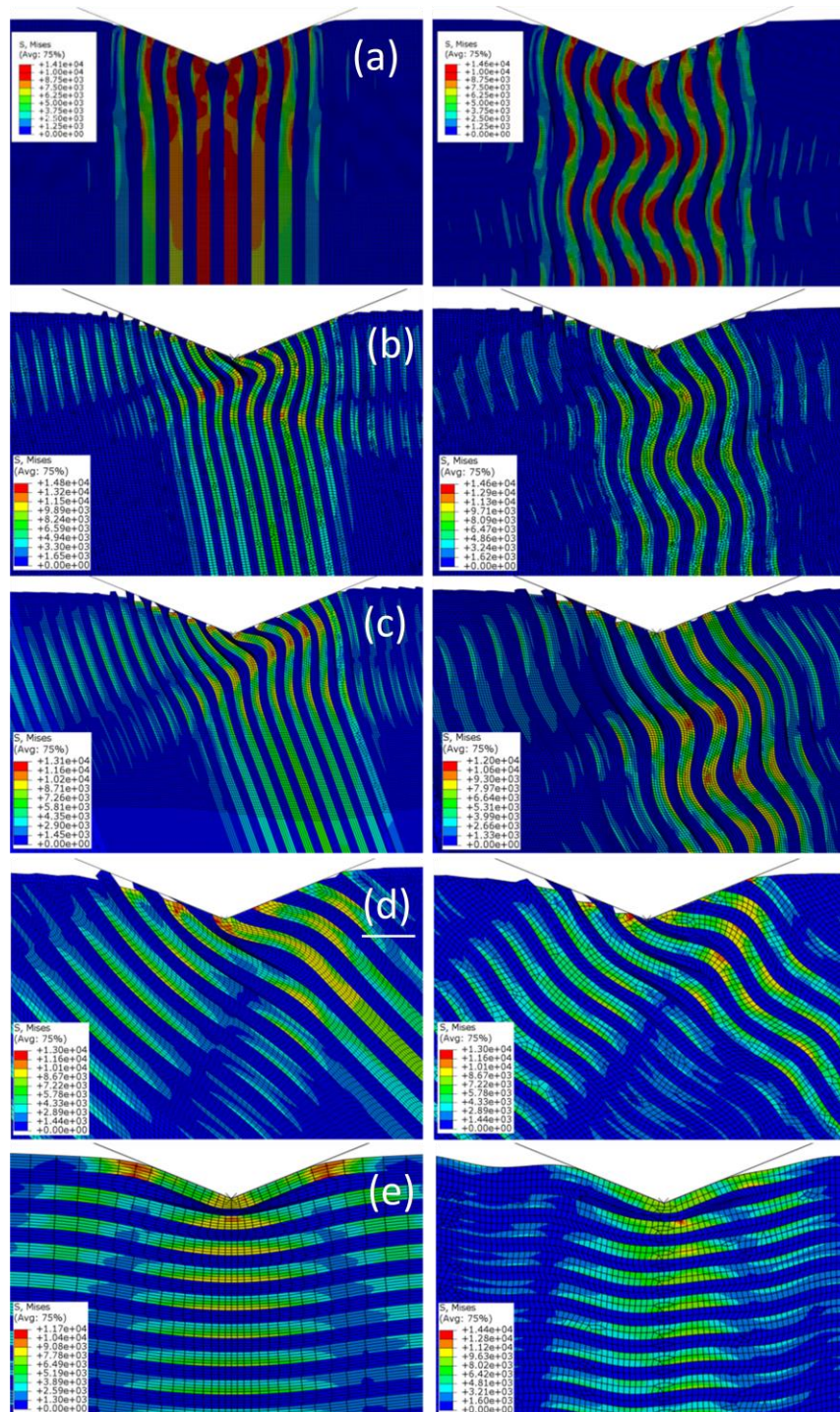
Figure 21. FEM von Mises effective stress contours of parallel indentation of flat (left) and wavy (right) microstructures for loading at 0°, 10°, 20°, 45°, and 90° (a-e respectively). The wavy microstructure shows more pronounced buckling of the layers except for the 90° case which shows little difference in behavior.
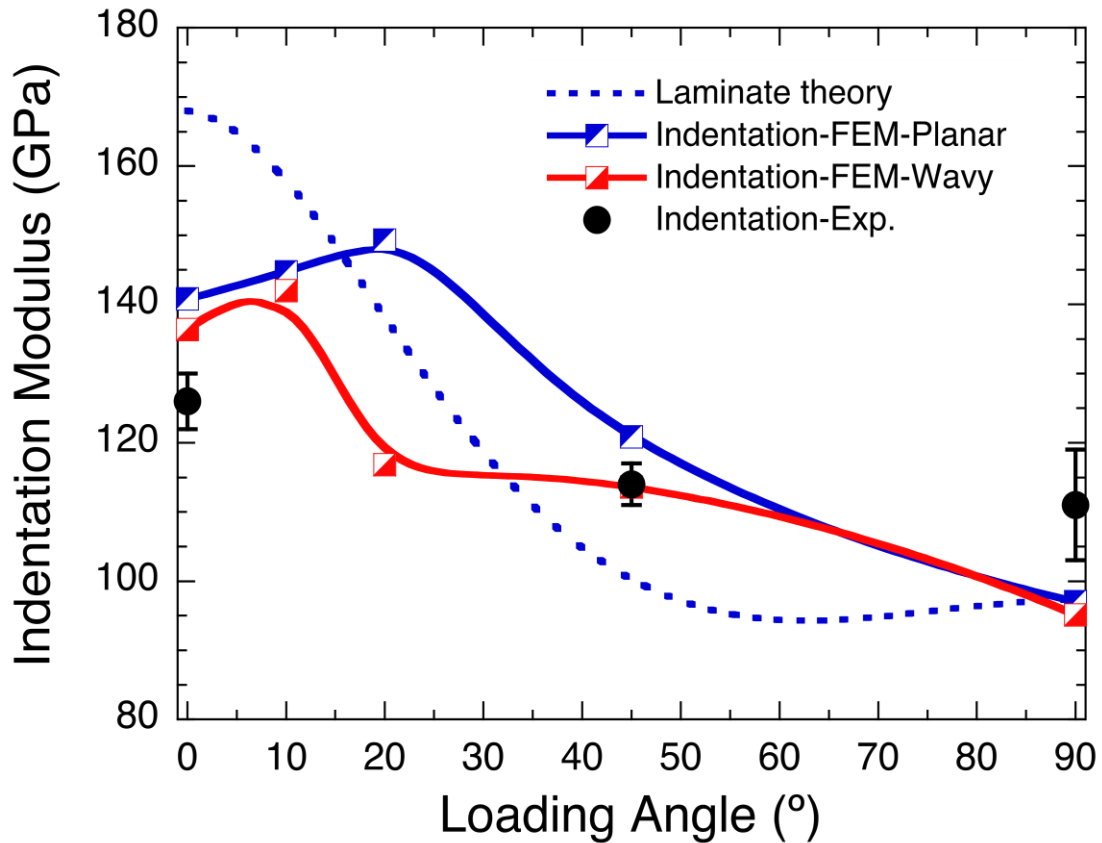
Figure 22. Effect of loading angle on relative stiffness with respect to perpendicular loading (90º). The solid lines are the predictions of laminate theory for uniaxial loading. The half full symbols represent the results of the FEM indentation simulations for planar and wavy layers and the full symbols correspond to the experimental results.

It should also be noted that although traditional laminate theory predicts that the highest modulus would be observed in the parallel indentations, FEM of small angle inclinations yield higher moduli. This is caused by the indenter geometry. Since the faces of the indenter are angled, an inclination of ~20 degrees will make the layers perpendicular to an indenter face, increasing the measured stiffness. In addition to this effect, the indenter geometry also affects the imposed stress state. In contrast to the rule of mixtures assumptions, the stress state underneath the indenter is neither uniaxial nor uniform. This

causes the overall indentation response to have some contribution from both the parallel and perpendicular directions. Therefore, it is expected that the moduli measured using indentation would fall somewhere between the moduli which would be measured using bulk techniques, which is corroborated by the experimental and FEM results showing a weaker dependence on orientation than the moduli predicted by classical laminate theory.

4.4 Summary

In summary, a combination of experimental and FEM results have shown the following for Al-SiC nanolaminate composites:

- The anisotropic behavior of these materials was characterized for the first time. The modulus and hardness in the direction parallel to the layers was shown to be greater than in the perpendicular and inclined directions.
- Due to the multi-axial stress state beneath the indenter and the laminate waviness, indentation measurements do not show as large differences between orientations as seen in the calculations based on laminate theory.
- Layer waviness predisposes the SiC layers to buckling deformation when loaded in the parallel and inclined orientations, leading to a more compliant response compared to the flat microstructure.
- Layer curvature reduces the stiffness of the multilayer in all orientations but much more drastically in the parallel and inclined orientations, especially where the layers are perpendicular to the indenter faces (~20°).

CHAPTER 5

ANISOTROPY, SIZE EFFECTS, AND ASPECT RATIO EFFECTS IN MICROPILLAR COMPRESSION OF AL-SIC NANOLAMINATES

5.1 Introduction

As shown in the preceding chapter using nanoindentation, the laminate structure of these materials gives rise to large anisotropy effects in the mechanical behavior. To characterize and understand this anisotropy, it is necessary to perform mechanical testing in various orientations. The nanoindentation results above also showed that a uniform and uniaxial stress state is required for characterizing the anisotropy of these films, conditions which can be met at the microscale by using micropillar compression.

Three orientations, with the loading axis forming 0°, 90° and 45° with respect to the layer direction, were chosen to characterize the anisotropy of the films using pillar compression. Pillars compressed perpendicular to the nanolaminate surface (90º) subject the layers to an isostress condition, while pillars compressed in the parallel direction (0º) load the layers in an isostrain condition. Finally, pillars oriented at 45° with respect to the film surface generate the largest amount of shear stresses parallel to the layers and have been utilized in other systems (Li et al., 2012) to obtain information on interfacial shear strength.

In addition to the effects of the orientation, it is also important to determine what role the pillar geometry parameters, such as pillar size and aspect ratio, plays in the deformation

behavior. The size effect phenomenon in pillar compression, where the flow stress of the materials increases as the size of the pillars is reduced, has been documented in a number of cases in single phase materials at small scale lengths (Uchic and Dimiduk, 2005, Greer et al., 2005, Chen et al., 2010, Guo et al., 2014), however this effect has not been sufficiently explored in nanostructured materials where the testing geometry is still much larger than the structural features.

Pillar compression allows the overall mechanical response of the material to be characterized, and combining this with post deformation imaging allows some information regarding the deformation mechanisms to be inferred. In addition to this, 2D finite element models (FEM) are used to provide a better mechanistic understanding of the deformation behavior of individual components. These tests provide a more comprehensive understanding of the deformation behavior of this class of material than previously available.

5.2 Materials and Experimental Procedure

Pillars were able to be fabricated on the surface of the 90º oriented sample without further sample preparation, however the 0º and 45º samples required mounting in epoxy and polishing in order to expose the edge to be tested, shown schematically in Figure 23. Pillar fabrication, post mortem imaging and cross sectioning was performed using a dual beam FIB operated at 30 keV ion beam accelerating voltage and 5 keV electron beam accelerating voltage. Pillar fabrication was performed using annular milling producing pillars as shown in Figure 23. For each orientation, pillars were milled with nominal

dimensions of 2 x 4, 2 x 6, and 1 x 2 µm (diameter by height) with a 20 µm surrounding

trench to allow clearance for the indenter. These pillar sizes were chosen in order to study

the size effect as well as the effect of aspect ratio. Various ion beam currents were used

depending on the material removal rate and precision needed, but final polishing of the

surfaces was always carried out using ion currents below 50 pA.
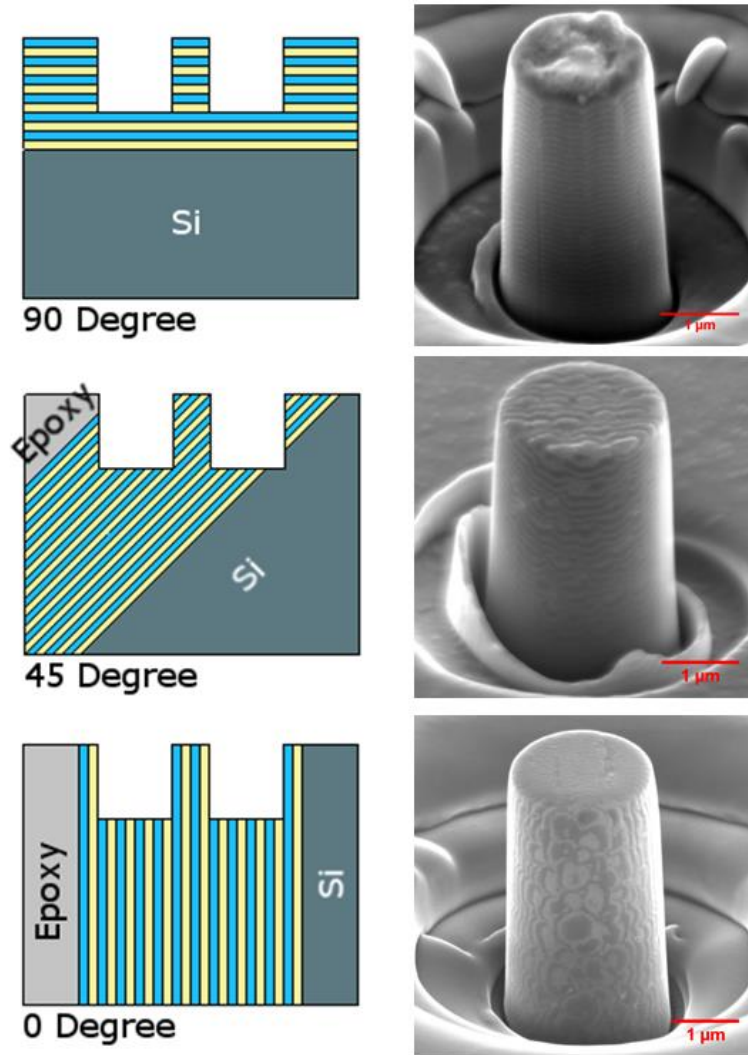
Figure 23. Schematic of the pillar orientations tested and SEM images of

2 x 4 µm pillars prior to testing.

Pillar compression was carried out using a commercial nanoindenter (Nanoindenter XP-II, Agilent) equipped with a 10 x 10 µm diamond flat punch. Samples were mounted to aluminum stubs for testing using a thermoplastic adhesive. Tests were performed using a constant displacement rates of 5, 10 and 15 nm/s for 1 x 2, 2 x 4, and 2 x 6 µm pillars, respectively, yielding an approximate strain rate of 2.5×10^{-3} s^{-1} for all tests. The drift rate for all tests was held below 0.05 nm/s.

The deformation of the micropillars was simulated by finite element modeling (FEM) using the commercial software Abaqus (Abaqus, v. 6.12, Dassault Systems Simulia Corp., Providence, R.I.). These simulations are not my own work and were perfomed by my collaborators Yang Lingwei and Jon Molina Aldareguia from IMDEA Materials and Professor Yu-Lin Shen from the University of New Mexico. However, their results provide valuable insight into my experimental work and are included for completeness and clarity.

The simulations were performed in 2D plane strain conditions. The models consisted of a rigid flat punch, micropillars with layers oriented at 0º, 45º and 90º with respect to the micropillar axis and a base material. Pillar sizes of 1 x 2, 2 x 4, and 2 x 6 µm were modeled to account for size and aspect ratio effects. To match more precisely with experimental conditions, a 2° taper was also included in the pillar models. In each case, the effect of layer waviness was accounted for by comparing the results of the simulations performed with micropillars containing flat layers, to those containing undulated layers. The undulated layers were modeled by imposing a standard sinusoidal

56

waveform with a wavelength of 0.5 µm and amplitudes of 15 and 45 nm. The 45 nm amplitude is close to the amplitude observed experimentally although there is considerable variability in the real microstructure. All the pillar models were meshed by 4-node bilinear plane strain quadrilateral meshes (CPE4) with a total of more than 29425 element, after performing a mesh convergency study. Constraint boundary conditions were imposed at the bottom of the base material, while the rest of the surfaces were set free.

The Al and SiC layers were modeled as elastic perfectly plastic materials, with no strain hardening, due to the small layer thickness, which precludes any dislocation storage. The young's modulus of Al and SiC were 70 GPa and 300 GPa, and the corresponding Poisson's ratios were 0.34 and 0.14. The yield stress of Al was 935 MPa (Yang et al., 2015), and the apparent yield stress of SiC was chosen 7 GPa, a large value estimated from nanoindentation results of 1 µm thick monolithic SiC films. The base material was modeled as pure elastic material, with the elastic modulus and Poisson's ratio estimated as an average value of the isostrain and isostress composite moduli between Al and SiC. The Al-SiC interfaces were considered perfectly bonded in all cases.

5.3 Results and Discussion

5.3.1 Effect of layer orientation on deformation morphology

Engineering stress-strain curves obtained from the pillar compression tests for different orientations are shown in Figure 24, where each plot, corresponds to a different pillar

geometry, i.e., 1 x 2, 2 x 4 and 2 x 6 µm respectively. The arrows indicate the strain to failure of the pillars.
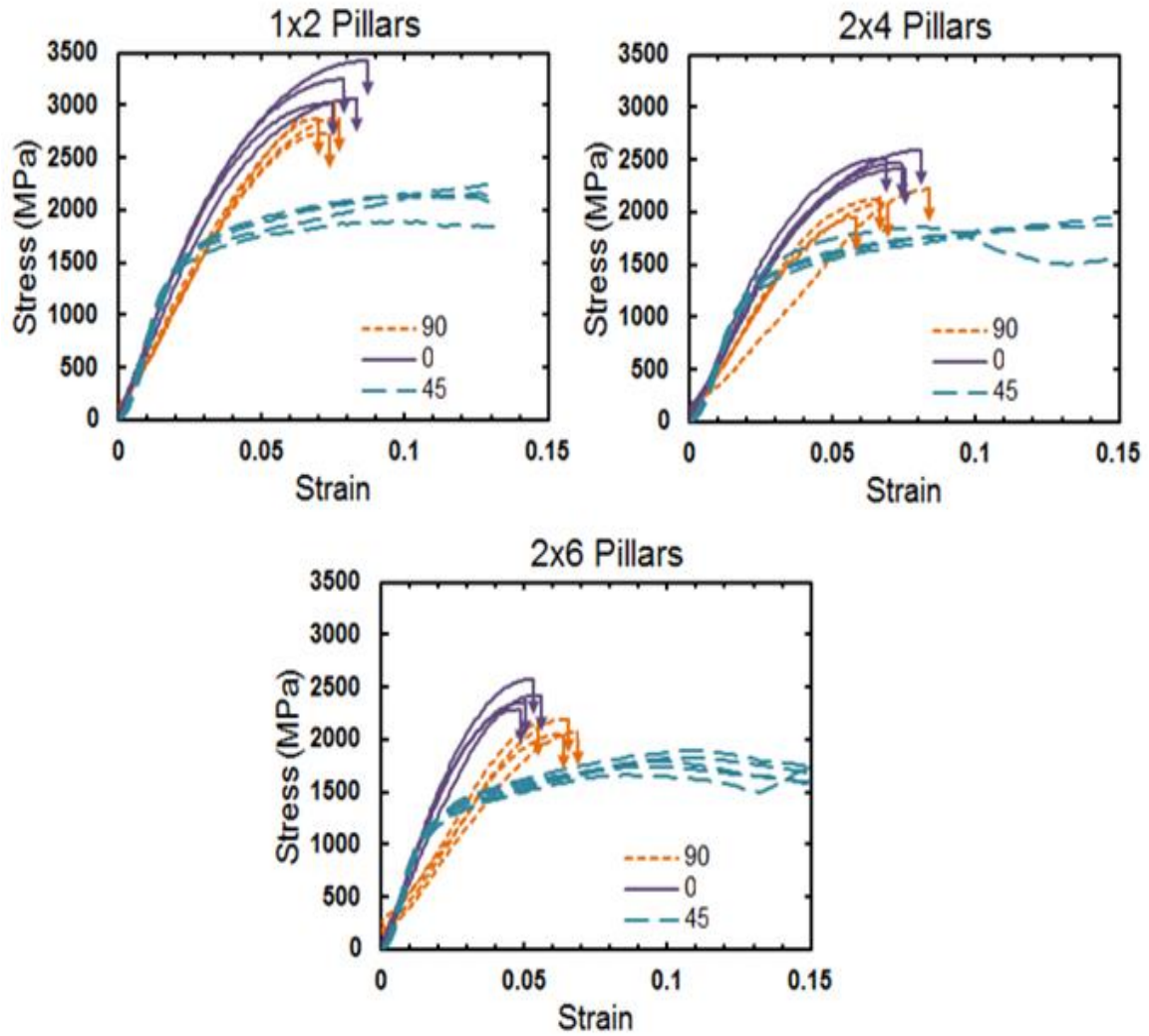
Figure 24. Experimental stress strain curves showing the effect of layer orientation on mechanical response for different geometries.

Figure 24 indicates that the relative strengths of the different orientations were fairly independent of the pillar geometry, with the 0° orientation being the strongest, the 45° orientation being the weakest, and the 90° orientation having an intermediate strength. SEM images of the pillars after deformation are shown in Figure 25. For the 0° orientation, Figure 25 (a) shows that strain localized at the top of the pillar. This localization was due to the hard SiC layers buckling under the applied load, as shown in Figure 25 (b), triggering the formation of kink bands and the complete collapse of the pillars. The formation of kink bands under parallel loading is not surprising considering the large strength difference between the Al and the SiC layers. Interestingly, bending of the layers tended to localize along pre-existing columnar boundaries within the nanolaminate microstructure, presumably because these boundaries are weaker than the rest of the material. For the 90° orientation, fracture occurred in a more brittle fashion, leading to a mushroom type deformation of the pillars, as shown in Figure 25 (c). As observed in Figure 25 (d), this deformation pattern occurs due to the formation of vertical cracks on the SiC layers, triggered by the radial tensile stresses that develop in them with the plastic deformation of the Al layers (Lauterbach and Gross, 1998). The plastic deformation of the Al layers, constrained by the SiC layers, is evident by the small extrusions that develop at the free surface, as can be seen in the lower, less strained part of the pillar (Figure 25 (c)). However, for larger strains at the top of the pillar, the SiC layers crack, and the Al layers plastically flow within the cracks, leading to the formation of a mushroom type morphology. The deformation behavior of the 45° pillars in Figure 25 (e) was also dominated by the bending of the SiC layers. As seen in cross section image (Figure 25 (f)), shear occurred predominantly in the direction normal to the layers

under the action of the applied stress, preferentially along the weaker columnar

boundaries, as indicated by the white arrows, instead of along the Al-SiC interfaces. The

latter is indicative of a very strong Al-SiC interface, as has been demonstrated elsewhere

(Mayer et al., 2015a). As a result of the shear localization along the pre-existing

columnar boundaries and the plastic deformation along the Al layers, the layers tended to

rotate with strain to become perpendicular to the applied stress. In consequence, the

layers at the top of the pillar form 60º with respect to the loading axis, as opposed to the

average angle of 45º that can be measured on the undeformed section of the pillar. As

opposed to the 0º and 90º orientations, which fail at strains of around 0.05-0.07,

depending on pillar geometry, this type of deformation allows the pillar to accommodate

large amounts of strain without collapsing, as seen in both the stress strain curves of

Figure 24 and the images of the deformed pillars.
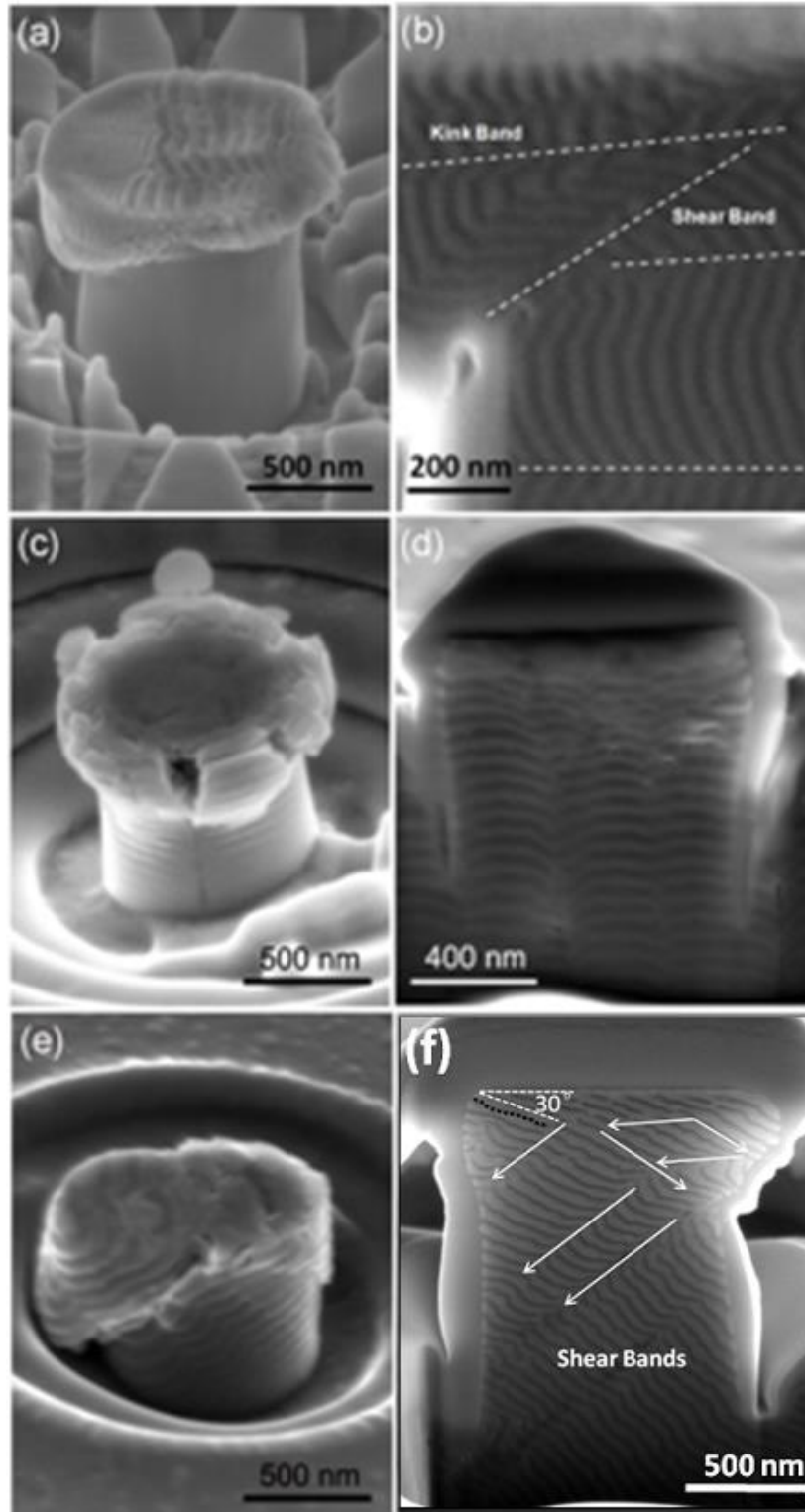
Figure 25. SEM images of 1 x 2 µm pillars and cross sections following compression for 0° (a and b), 90° (c and d), and 45° (e and f) orientations. The deformation behavior shows large differences with the 0 and 45 degree orientations being strongly influenced by the buckling of the layers.

61

5.3.2 Effect of layer waviness on deformation morphology

Overall, the results confirmed, as demonstrated before (Lotfian et al., 2013), that the nanolaminates deformed by the constrained plastic deformation of the Al layers and that the Al-SiC interface was very strong. However, the results also showed that fracture of the SiC layers, especially along pre-existing columnar boundaries, was the main mechanism responsible for the final failure. And moreover, that the failure pattern was very sensitive to the loading direction, with micropillars oriented at 0º and 45º mainly collapsing by the buckling of the SiC layers, and the micropillars oriented at 90º failing by their transverse cracking. It is well known that buckling is very sensitive to vertical alignment, so it was expected that the layer waviness present in the microstructure should have a strong influence on the failure strain. In order to assess the effect of layer waviness on deformation morphology, the results of FEA simulations utilizing micropillars with undulated and flat layers are compared in Figure 26 for the different loading directions. The figures on the left correspond to the von Mises stress contours micropillars with flat layers, while the figures on the right are those with undulated layers for a waviness amplitude of 45 nm. The simulated stress-strain curves for flat and undulated layers are also compared in Figure 27, where the experimental results of a 2 x 4 pillar is also plotted for reference. Comparing the results for the pillars loaded at 0º, it is evident that the layer buckling at the top of the pillar encountered experimentally was only reproduced by the simulations considering undulated layers in Figure 26(b). Moreover, the stress-strain curve of the simulation with undulated layers predicted a maximum in the stress in Figure 27(a) (denoted by arrows), as a consequence of the buckling of the layers, as experimentally observed. Analogously, the simulations of

62

pillars loaded at 45º also showed a very different behavior for flat and undulated layers. For flat layers, shear predominantly occurred parallel to the layers, resulting in little strengthening contribution from the SiC layers, whereas undulation of the layers resulted in significant longitudinal compressive stress on the SiC layers to trigger buckling, leading to the formation of shear bands perpendicular to the layers and domains where the layers are substantially rotated towards the applied stress. Moreover, while the stress strain curve for flat layers of Figure 27(c) showed very little strain hardening, in agreement with the strain localization observed along some of the Al layers in Figure 26(e), the stress-strain curve for undulated layers displayed an increase in apparent strain hardening rate, in agreement with the experimental observations. Finally, in the case of the 90° loading direction, the results of the simulations with flat (Figure 26(c)) and undulated (Figure 26(d)) layers were very similar, as well as the predicted stress-strain curves (Figure 27(b)), indicating little effect of the layer waviness when loading perpendicular to the layers.
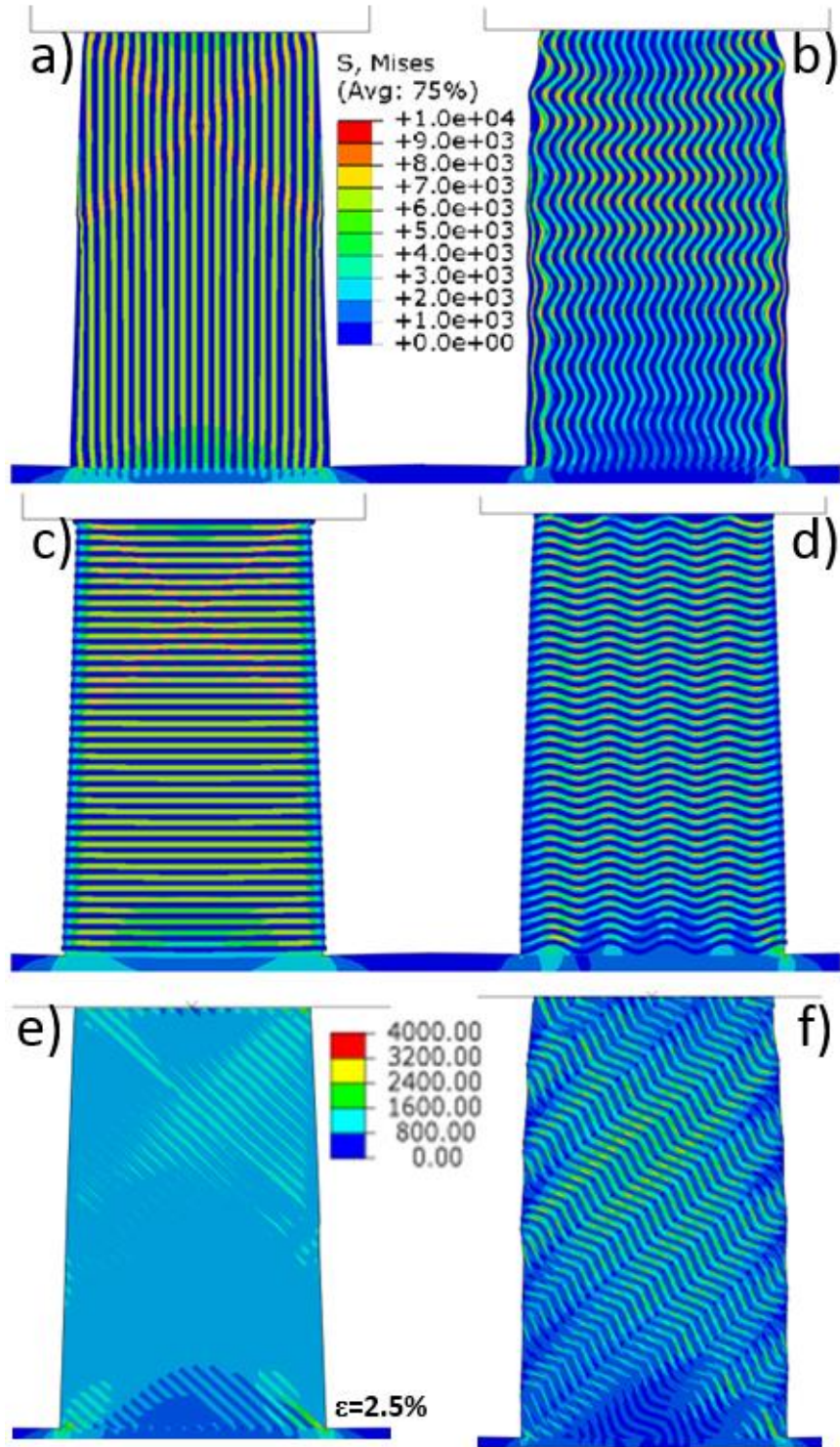
Figure 26. FEA stress contours at 6% strain showing the effect of 0 nm (a, c, and e) and 45 nm (b, d, and f) amplitude waviness on the deformation behavior for all three orientations. Due to lack of convergence e) is only able to be modeled to 2.5% strain (also note the difference in contour levels).
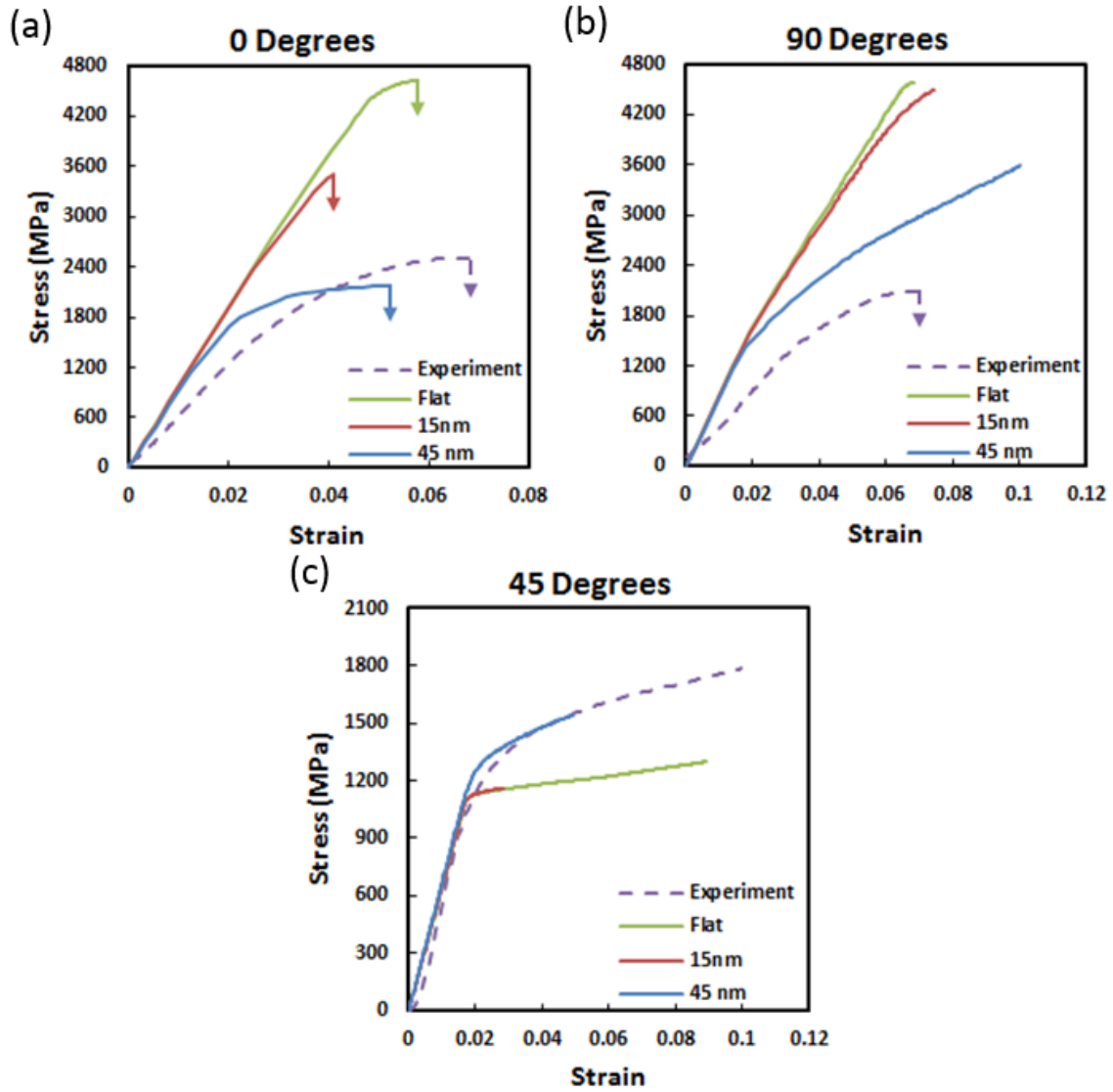
Figure 27. Comparison of 2 x 4 µm pillar behavior to FEA simulations having waviness amplitudes of 0, 15 and 45 nm in each orientation.

Although the modeled stress-strain curves for the three orientations (Figure 27) show a qualitative agreement with the experimental ones, quantitatively there are discrepancies. On top of several model assumptions that undoubtedly affected the simulation results, like the consideration of plane strain loading or the ideally sinusoidal waviness assumption, this is mainly due to the fact that the models did not account for fracture of the SiC layers, which occurred profusely at the last stages of deformation. As a matter of fact, it is interesting to note that, for instance, for loading at 90º the simulations reproduced the large initial strain hardening rate observed experimentally, even though the Al was assumed perfectly plastic. As shown before (Lotfian et al., 2013), this is a consequence of the constraint imposed by the SiC layers on the plastic deformation of the Al layers, which lead to a buildup of hydrostatic stresses and an increase in the uniaxial applied stress required for yield. However, experimentally this behavior was limited by cracking of the SiC layers, leading to a maximum stress prior to failure that was not reproduced by the simulations.

5.3.3 Pillar size effect

Figure 28 summarizes the effect of pillar size and aspect ratio on the stress-strain curves as a function of layer orientation. A non-negligible size effect could be observed for all three orientations, with the 1 x 2 µm pillars having significantly higher fracture strengths than the 2 x 4 µm pillars. The Student's t test was used to determine the significance of the difference; given the fracture strength distributions and limited number of tests, the probability that there was no difference in the 1 x 2 and 2 x 4 µm pillar fracture stress was <0.01%, 0.11%, and 1.8% for the 90°, 0°, and 45° orientations respectively, which

are all considered statistically significant. Size effects have been observed in micropillar testing of other materials, especially when testing single crystals of pure metals (Guo et al., 2014, Greer and Hosson, 2011, Zhang et al., 2014). Dislocation starvation and the lack of dislocation sources have been proposed as the cause of this strength increase in other works (Greer et al., 2008, Volkert and Lilleodden, 2006) however this mechanism is not likely the cause of the strengthening in the case of nanolaminates. While dislocations slip more or less unimpeded and leave the surface in the case of single-crystal micropillars, the interfaces represent strong barriers for dislocation transmission (Tschopp and McDowell, 2008), forcing them to glide confined within single layers (Misra et al., 2005). Considering that the layer thickness is significantly smaller than the pillar diameter, it is unlikely that plasticity in the Al layers is affected by the pillar size.
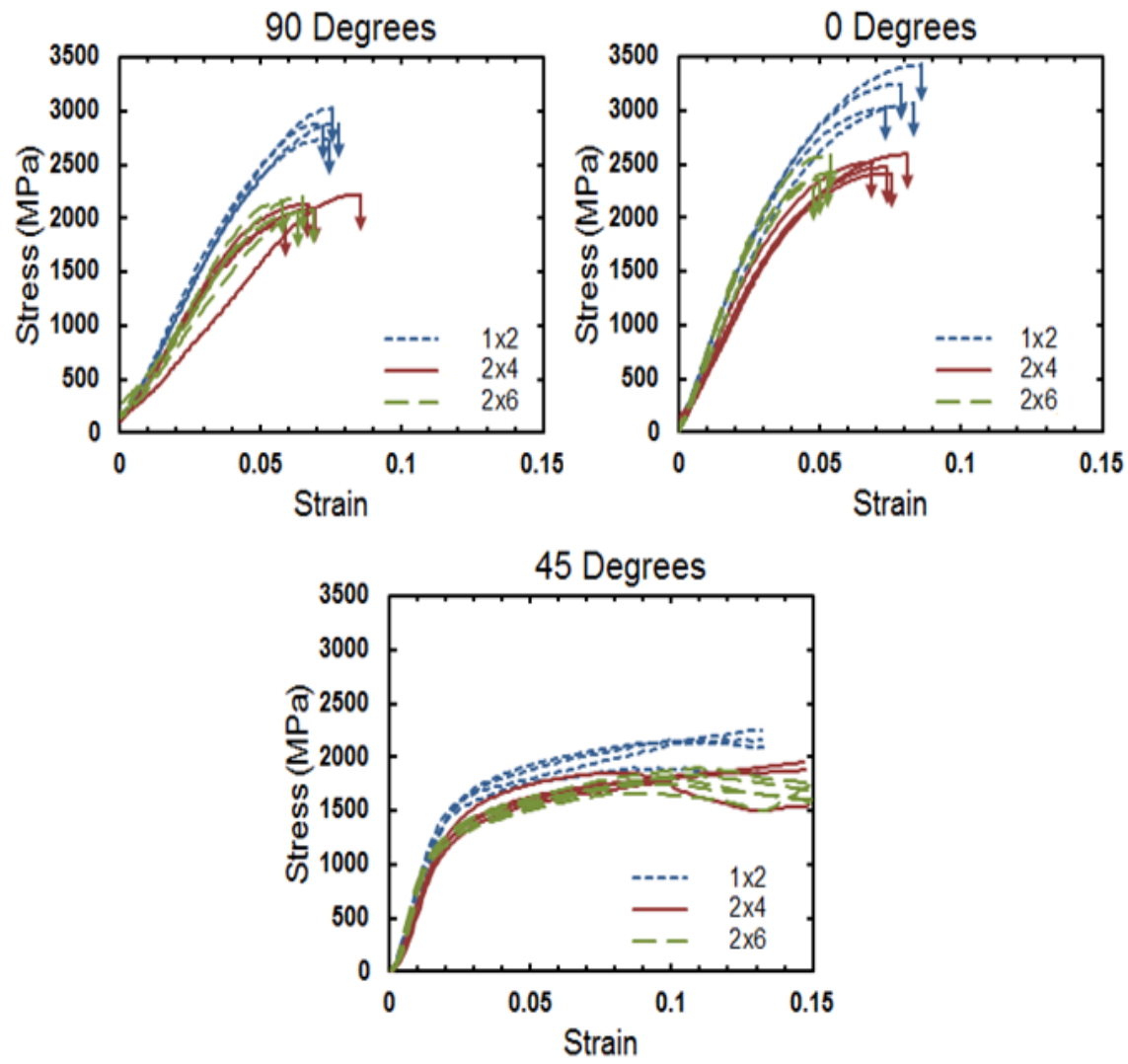
Figure 28. Experimental stress-strain curves showing the effect of pillar size and aspect ratio on mechanical behavior.

In addition to dislocation starvation, size effects could also arise from artifacts of the FIB fabrication process, as smaller pillars would contain a larger proportion of FIB damaged material. However this is not likely in this system, as discussed in Chapter 2, because TEM observations only show a few nm amorphized layer and no dislocations near the FIB surface. Additionally the deformation shows a significant and approximately equal amount of plasticity even at small pillar sizes where Ga embrittlement would presumably be highest.

Another possible mechanism for the strengthening due to the limited size pillars that has not been proposed before and that would be intimately linked to the observed cracking of the SiC layers is the initial distribution of flaws within each micropillar. This type of size effect has been studied extensively in the ceramics literature using Weibull statistics (Danzer et al., 2007), where the materials fracture strength decreases in larger samples because there is a higher probability for the sample to contain a strength limiting flaw. Although this approach is most often used in tensile or bending tests, the same type of analysis has been successfully applied to compressive failures as well (Huang et al., 2014, Wong et al., 2006). One caveat to using this analysis for compressive loading cases is that cracks could be propagated though mode I cracking in the case of wing cracks or mode II cracks due to the resolved shear stress at 45°. As our study is only concerned with determining if the apparent size effect can be attributed to a distribution of flaws, as long as the type of crack propagation is consistent in all pillars used in the analysis, the cracking mode should not affect the dependence on the pillar size.

69

There are indications which support the idea of a preexisting flaw based failure

mechanism in these pillars leading to a size effect. Firstly, porosity is observed in these

laminates (Singh et al., 2010b, Mayer et al., 2015a), often in the troughs of the layer

waviness where the uneven surface can cause shadowing during the deposition.

Secondly, the largest size effect is observed in the 90° orientation, where the fracture

behavior appears the most brittle (Figure 25(c)), while the effect is greatly reduced in the

45° oriented pillars, which deform predominantly by plastic shear of the Al layers. To test

this hypothesis, 11 additional pillars of both the 1 x 2 and 2 x 4 µm 90° orientation were

made using the same procedure outlined above in order to have an acceptable sample

size. Each pillar was strained to failure and the fracture stress was recorded (for

consistency across all tests this was taken to be the first instance where the hardening rate

becomes negative). The fracture stress values were assigned a probability of survival

based on the proportion of pillars which failed at a lower stress. The two parameter

Weibull distribution function can relate this probability of survival, Ps, to the fracture

stress, σ, and the sample volume, V, according to the following equation:

$$P_S = exp\left[-\frac{V}{V_o}\left(\frac{\sigma}{\sigma_o}\right)^m\right] \tag{7}$$

where m is the Weibull modulus and the constants Vo and σo are the characteristic

volume, and the characteristic strength, respectively (Danzer, 2006). Algebraic

manipulation of this equation yields the linear form:

$$\left[\ln\left(\ln\left(\frac{1}{P_S}\right)\right) - \ln V\right] = m[\ln \sigma] + \left[\ln\left(\frac{1}{V_o}\left(\frac{1}{\sigma_o}\right)^m\right)\right] \tag{8}$$

Plotting the fracture strengths according to this form yields Figure 29. This plot clearly

shows that both the 1 x 2 and 2 x 4 µm data fall on a single linear trend. Therefore, the

fact that the mean strength of the 1 x 2 µm pillars is higher than that of the 2 x 4 µm

pillars can be completely accounted for using the volume term in the Weibull equation.

This indicates that at smaller pillar sizes there is a lower probability of the pillar

containing a strength limiting flaw, increasing the apparent strength, and the increase is

not due to FIB damage or a dislocation based size effect. The small amount of

nonlinearity in the 2x4 pillar data is characteristic of a bimodal flaw distribution as seen

in other work (Danzer et al, 2007). Appendix A, which characterizes the tension

compression asymmetry of these materials provides additional support to this theory.
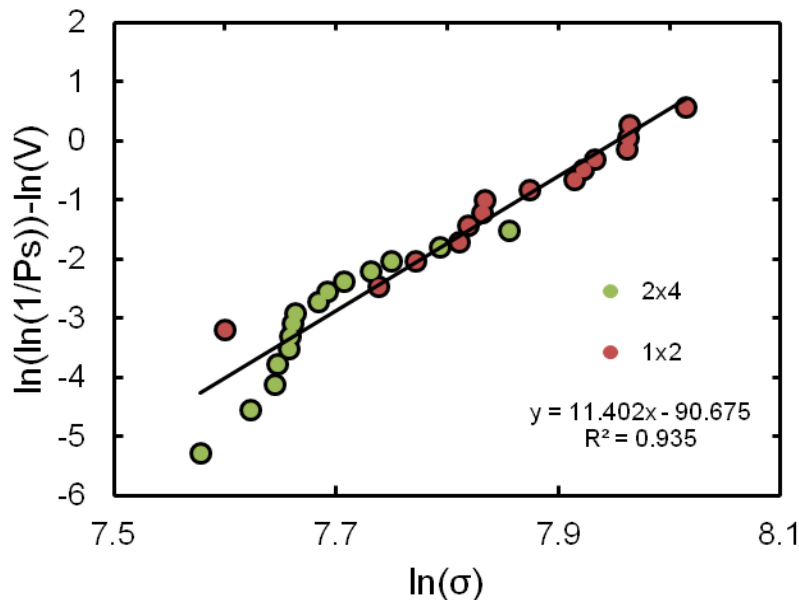
Figure 29. Weibull plot of the fracture stresses of 1 x 2 and 2 x 4 µm pillars (in the 90° orientation). The

fact that both sets of data fall on a single linear fit line indicates that the increase in mean strength of the 1 x

2 µm pillars can be attributed to lower probability of a strength limiting flaw and is not due to FIB damage

or a true material size effect.

5.3.4 Pillar aspect ratio effects

Finally, by comparing the 2 x 4 and 2 x 6 µm pillar stress-strain curves shown in Figure 28, it can be concluded that in general there is little effect on the mechanical behavior due to altering the aspect ratio. The one notable exception to this is the 0° orientation. Although the fracture stresses for the two geometries are statistically equivalent in this case as well, the fracture strain is substantially smaller in the 2 x 6 µm case. FEA was used to simulate the deformation in both geometries, as shown in Figure 30. The modeling results also displayed a decrease in the strain to failure at larger aspect ratios. This difference stems from the buckling deformation behavior seen in the 0° orientation. Buckling deformation is a type of plastic instability, the extent of which is determined by the geometry of the initial waviness. This leads to the buckled region having the same height in both modeled geometries (Figure 30). Therefore, in the case of the high aspect ratio pillars, the wavelength is a smaller proportion of the overall pillar height, leading to a smaller apparent strain before failure.
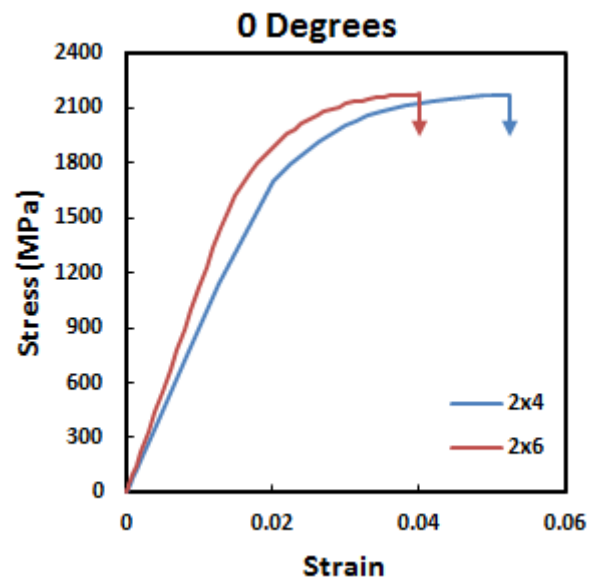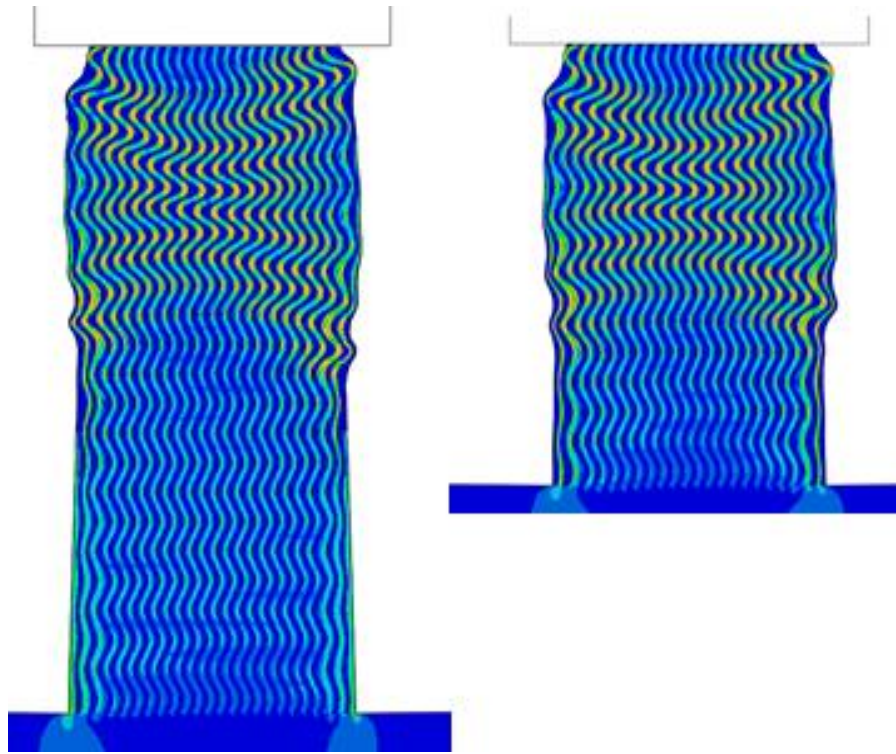
Figure 30. Simulated deformation behavior of 2 x 6 and 2 x 4 µm pillars (same contour scale as Figure 26) showing that the height of the instability is independent of the overall pillar height. This leads to a decreased apparent strain to failure, as shown in the stress-strain curve.

5.4 Summary

In this work, the effects of orientation, pillar geometry, and layer morphology were investigated though a combination of experimental observations and FEA. In light of the results obtained, the following conclusions can be made:

- The 0° orientation shows the highest strength because the reinforcing SiC layers are aligned with the loading axis while the 45° orientation shows the lowest strength because it accommodates shear deformation more easily.

- The deformation behavior in the 0° and 45° orientations is highly dependent on the waviness of the layer structure because deformation is limited by bending and buckling of the layers.

- The maximum strength of the 90° orientation is limited by cracking of the SiC layers.

- A size effect is observed in all orientations, but more predominantly in the 0° and 90° orientations. Using a Weibull statistics approach, it was shown that the difference in strength can be attributed to the lower probability of the smaller pillars containing a strength limiting flaw.

- An aspect ratio effect is observed in only the 0° orientation where the failure strain decreases at higher aspect ratios. This is due to the majority of the deformation being accommodated by a buckling type of plastic instability, the size of which is not related to the pillar height, but to the geometry of the existing layer undulation.

CHAPTER 6

3D CHARACTERIZATION OF AN AL-SIC MULTILAYER NANOSTRUCTURE USING FIB TOMOGRAPHY AND ITS IMPLICATIONS TOWARDS MECHANICAL BEHAVIOR

6.1 Background

An ever growing body of literature is focused on nanolaminate materials both because of their potential applications and because they allow a unique opportunity to study the deformation mechanisms of materials at the nanoscale under an extremely high degree of constraint. Due to this interest in these deformation mechanisms, many of these research efforts also utilize a significant amount of modeling to help provide a better understanding of the mechanical behavior. The vast majority of this literature assumes a perfectly flat nanostructure (Singh et al., 2010b, Lotfian et al., 2013, Tang et al., 2010b, Liu et al., 2013a), which is not representative of the actual nanostructure, as seen in Figure 31. Some more recent studies have begun implementing non-ideal structures to account for this, for example layers with sinusoidal waviness (Mayer et al., 2016a, Mayer et al., 2016b, Jamison and Shen, 2015, Jamison and Shen, 2014) or arc segment waviness (Verma and Jayaram, 2014).
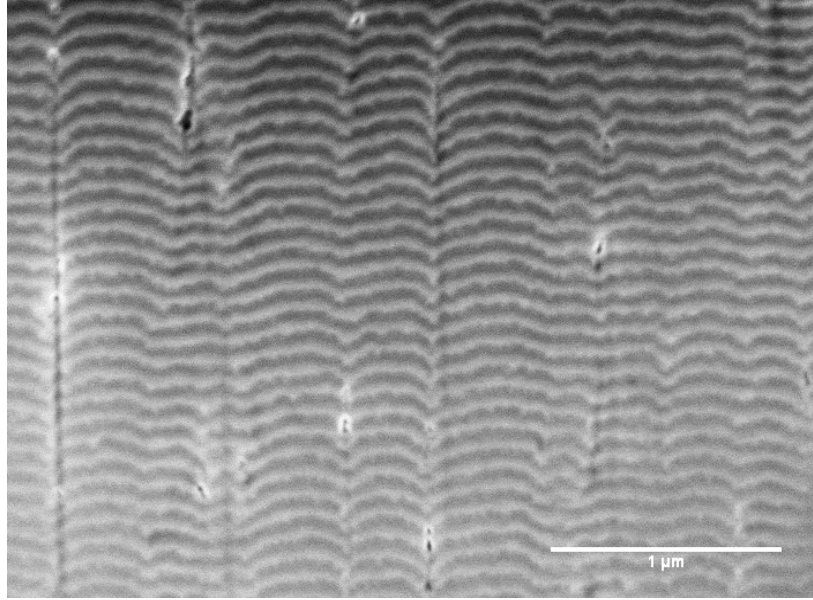
Figure 31: SEM image of nanolaminate nanostructure, showing significant waviness in the deposited layers.

Finite element (FE) modeling based off of experimentally determined microstructures can provide more accurate results as well as insights into the deformation behavior which can be overlooked using simplified structures (Qidwai et al., 2009, Chawla et al., 2006, Sidhu and Chawla, 2006). A variety of experimental methods are available to characterize materials in 3D. These techniques range from relatively course techniques such as serial sectioning (Sidhu and Chawla, 2006) to sub-micron resolutions available with x-ray computed tomography (Singh et al., 2016) to individual atom locations determined by atom probe tomography (Weber et al., 2016). The length scales of interest in these materials makes focused ion beam (FIB) tomography the most appropriate compromise between the required resolution and volume of material which can be characterized. This technique utilizes a dual beam FIB/SEM to image the structure with a high resolution SEM while sequentially removing thin slices of material with the FIB, as shown in Figure

76

32, allowing nanometer scale resolution. Additionally, FIB tomography allows tens of cubic microns of material to be characterized, which is large enough to directly compare models to pillar compression experiments carried out in Chapter 4. In general however, the amplitude and wavelength of the waviness varies from sample to sample depending on the exact processing parameters, layer thicknesses, and materials used, making it impractical to experimentally determine the microstructure in 3D for every permutation of sample.
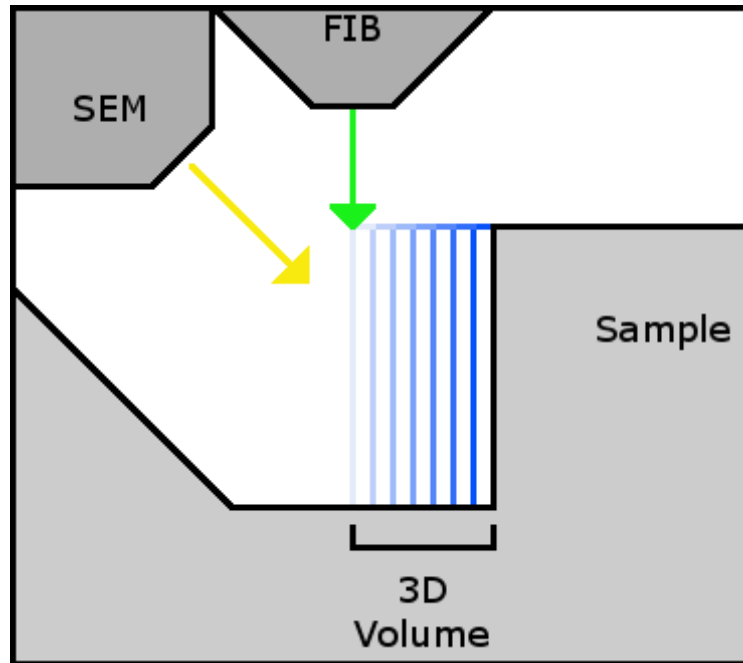
Figure 32: Schematic representation of the FIB tomography process.

Due to this limitation, the aim of this work is to determine how appropriate perfectly flat, sinusoidal, and arc segment nanostructures are for modeling the deformation of these laminate structures. By comparing these simplified structures to the experimentally determined structure obtained using FIB tomography and the experimental pillar compression results, it is possible to determine which idealized structure provides the

most accurate approximation of both the constitutive stress strain relations as well as the localization of stresses within each structure. This will help to inform future research on these multilayer systems as to the most accurate approximation as well as the error these approximations are expected to induce.

6.2 Materials and Experimental Procedure

FIB tomography was carried out in a Nova200 dual beam FIB/SEM. Approximately 5 μm x 5 μm cross sections were imaged following each milling step. Slices of 80 nm each were removed in each step using the FIB. A total of 23 slices were imaged for a total depth of 1.84 um. These slices were then manually aligned using the Avizo Fire (VSG, Burlington, MA) software. A volume of 3.20 μm by 3.53 μm by 1.84 μm was cropped from these aligned slices in in order to both remove the misaligned edges as well as provide a volume of material with maximum contrast.

Before the 3D volume characterized using FIB tomography could be utilized in a FE model, the Al and SiC phases needed to be segmented in each of the 2D slices. As the contrast differences in the raw images were not adequate for grayscale thresholding immediately, Image J (Bethesda, MD) was used to implement a variety of image manipulations in order to improve the image quality, the outline of which are shown in Figure 33. First, in order to remove the background contrast variations, a Gaussian blur was applied to the image and then this blurred image was subtracted from the original. The radius of this Gaussian blur was adjusted to the minimum size where any feature of interest is not visible in the blurred image, in this case 50 nm. Since the features of

interest in this case were the horizontal layered structure, a mask was applied to the Fourier transform of the image in order to remove much of the noise without affecting the horizontal features. This process provided images which were able to be segmented using standard grayscale thresholding. Due to contrast differences, areas immediately surrounding pores in the material required manual adjustment to ensure layer continuity. As the slice thickness was much larger than the x and y pixel size, the image stack resulted in non-cubic voxels. In order to obtain uniform cubic voxels, the 3D volume was resampled with layer positions were interpolated linearly between the slices. Avizo Fire was then used to generate a 3D solid tetrahedral mesh of the structure.
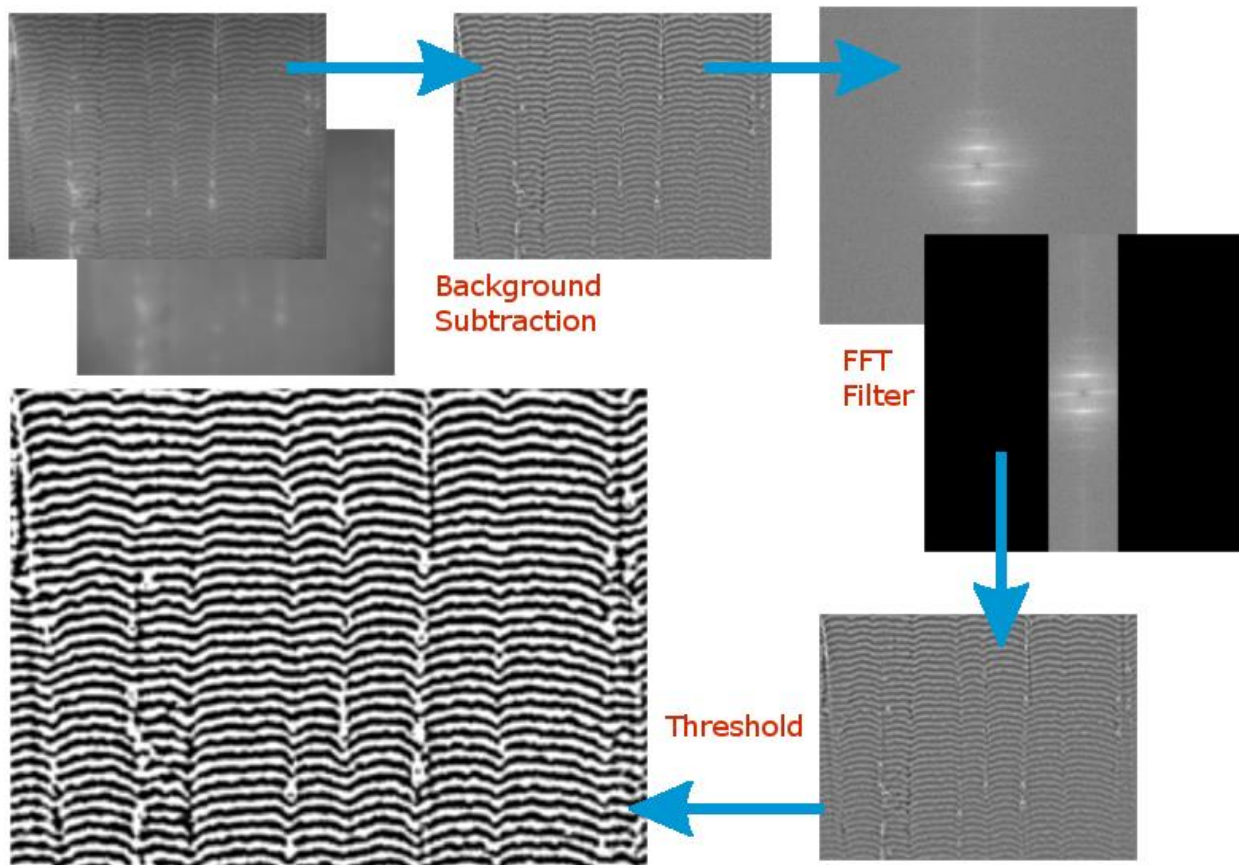
Figure 33: Outline of the image processing steps used to segment the Al and SiC phases from the raw images.

79

Three simplified nanostructure geometries, with layers consisting of either flat, cosine or arc sections, were developed in order to approximate the experimental structure. Using a single cross sectional image, the average amplitude and wavelength of the undulations were measured to be 50 nm and 475 nm, respectively. Equivalent amplitude and wavelength values were used while generating the cosine and arc section based geometries.

In order to emulate experimental pillar compression studies, 1 μm diameter by 2 μm height pillars were cropped from each of the geometries as seen in Figure 34. A 2° taper was also incorporated in the pillar models, as seen experimentally in Chapter 4. In each of the models the layers were oriented parallel to the loading axis, as this orientation showed the strongest dependence on the layer waviness in Chapters 3 and 4.

Figure 34: Pillar models used with flat, cosine, arc segment, and FIB derived nanostructures (respectively from left to right). Al layers are depicted in green while SiC layers are depicted in gray.

The deformation of the micropillars was simulated by FE modeling using the commercial software Abaqus (Abaqus, v. 6.12, Dassault Systems Simulia Corp., Providence, R.I.). All the pillar models were meshed using 4-node tetrahedral elements (C3D4). To determine the number of elements required for mesh convergence, the cosine geometry mesh was iteratively refined in ~100,000 element steps until deviations in the peak load was determined to be less than 1% from the previous iteration, which occurred at ~600,000 elements. This element count was used for the cos, arc and flat geometries, while the FIB derived mesh generated from the Avizo Fire program contained ~1,000,000 elements. The bottom surface of the pillar was completely constrained while the top surface was constrained in the x and z dimensions and displaced as a function of time in the y dimension in order to induce the deformation. Displacement was carried out at a rate of 2 nm/s to a maximum of 200 nm, corresponding to an initial strain rate of 0.001 s^{-1} and a maximum strain of 0.1. During loading, this set of constraints is analogous to displacement controlled micropillar compression with a rigid indenter that has infinitely high friction. A deformable base material was excluded from all models because this additional source of compliance has already been accounted for using the Sneddon correction (Singh et al., 2010b) in the experimental results being using for comparison (Mayer et al., 2016a).

The constitutive behavior used for the Al and SiC phases has been utilized in previous studies (Tang et al., 2010b, Tang et al., 2010a) and was approximated from the results of indentations made on 1 μm thick monolithic films of each phase, using the same deposition parameters. For the aluminum phase, the elastic modulus and poisson's ratio

were 59 GPa and 0.33, respectively, with an initial yield point of 200 MPa. A piecewise

hardening behavior following yield was used with linear hardening between (stress,

plastic strain) points of (200 MPa, 0), (300 MPa, 0.5), and (400 MPa, 3), followed by

perfectly plastic behavior. For the SiC phase, the elastic modulus and poisson's ratio was

277 GPa and 0.18, respectively. A yield point of 8770 MPa was chosen, followed by

perfect plasticity. Although the brittle SiC is not expected to undergo significant

plasticity experimentally, unrealistically high stresses occur using purely elastic behavior

due to the lack of fracture incorporated into the models. Therefore, allowing perfectly

plastic deformation after a high yield point estimated from the indentation hardness

allows for a closer approximation of the actual behavior.

6.3 Results and Discussion

A comparison of experimental pillar compression curves with the simulated result from

the FIB microstructure is shown in Figure 35. It can be seen from Figure 35 (a), the initial

loading slope in the experimental stress strain curves is much lower than the modeled

behavior. This lower apparent modulus has also been seen in previous studies when

comparing the modulus calculated using the stress strain curve and the continuous

stiffness measurement (CSM) based modulus (Singh et al., 2010b). The root of this

difference is imperfect contact between the flat punch indenter and the top surface of the

pillar, which can be caused by surface roughness or slight angular misalignment. The

imperfect contact results in an underestimation of the contact area during initial loading

and therefore the stress strain curve appears more compliant. Therefore, comparison of

the stress vs plastic strain is more appropriate and results in a much stronger agreement

between experiment and modeled response as seen in Figure 35 (b). The experimental

pillar compression results are inherently load controlled, resulting in large displacement

jumps at fracture events or plastic instabilities. Therefore, for the purpose of this study,

failure is defined at the first instance of a negative hardening rate and denoted by a

downward arrow.

Stress strain curves and corresponding frames showing the Von Mises stress contours for

the flat, cosine and arc segment, and FIB structures are shown in Figure 36 - 29,

respectively. The fully deformed pillars using the experimental and arc segment

structures (Figure 38 and Figure 39 (c)) show significant buckling of the layers in a single

localized region. This is also observed experimentally (Mayer et al., 2016a), although the

lateral constraint imposed on the top surface of the modeled pillars likely reduces this

effect. Directly comparing the stress strain curves from each of the models indicates that,

based on the overall mechanical response, the arc segment based nanostructure is the best

approximation of the experimentally determined structure, as seen in Figure 40.
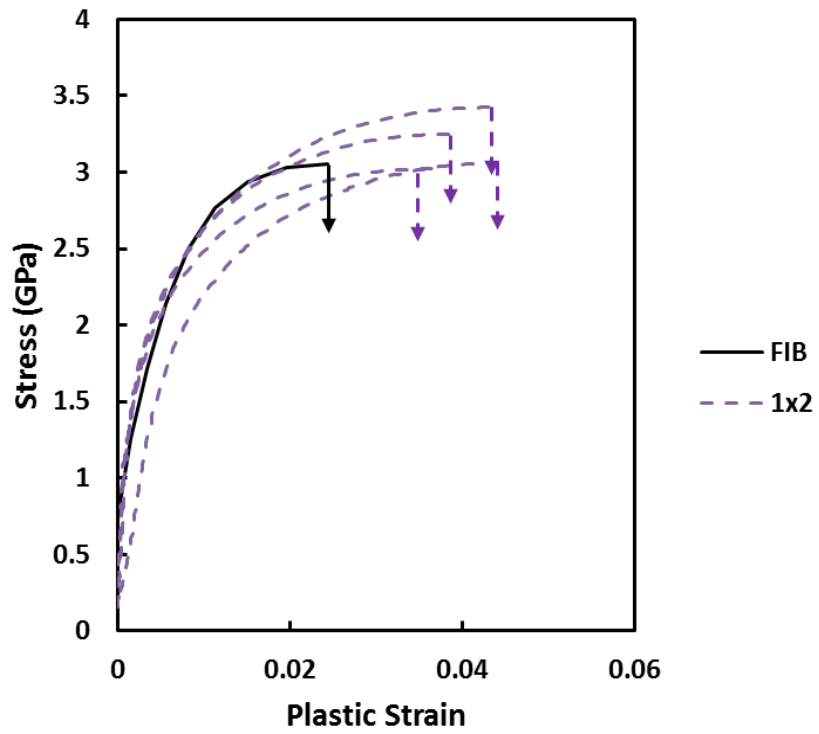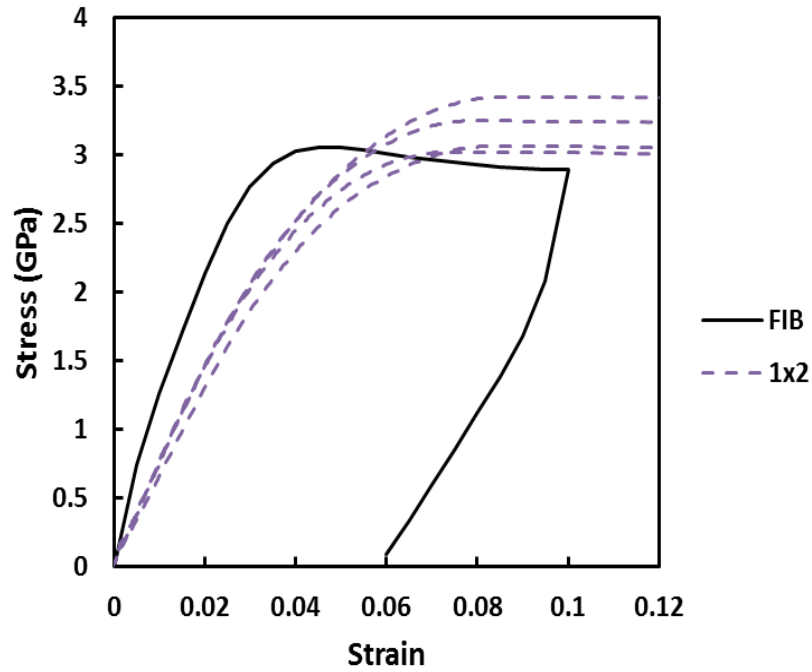
Figure 35: Comparison of experimental pillar compression response (Mayer et al., 2016a2016) to the modeled response using the FIB tomography derived nanostructure. Stress vs plastic strain response shows much stronger agreement due to the low apparent modulus in pillar compression experiments.
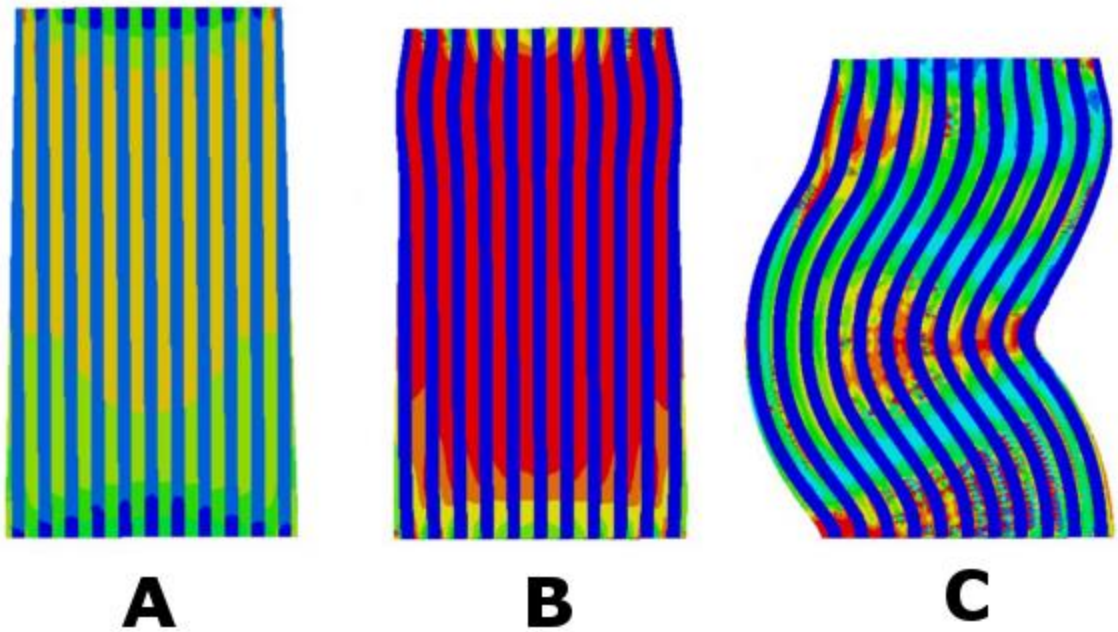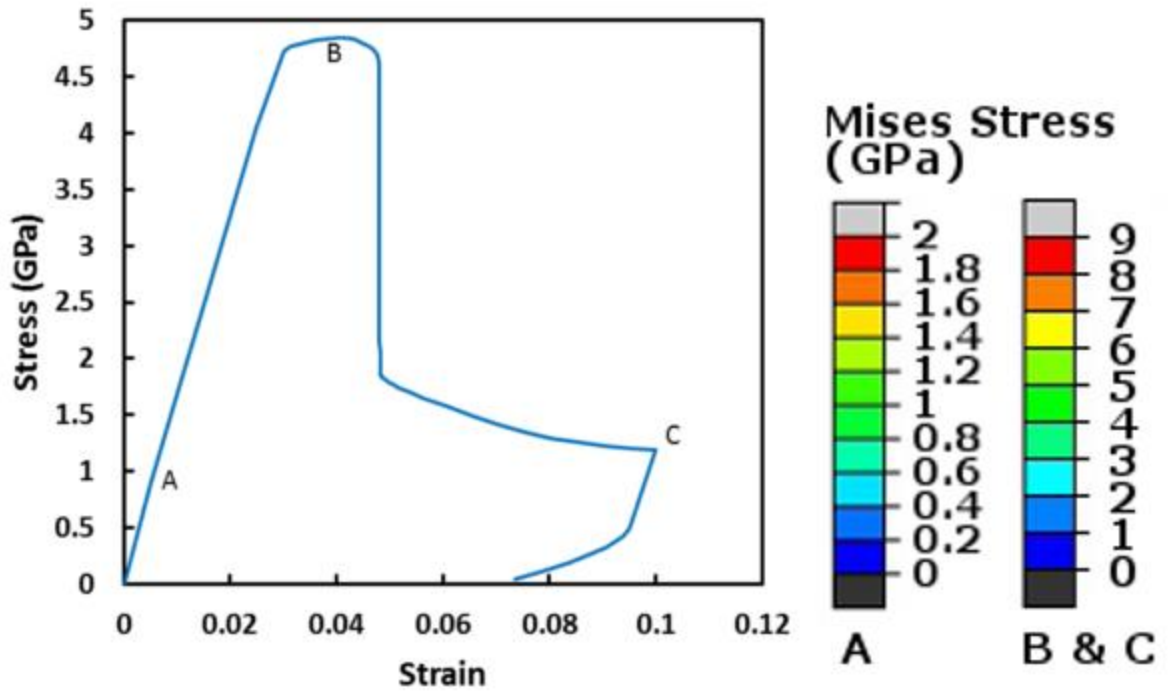
Figure 36: Modeled stress strain response of the flat nanostructure pillar. Von mises stress contours correspond to points indicated on the curve
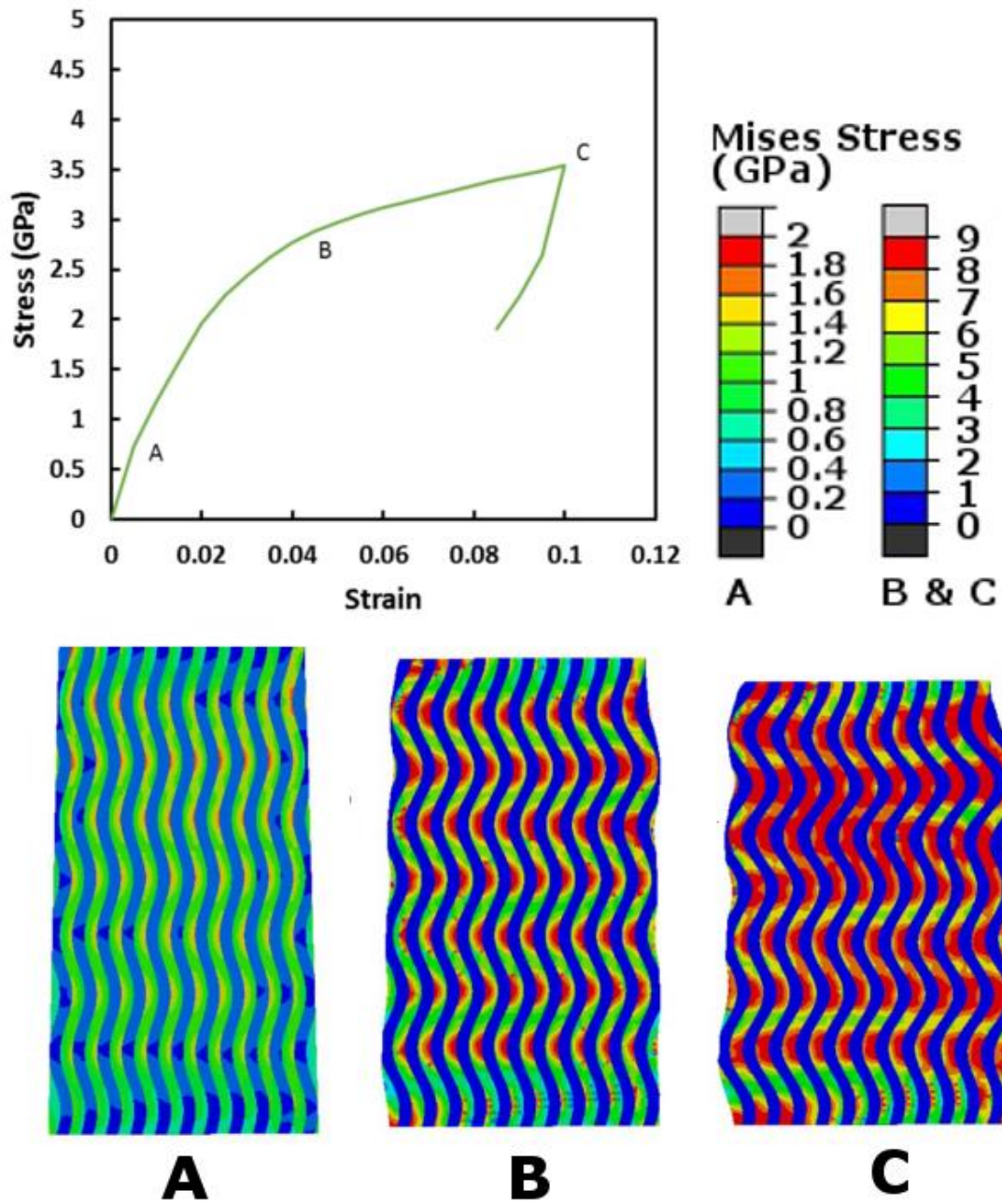
Figure 37: Modeled stress strain response of the cosine nanostructure pillar. Von mises stress contours correspond to points indicated on the curve
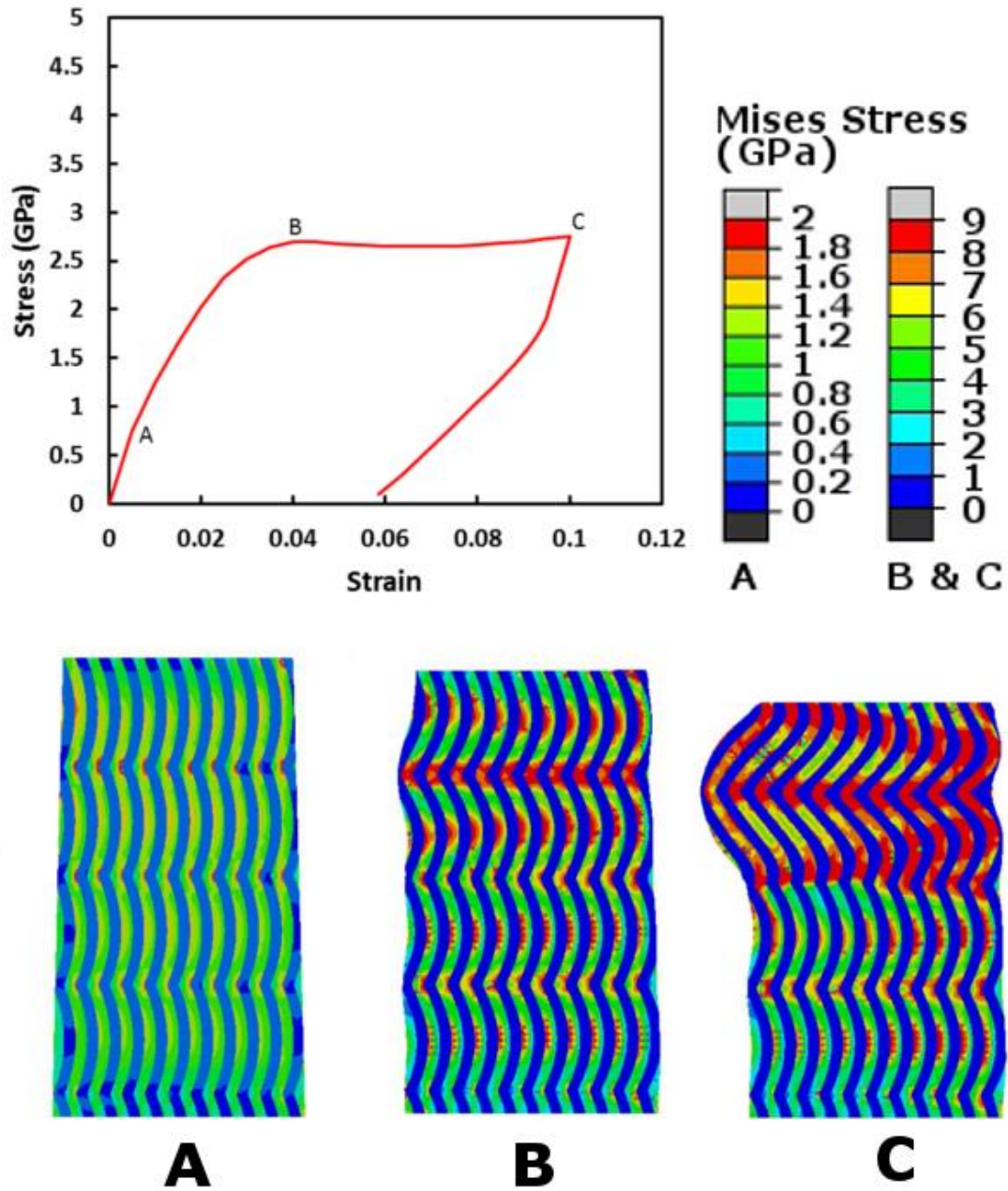
Figure 38: Modeled stress strain response of the arc segment nanostructure pillar. Von mises stress contours correspond to points indicated on the curve (Contour units are TPa)
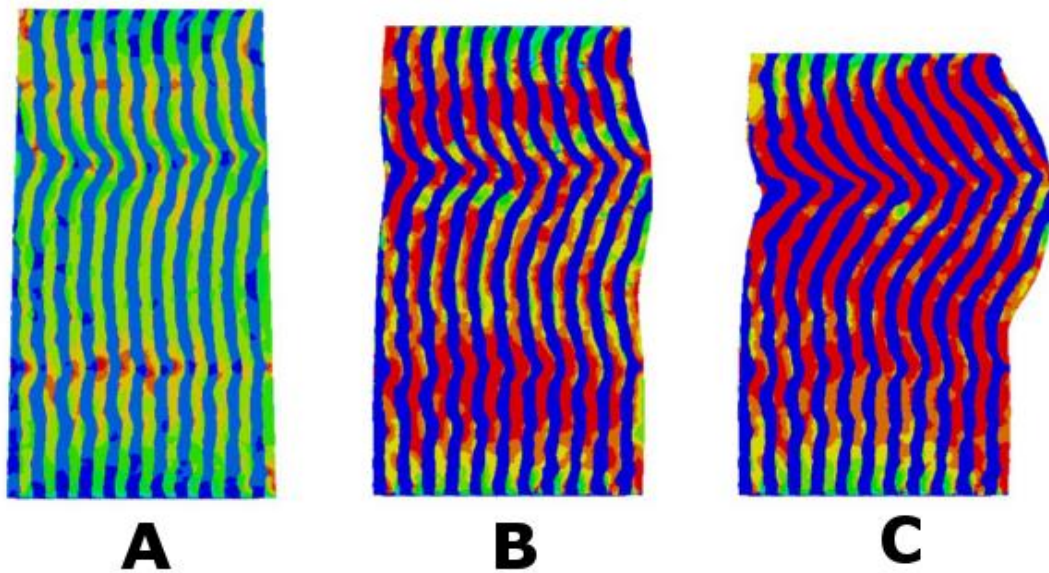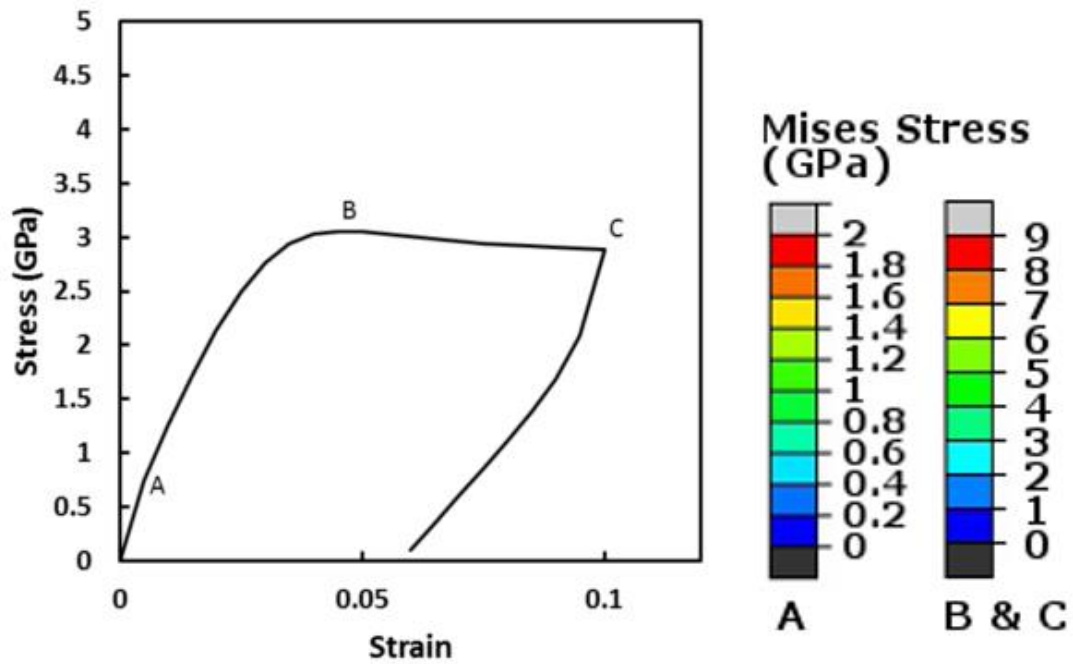
Figure 39: Modeled stress strain response of the FIB determined nanostructure pillar. Von mises stress contours correspond to points indicated on the curve
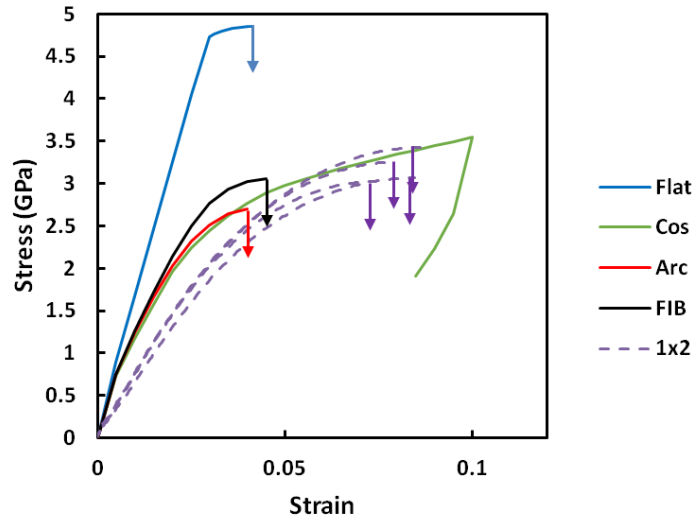
Figure 40: Comparison of modeled responses for all 4 models, showing that the arc structure most closely approximates the FIB determined structure.

In addition to the overall mechanical response quantified by the stress strain behavior, the localization of stresses in the structure are very important as well. This is especially relevant to fracture processes, where the high local stresses can drive flaw propagation even if the farfield stress is low. In order to quantify this localization, the distribution of stresses along the loading axis (S22) was quantified at a strain of 0.005, which is within the elastic regime. For each of the models, a histogram representation of the stresses in the SiC elements was calculated as shown in Figure 41. In order to quantify how well the localization in the FIB structure is reproduced by each of the simplified geometries, the R^2 parameter was used to determine the goodness of fit. The R^2 values for the flat, cosine, and arc segment structures were determined to be -1.67, 0.86, and 0.95, respectively. This indicates that the arc segment model approximates the localization of stresses the most accurately as well.

90
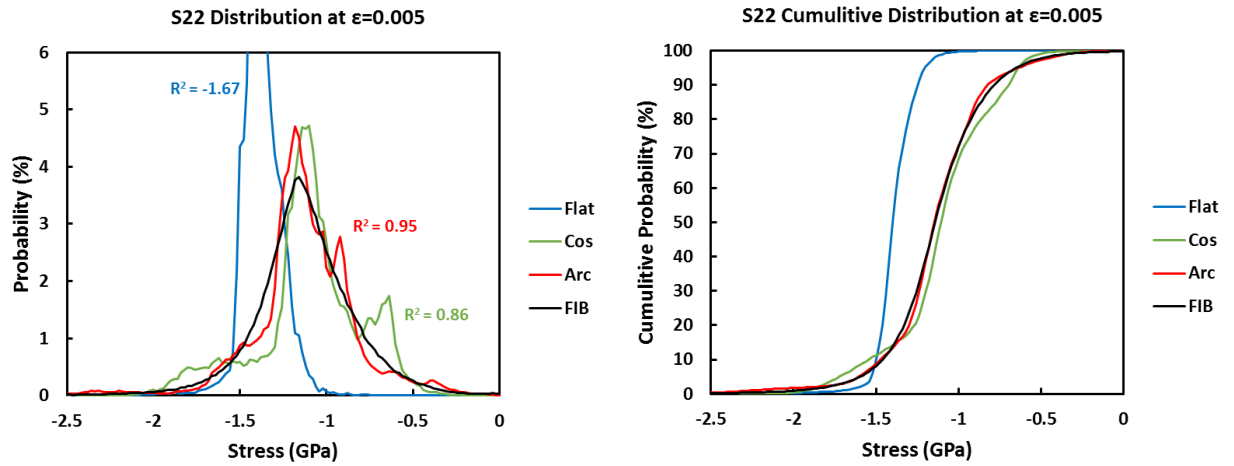
Figure 41: Distribution and cumulative distribution of element stresses in the loading direction for each of the structures at 0.005 strain. The arc segment structure fits the results from the FIB structure the most accurately, indicating it is the most suitable for capturing how the stresses are being localized.

6.4 Summary

This work has provided insight into the role the nanostructure plays in the deformation behavior of Al-SiC nanolaminate composites allowing the following conclusions to be drawn;

- The waviness of the structure makes a significant contribution to the mechanical response of these materials and needs to be accounted for in order to obtain even qualitative agreement with experiment.

- Close agreement between experimental pillar compression and the modeled response of the FIB determined nanostructure was observed in the stress vs plastic strain behavior.

91

- Of the simplified structures used for modeling, the structure consisting of arc segments provided the stress strain response closest to the one obtained using the FIB tomography determined nanostructure

- The arc segment based nanostructure was also able to closely reproduce the distribution of SiC element stresses seen in the FIB tomography determined nanostructure, indicating that the stresses are localized in a similar fashion.

- The two above conclusions indicate that when quantitative modeling results are required, a layer geometry based on arc segments should be utilized.

CHAPTER 7

FRACTURE TOUGHNESS CHARACTERIZATION OF AL-SIC

NANOLAMINATES USING MICRO SCALE CANTILEVER BEAMS

7.1 Introduction

Site specific measurement of the fracture toughness of materials at the microscale, is a powerful tool, providing insight into the behavior of individual phases, size dependent fracture mechanisms, and the behavior of individual interfaces. As mentioned in Chapter 2, the range of methods available for testing at the microscale has grown substantially in recent years to include cantilever beam bending (Matoy et al., 2009, Wurster et al., 2012, Di Maio and Roberts, 2005, Iqbal et al., 2012, Best et al., 2016), double cantilever beam compression (Liu et al., 2013b), clamped beam bending (Jaya and Jayaram, 2014, Jaya et al., 2012), and pillar splitting (Sebastiani et al., 2015). Jaya et al (Jaya et al., 2015) confirmed the accuracy of all these techniques by showing the measured toughness values are within the range reported in literature for bulk [100] Si. However for our particular material system, the cantilever beam approach is the most attractive for a variety of reasons. This is the only methodology which allows the experiments to be performed *ex situ* while still being tolerant of small indenter misalignments, residual stresses, and anisotropy (Jaya et al., 2015). Additionally, the FIB machined notches allow the orientation of the crack propagation to be defined by the geometry, which is essential for testing different crack growth directions. Concerns have been raised regarding the use of FIB machined notches instead of true precracks, however the root radius in our case is

less than 10 nm, which is well below the size where the toughness has been shown to be unaffected by the notch root radius (Best et al., 2016, Iqbal et al., 2012).

Although numerous investigations using this microscale geometry have been focused on linear elastic fracture mechanics (Armstrong et al., 2011, Jaya et al., 2015, Di Maio and Roberts, 2005, Iqbal et al., 2012), the use of an elastic-plastic approach could expand the applicability of this test method to more ductile materials, as commonly done at the bulk scale (ASTM-E1820, 2015, Zhu and Joyce, 2012). A very limited amount of research (Wurster et al., 2012, Ast et al., 2014) has been focused on applying elastic plastic fracture mechanics principles to microscale testing. However there are concerns regarding the accuracy of these previous studies related to the steeply angled crack propagation path, which violates the assumption of mode I crack propagation, and the applicability of their assumed constant value of 2 for the η-factor which is discussed in more detail in the results section.

The J integral was developed as a measure of the energy dissipated during crack growth. This concept is similar to the G parameter, or strain energy release rate, except that G is only applicable to linear elastic solids whereas J is more generally applicable to nonlinear deformation (Zhu and Joyce, 2012). Experimentally, the measurement of this parameter is achieved by accounting for the elastic and plastic contributions to the dissipated energy, determined using the traditional linear elastic fracture toughness for the elastic contribution and the area under the load-plastic displacement curve for the plastic contribution (Zhu and Joyce, 2012).

While previous scratch test results have qualitatively indicated high toughness in these Al-SiC nanolaminates (Singh and Chawla, 2012), this work is aimed at quantitatively determining the fracture toughness of these materials for the first time. This material property is characterized as a function of both layer thickness and crack orientation in order to determine how the changes in deformation mechanisms elucidated in previous studies on nanolaminate films (Lotfian et al., 2014, Misra et al., 2005) manifest themselves in the fracture behavior. The observed changes in the fracture toughness is then discussed in relation to both finite element (FE) simulations of the plastic zone and the observed fracture surfaces.

7.2 Materials and Experimental Procedure

The cantilever beam fabrication process, discussed in the following paragraph, requires a polished 90° edge to be exposed. To achieve this, approximately 5 mm by 5 mm sections of wafer were adhered to a 1 cm x 1 cm x 2 cm copper block with a small amount of wafer overhanging the copper block. This overhanging section was then polished away flush to the block, providing a 90° corner with which to work. Polishing was carried out using SiC paper ranging in grit size from 600 to 1200, then 0.1 um Al_2O_3 suspension, and a final polish with 0.050 um colloidal silica. Care was taken to always keep the polishing direction parallel to the plane of the film in order to minimize the rounding of the corner.

The cantilever beams were fabricated using a dual beam FIB/SEM (Nova 200, FEI) with an ion beam accelerating voltage of 30 kV. First, a high current of 20 nA was used to

mill a large trench in the side of the sample, leaving an approximately 12 μm x 60 μm x 7 μm (depth x length x thickness) freestanding foil. Then using a 7 nA current normal to the top of the sample, this foil was divided into 5 individual cantilevers, approximately 7 μm wide. The shape of the cantilevers was then refined in steps to their nominal 5 μm x 5 μm x 13 μm dimensions using decreasing currents down to 0.1 nA. Line milling at 0.1 nA was then used to cut the notches, which ranged from 500 - 1000 nm due to the different samples and orientations having slightly variable milling rates. Beams were made in batches of 5 for each sample and orientation, leading to a total of 30 beams (6 of which were fractured while testing adjacent beams due to the fairly close spacing). A schematic and a SEM image of a finished beam are provided in Figure 42.
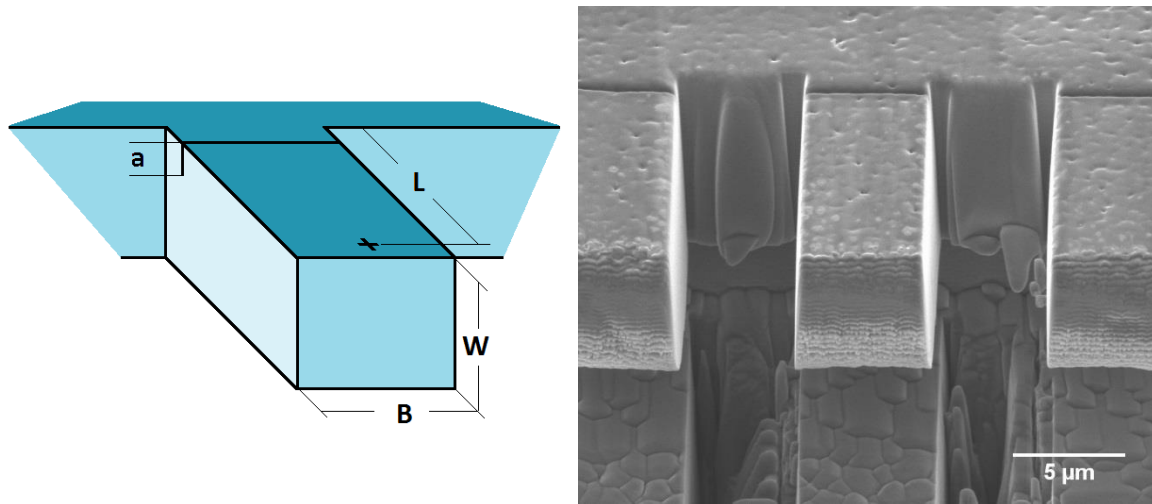
Figure 42. Schematic of the cantilever beam geometry (left) and a SEM image of a beam prior to testing (right)

The bending moment was applied to these cantilevers using a commercial nanoindenter (XPS, Agilent) equipped with a sphero-conical diamond indenter (1 μm diameter tip, 90° included angle). A constant displacement rate of 5 nm/s was applied until the beams fractured, while the load, displacement, and harmonic contact stiffness was recorded. Although the software attempts to maintain a constant displacement rate using feedback,

the nature of the electrostatic actuation of the indenter tip means that the tests are inherently load controlled, which causes fracture events to result in large displacement jumps. Therefore, fracture was defined where the displacement jumps by more than 100 nm between data points, compared to the 1-5 nm between data points that is typical during loading. The thermal drift was allowed to equilibrate until the drift rate was less than 0.05 nm/s before starting each test. The indenter to microscope calibration was performed prior to each test in order to ensure accurate placement of the indenter. The distance between the notch and the indenter was measured using the optical microscope that is built into the indenter.

Post mortem imaging using the SEM (Nova 200, FEI) was used to investigate the fracture surfaces at 5 kV and 1.6 nA. In addition these images allowed for accurate measurement of the sample width, height and notch depth.

The FE models used to determine the plastic zone size were simulated using the commercial software Abaqus (Abaqus, v. 6.12, Dassault Systems Simulia Corp., Providence, R.I.). These simulations are not my own work and were perfomed by my collaborators Yang Lingwei, Valerio Carollo, and Jon Molina Aldareguia from IMDEA Materials. However, their results provide valuable insight into my experimental work and are included for completeness and clarity.

Two dimensional FE models were utilized in this work to determine the effect of layer thickness and orientation on the plastic zone size at the crack tip. A 5x5 µm area was

meshed with a 500 nm notch at the top surface. The mesh far away from the notch was relatively coarse (50, 25, and 10 nm mesh size for 100, 50, and 10 nm layer thickness, respectively) while a 1.5x1.5 μm area around the notch was refined (10, 10, and 5 nm mesh size for 100, 50, and 10 nm layer thickness, respectively). The mesh consisted of 4-node bilinear plane strain quadrilateral elements (CPE4) with perfect interfaces between the constituent phases. A displacement gradient was imposed on the free end of the mesh to approximate a bending moment, such that a stress intensity factor of 0.54 MPa√m was applied for all samples and orientations. The constitutive behavior of each of the phases was based on previous indentation experiments by Yang et al. [25]. The Al phase is considered elastic-perfectly plastic with a modulus of 70 GPa, a Poisson's ratio of 0.34, and yield strengths of 891, 877, and 1477 MPa for the 100, 50 and 10 nm layer thicknesses, respectively.

7.3 Results and Discussion

The load displacement curves are shown for the perpendicular and parallel orientations in Figure 43. Qualitatively, the load displacement curves are approximately linear for the perpendicular case, which indicates there is not a significant amount of stable crack growth or plasticity at the crack tip. The parallel orientation on the other hand, shows increasing nonlinearity in the curves as the layer thickness increases, which indicates an increasing amount of plastic deformation.
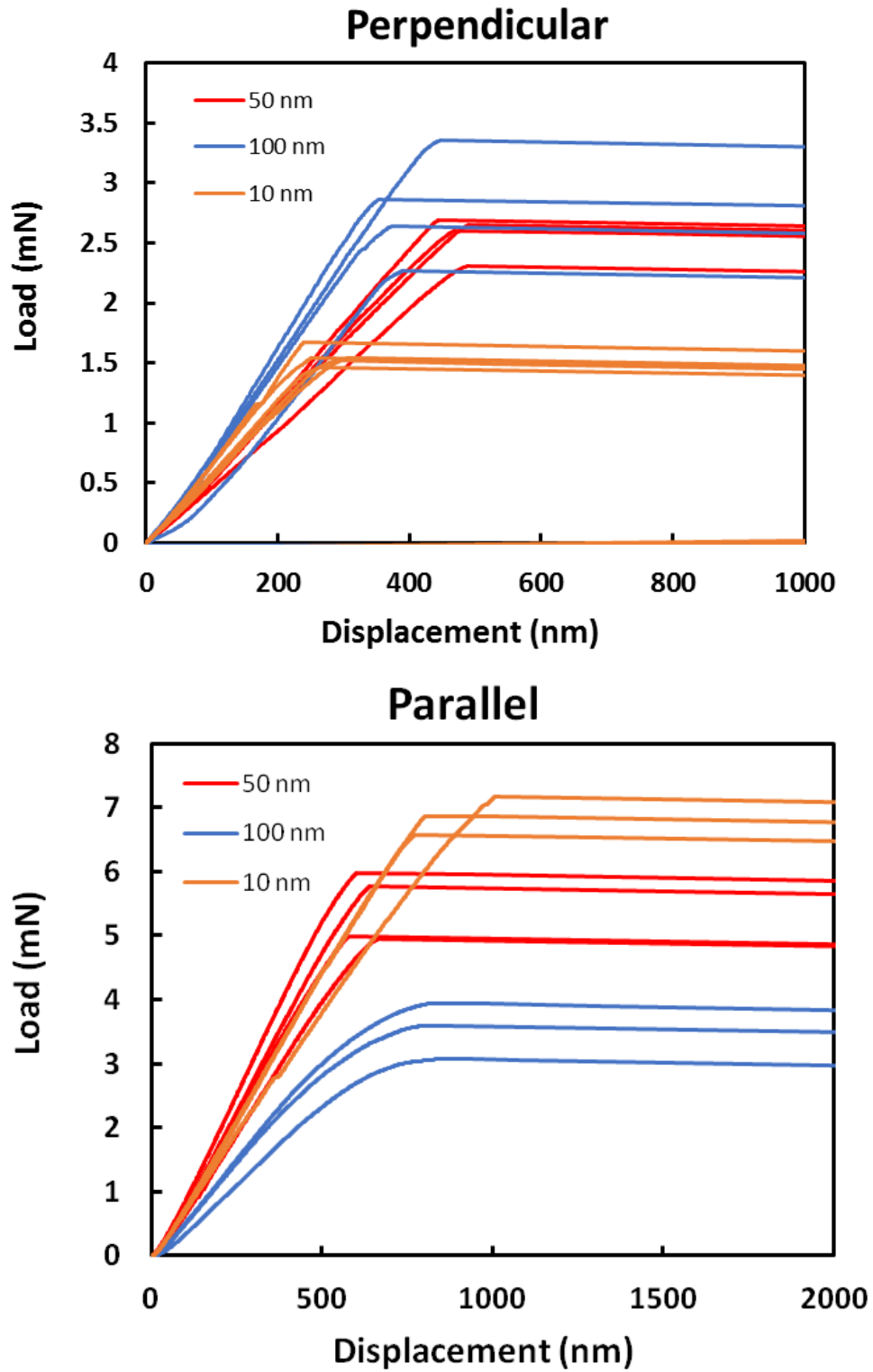
Figure 43. Load-Displacement curves showing little plasticity in the perpendicular orientation (top), and increasing plasticity with layer thickness in the parallel orientation (bottom)

The linear elastic fracture mechanics approach to determining the toughness of materials through cantilever beams has been widely used in the literature (Armstrong et al., 2011, Jaya et al., 2015, Di Maio and Roberts, 2005, Iqbal et al., 2012). The fracture toughness is calculated using the peak load applied to the beam (P_{max}), a dimensionless constant based on the sample geometry (f_{CB}), along with the dimensions of the beam (which are defined in Figure 42), according to the following equations (Jaya et al., 2015, Iqbal et al., 2012):

$$K_{LEFM} = \frac{P_{max}L}{BW^{1.5}} f_{CB}$$

(9)

$$f_{CB} = 1.46 + 24.36\left(\frac{a}{W}\right) - 47.21\left(\frac{a}{W}\right)^2 + 75.18\left(\frac{a}{W}\right)^3$$

(10)

The variation in measured toughness as a function of layer thickness and orientation can be seen in Figure 44. The most widely accepted criterion for determining whether the size of the testing geometry is adequate for obtaining a plane strain condition is B,a $\geq$ 2.5$(K/\sigma_y)^2$. Given the measured toughness and yield strength from previous indentation studies (Lotfian et al., 2014), the B and a dimensions would need to be approximately 1.5 um. As the notch length utilized in these beams is smaller than this, these tests do not satisfy the plane strain condition and must be described as a 'conditional toughness' termed K_Q.
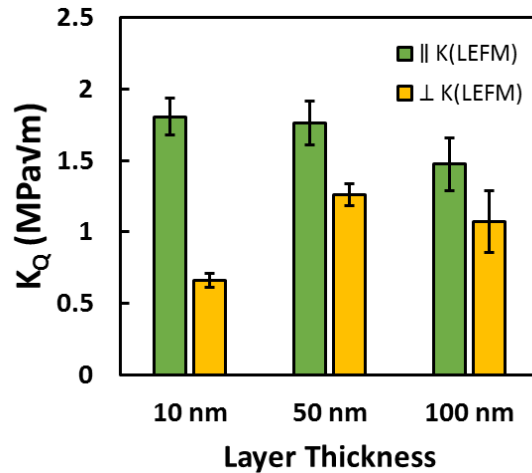
Figure 44. Toughness calculated according to linear elastic fracture mechanics principles. The toughness values are K_Q, or conditional toughness values, as the sample dimensions do not meet the criterion for plane strain fracture toughness. Toughness values for the parallel orientation are approximately constant while the perpendicular orientation shows a large increase from 10 to 50 nm and a slight decrease from 50 to 100 nm.

This shows that it can be challenging to obtain valid plane strain fracture toughness measurements at the microscale even in materials showing fairly brittle behavior because of the small sample dimensions. Because of this, having a less stringent criterion for validity would greatly improve the applicability of this technique by allowing both higher toughness and smaller samples to be tested. Fortunately, the J-integral approach to measuring the fracture toughness has a much more flexible criterion for validity.

The J parameter is a measure of the amount of energy required to propagate a crack, identical to the strain energy release rate, G, in the case of pure elastic brittle materials (Zhu and Joyce, 2012). As such, the elastic-plastic fracture toughness (K_{EPFM}) of the material can be determined from J according to the equation:

101

$$K_{EPFM} = \sqrt{\frac{JE}{(1 - v^2)}}$$

(11)

where E is the Young's modulus and v is the Poisson's ratio. The J parameter consists of

two independent contributions from the elastic energy (J_{el}) and the plastic energy (J_{pl})

dissipated during fracture. The elastic contribution is calculated using the linear elastic

toughness calculated in equation (9), while the plastic contribution is related to the

integral of (or area under) the load-plastic displacement (D_{pl}) curve according to the

following equations (Zhu and Joyce, 2012):

$$J = J_{el} + J_{pl}$$

(12)

$$J_{el} = \frac{K_{LEFM}^2 (1 - v^2)}{E}$$

(13)

$$J_{pl} = \frac{\eta \int (P) dD_{pl}}{B(W - a)}$$

(14)

where η is a geometric factor that depends on the sample configuration.

Unfortunately, the η factor in equation (14) has not been developed for the cantilever

beam geometry and assuming that it is approximately equivalent to η for 3 point bending,

as the studies by Wurster et al. (Wurster et al., 2012) and Ast et al. (Ast et al., 2014) have,

is questionable. Comparing the geometries of the cantilever beam and the 3 point bending

samples as shown in Figure 45, it can be seen that for equivalent samples, S=2L and

$P_{3pt}=2P_{CB}$. Carrying these factors through equations (9) and (14), leads to $f_{CB} \approx 4(f_{3pt})$ and

$\eta_{CB} \approx 2(\eta_{3pt})$. Using both the f_{CB} derived specifically for cantilever beams (equation (10)) and the $f_{CB} \approx 4(f_{3pt})$ approximation, there is only a small 2-5% difference between the calculated fracture toughness values, indicating this use of this approximation is reasonable. As the complimentary approximation of $\eta_{CB} \approx 2(\eta_{3pt})$ should be similarly accurate, the J_{pl} values calculated in the studies by Wurster et al (Wurster et al., 2012) and Ast et al (Ast et al., 2014) are underestimated by a factor of 2. Therefore the f and η parameters used for calculating the plastic toughness in this study are (ASTM-E1820, 2015, Zhang and Lin, 1990):

$$f_{CB} \cong 4 \times f_{3pt} = 12\left(\frac{a}{W}\right)^{0.5} \times \frac{1.99 - \left(\frac{a}{W}\right)\left(1 - \left(\frac{a}{W}\right)\right)\left(2.15 - 3.93\left(\frac{a}{W}\right) + 2.7\left(\frac{a}{W}\right)^2\right)}{2\left(1 + 2\left(\frac{a}{W}\right)\right)\left(1 - \left(\frac{a}{W}\right)\right)^{1.5}}$$

(15)

$$\eta_{CB} \cong 2 \times \eta_{3pt} = 2 \times \left(2 - \frac{\left(1 - \frac{a}{W}\right)\left(1.3096 - 1.6314\frac{a}{W}\right)}{0.9534 + 1.3096\frac{a}{W} - 0.8157\left(\frac{a}{W}\right)^2}\right)$$

(16)
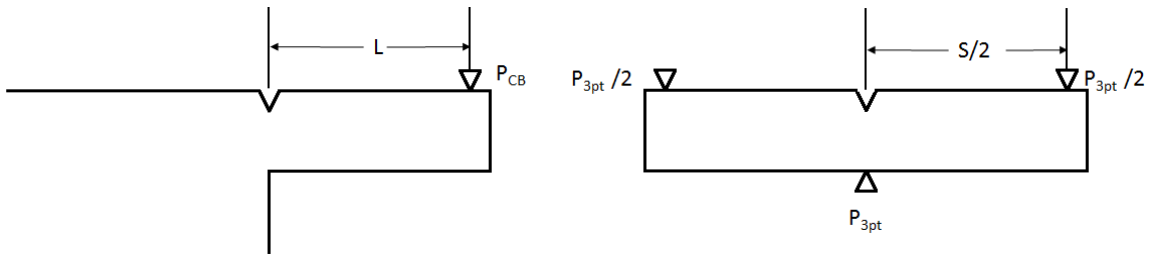
Figure 45. Schematic of equivalent cantilever beam and 3 point bending geometries used to determine the f and η factors. It shows that S=2L and $P_{3pt}=2P_{CB}$

When utilizing the J integral approach, it is also critical to account for any change in crack length due to stable crack growth during the test (ASTM-E1820, 2015, Zhu and

Joyce, 2012). The harmonic contact stiffness vs displacement curves (Figure 46) were used to determine if any crack growth was occurring prior to fracture. The measured harmonic contact stiffness is a convolution of both the beam stiffness and the contact stiffness between the indenter and the surface, behaving as two springs in series. Since the contact stiffness increases sharply with load and the beam stiffness is constant, the surface contact contribution decreases the measured stiffness at low displacements but quickly becomes much greater than the beam stiffness and becomes negligible. Any stable crack growth should result in a significant decrease in the beam stiffness, which is not observed in any of the curves. This indicates that there is no crack growth and J can be calculated without any additional corrections. Although it was not necessary in this particular study, in situ imaging, periodic unloading curves, or the continuous stiffness measurement could be used to determine the amount of crack growth and thereby provide a corrected measure of J according to the methods outlined in ASTM standard E1820 (ASTM-E1820, 2015).
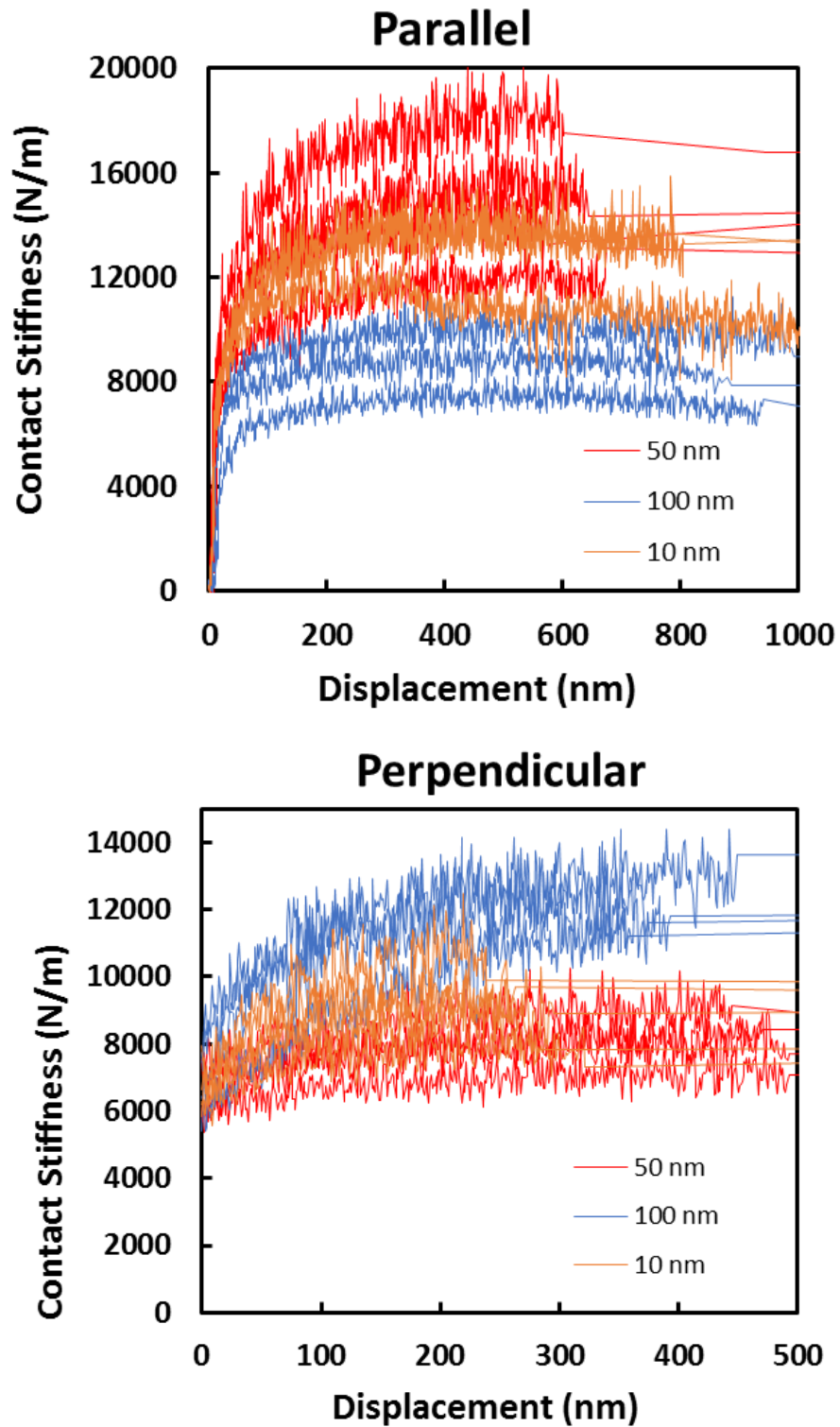
Figure 46. Plots of the contact stiffness vs displacement for each of the beams. The lack of any stiffness drops during loading indicates that there is no stable crack propagation prior to fracture.

Comparing the toughness measurements obtained using the elastic-plastic and linear-elastic analysis methods yields Figure 47. As seen in Figure 47 (a), the elastic-plastic fracture mechanics approach for the perpendicular orientation shows only a small increase in toughness relative to the linear elastic method. This is expected, as the load displacement curves shown in Figure 43 are approximately linear indicating there would be very little contribution from plasticity. In contrast, the parallel orientation shows a much larger increase in toughness due to the plasticity, especially the 100 nm Al - 100 nm SiC sample, as seen in Figure 47 (b). The criterion for validity using this method is B, (W-a) > 25(J/σ_y) (Zhu and Joyce, 2012). All tests in this study pass fulfill this criterion, which indicates these are valid plane strain toughness measurements.
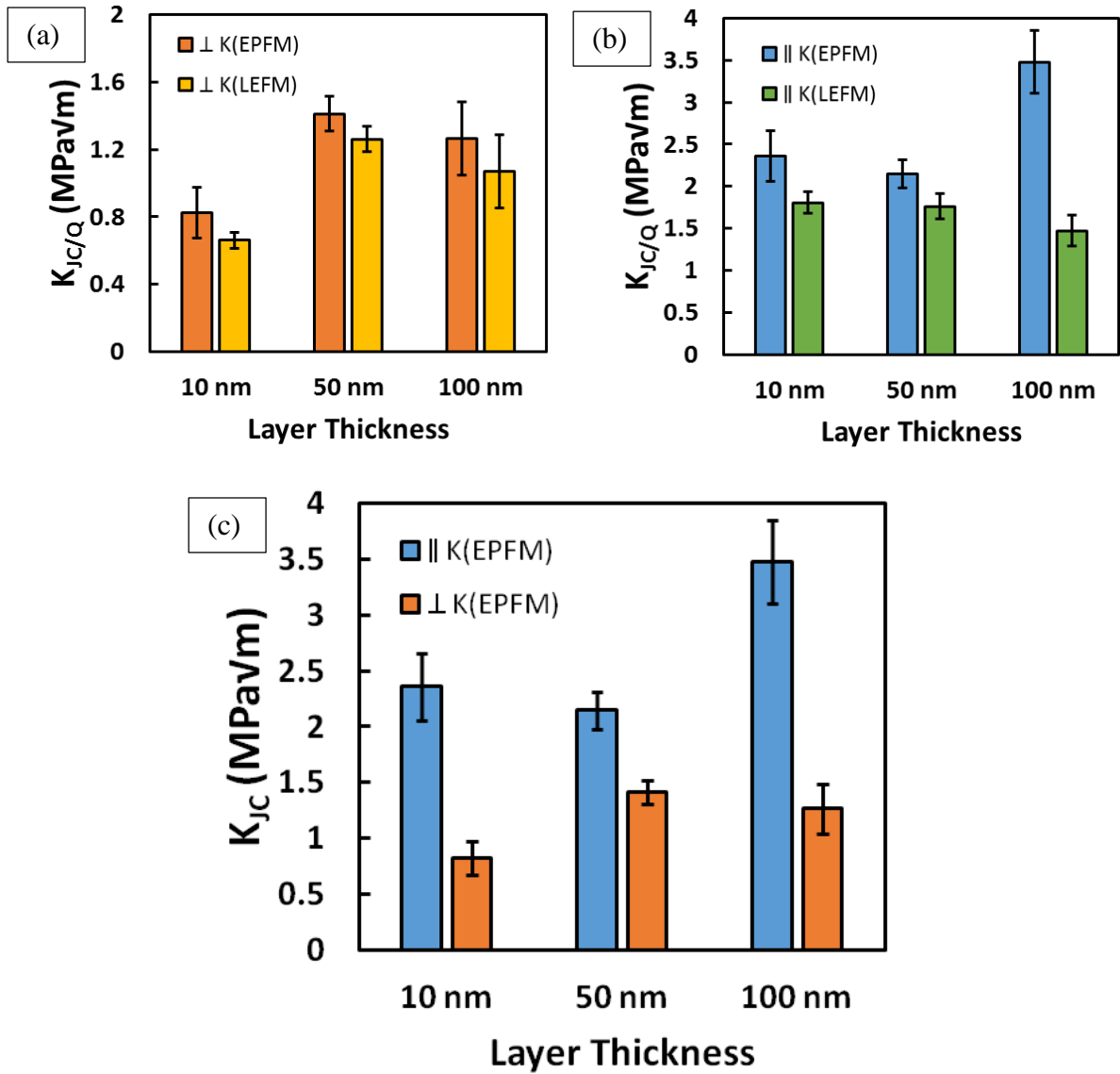
Figure 47. Graphs (a) and (b) show the differences in toughness values calculated using elastic plastic and linear elastic approaches for the perpendicular and parallel orientations, respectively. Graph (c) compares the K_{JC} toughness values measured in the parallel and perpendicular orientations.

Images of the fracture surfaces and FE modeling can provide insight into the mechanisms which lead to the observed trends in the fracture toughness, shown in Figure 47 (c). Figure 48 shows the fracture surfaces of the perpendicular orientation. It can be seen that the 10nm layer thickness does not show any horizontal striations which would be

107

indicative of crack blunting or deflection due to the Al layers. Rather the fracture path appears to be dominated by the vertical columnar boundaries, which are a byproduct of the deposition process and have a higher incidence of porosity. The 50 and 100 nm layer thicknesses show significant horizontal striations, which indicates there is increased plasticity in the Al layers. These observations in conjunction with the significant drop in fracture toughness from 50 to 10 nm suggest that the behavior is being dominated by the by the plasticity in the Al layers. From the fracture surfaces of the parallel oriented beams, shown in Figure 49, it can be seen that the magnitude of the roughness in the 10 nm layer thickness fracture surface is much greater than the layer dimensions. This indicates that the fracture path is not through a single layer or interface but rather it propagates through multiple layers. The fracture path in this case is likely along the columnar boundaries as in the perpendicular case, because these areas are inherently weaker than the rest of the material due to the porosity. For the 50 nm and 100 nm layer thickness, there appears to be discrete islands of Al remaining on the surface. The height of these islands in the 100 nm layer thickness sample is also approximately 100 nm, indicating the crack propagation is predominately along the interface with occasional fractures through the Al layers to reach the adjacent interface.
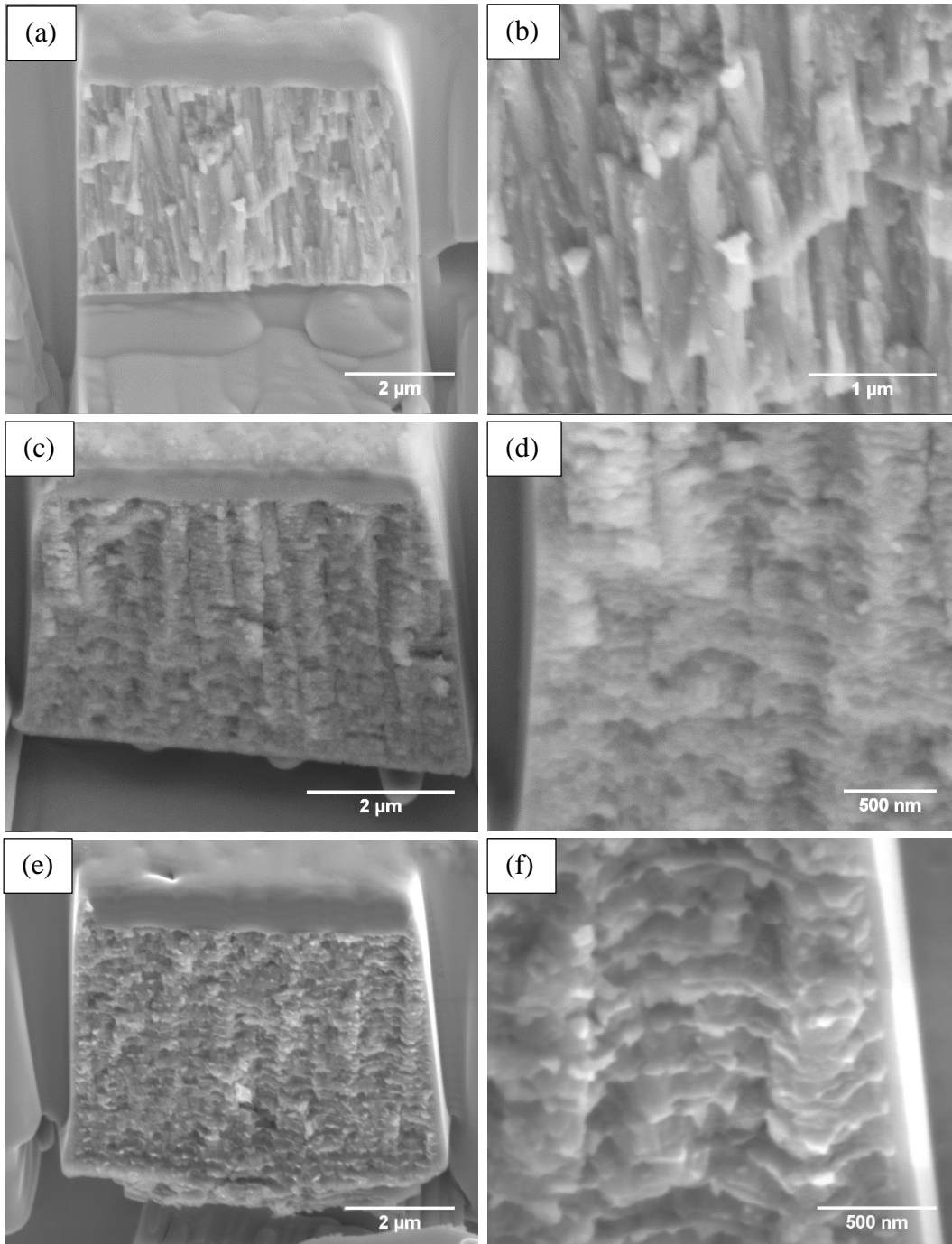
Figure 48. SEM images of representative fracture surfaces of the perpendicular oriented beams. No horizontal striations are observed in the 10 nm layer thickness sample ((a) and (b)) indicating that there is little plasticity in the Al layers. The 50 nm and 100 nm layer thickness samples, ((c) and (d)) and ((e) and (f)), respectively, show very pronounced horizontal striations, indicating significant plasticity is occurring as the crack propagates through the layers.

109
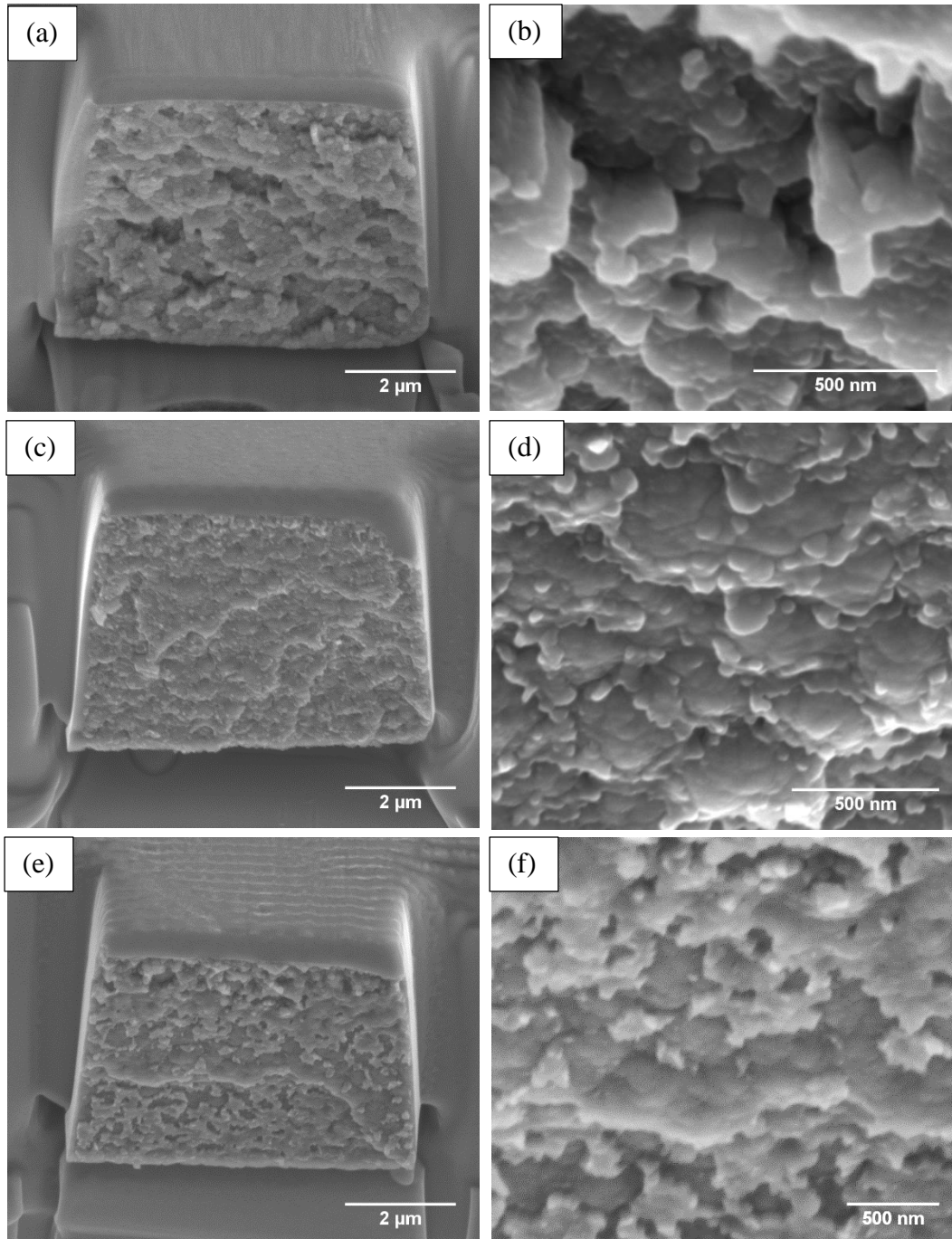
Figure 49. SEM images of representative fracture surfaces of the parallel oriented beams. The 10 nm layer thickness sample ((a) and (b)) shows much greater surface roughness indicating the crack is propagating through multiple layers. The 50 nm and 100 nm layer thickness samples, ((c) and (d)) and ((e) and (f)), respectively, show what appears to be predominantly interfacial failure.

Since the observed fracture surfaces indicated that significant plasticity is occurring in the Al layers, especially at 50 and 100 nm layer thicknesses, the plastic zone size for each layer size and orientation was determined at a constant stress intensity factor using FE models, as shown in Figure 50. The size of the plastic zone should be indicative of the amount of energy dissipated through plasticity, and therefore qualitatively representative of the contribution of the crack tip plasticity to the toughness. The parallel orientation was modeled such that the crack is on the Al-SiC interface because the fracture surfaces appear to be predominantly interfacial (Figure 49). The perpendicular orientation was modeled such that the crack tip ends at an Al layer because it would be the most likely position for a crack to arrest due to the ductility of the Al layer. By comparing the measured fracture toughness to the simulated plastic zone areas as seen in Figure 51, it can be seen that the plastic zone area follows a similar trend as the fracture toughness for the 50 and 100 nm cases, indicating the toughness is dominated by plasticity. The 10 nm layer thickness beams, however do not follow the same trend, with a higher toughness than the plastic zone size would suggest. This higher than expected toughness is likely due to the columnar boundaries. Analogous to the toughening which results from weak interfaces in bulk ceramic-ceramic composites, the weak columnar boundaries promotes an increase in crack deflection and a more tortuous crack path, as seen in the fracture surfaces, resulting in the higher measured toughness.

Parallel

Perpendicular
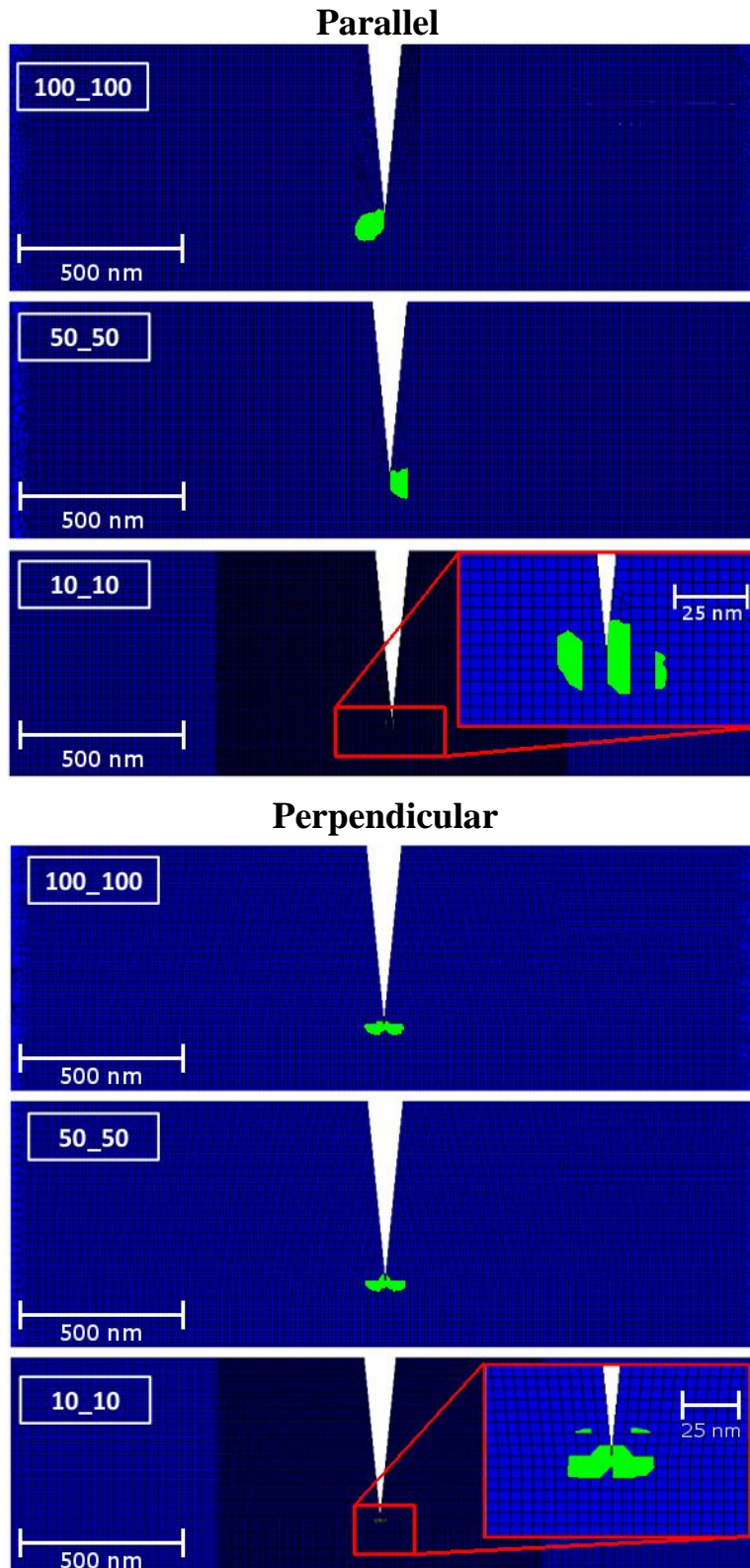
Figure 50. FE models showing the variation in plastic zone size (segmented in green) at a constant applied K (0.54 MPa√m).
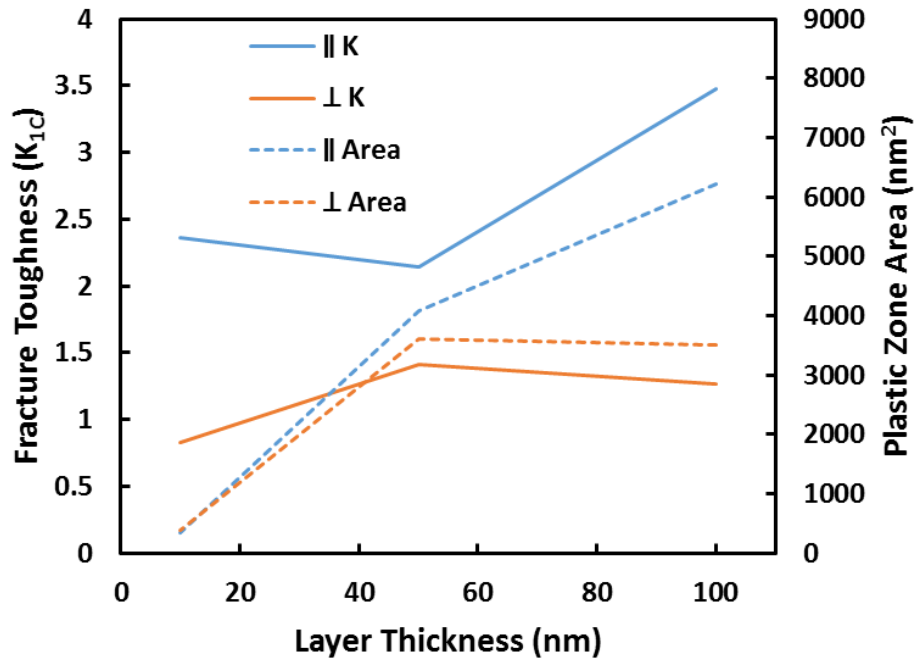
Figure 51. Comparison of the experimental fracture toughness measurements to the plastic zone areas determined using FE modeling.

7.4 Summary

This work has characterized the fracture toughness of Al-SiC nanolaminate composites using microscale cantilever beams. From the results presented in the preceding sections the following conclusions can be drawn:

- The size requirements for the linear elastic fracture mechanics approach to determining the toughness is only applicable to extremely brittle materials or require relatively large sample dimensions, which makes FIB fabrication more time consuming.

- The J integral method for determining the elastic and plastic contributions to the fracture toughness was applied to microscale cantilever beams. This method has

less stringent validity criterion and can be used to characterize smaller samples and tougher materials.

- The plastic contribution to the measured toughness is much greater in the parallel orientation compared to the perpendicular orientation, especially in the 100 nm layer thickness.

- The toughness observed in the 50 and 100 nm layer samples was shown to follow a similar trend as the plastic zone size indicating that the differences in toughness are related to the amount of energy dissipated through plasticity at the crack tip.

- The toughness observed in the 10 nm case is higher than what the plastic zone size would suggest. This increase is thought to be due to the greater crack deflection and more tortuous crack path resulting from the weak columnar grain boundaries.

CHAPTER 8

CONCLUSIONS

8.1 Summary of Research Findings

This work has utilized a wide array of micromechanical testing methods in order to better understand the mechanical properties of these Al-SiC comopsites. The primary outcomes of this research are listed below.

- A novel approach was developed to determine the mechanical properties of these films under shear loading using a microscale double notch shear geometry compressed with a flat punch indenter. To further elucidate the failure mechanisms under shear loading, *in situ* TEM experiments were performed using a double notch geometry cut into the TEM foil. Aluminum layer thicknesses of 50nm and 100nm were used to show the effect of constraint on the deformation. Higher shear strength was observed in the 50 nm Al layers (690±54 MPa) compared to the 100 nm Al layers (423±28.7 MPa). Additionally, failure was dominated by interface fracture in the 50 nm Al layer sample as opposed to failure within the Al layer in the 100 nm Al layer sample.

- Nanolaminate films consisting of 50 nm Al and 50 nm SiC layers were characterized in the perpendicular, inclined and parallel orientations using nanoindentation. The deformation was dominated by buckling of the layers when

the layers were parallel to the indenter and by compression of the ductile Al layers

when the layers were perpendicular to the indenter, while indentation in inclined

orientations showed an intermediate behavior. Finite element modeling (FEM) of

indentation deformation using wavy layers showed much more compliant

behavior and prominent layer buckling than the idealized flat structure,

highlighting the large effect these microstructural details can have on the

deformation behavior.

- Micropillar compression was used to characterize the mechanical behavior of

  50nm Al -50 nm SiC multilayers in different orientations including loading at 0°,

  45° and 90° with respect to the direction of the layers. The 0° orientation showed

  the highest strength while the 45° orientation showed the lowest strength. Each

  orientation showed unique deformation behavior, with buckling dominating the 0°

  and 45° orientations and fracture of the SiC layers dominating the 90°. Effects of

  pillar size and aspect ratio were also studied. Higher compressive strengths were

  observed in smaller pillars for all orientations. This effect was shown to be due to

  a lower probability of flaws using Weibull statistics. Additionally, changes in the

  aspect ratio were shown to have no significant effect on the behavior except an

  increase in the strain to failure in the 0° orientation. Finite element analysis (FEA)

  was used to simulate and understand the effect of these parameters on the

  deformation behavior.

- Although a significant amount of modeling effort has been focused on materials with an idealized flat nanostructure, experimentally these materials exhibit complex undulating layer geometries. FIB tomography was used to characterize this nanostructure in 3D while fininte element modeling was used to determine the effect that this complex structure has on the mechanical behavior of these materials. A sufficiently large volume was characterized such that a 1 x 2 μm micropillar could be generated from the dataset and compared directly to experimental results. The mechanical response from this nanostructure was then compared to pillar models using simplified structures with perfectly flat layers, layers with sinusoidal waviness, and layers with arc segment waviness. The arc segment based layer geometry showed the best agreement with the experimentally determined structure, indicating it would be the most appropriate geometry for future modeling efforts.

- The fracture toughness of these Al-SiC nanolaminates was characterized as a function of both layer thickness (at constant volume ratio) and orientation using microscale cantilever beams. Both linear elastic and elastic plastic methodologies were used to calculate this toughness. The parallel orientation showed overall much higher toughness than the perpendicular orientation especially in the 100 nm Al layer thickness case, where there was significant nonlinearity in the load displacement curves. Fracture surfaces in this orientation indicate interfacial failure in the 50 and 100 nm layer thicknesses and fracture through multiple layers in the 10 nm case. The perpendicular orientation shows very low toughness

117

in the 10 nm layer thickness case where there is little evidence of plasticity in the fracture surfaces. 50 and 100 nm layers show significant horizontal striations which are indicative of plasticity and crack blunting as the crack propagates through the layers. For the 50 and 100 nm layers, the toughness was shown to scale closely with plastic zone size determined using FE simulations.

8.2 Future Work

Although the work presented in the preceding chapters has resulted in a significant advance in our understanding of these intriguing class of composites, there is potential for future work especially in the area of experimenting with alternative material combinations and processing approaches. The Al-SiC combination is a good choice as a nanolaminate model system due to the vast amount of literature available on bulk Al-SiC composites as well as the behavior of Al thin films. However, the toolkit of characterization techniques that have been developed through this work can be employed to test other systems with more potential for practical applications.

Through this study on Al-SiC we saw that two of the biggest factors determining the behavior of these materials was the strength of the interface and the ductility of the metallic phase. To get a better fundamental understanding of the behavior, it would be interesting to investigate the effect of these properties through the use of alloying. Gallium solute added to aluminum preferentially segregates to interfaces and drastically reduces the interface strength (Schmidt et al., 2002, Rajagopalan et al., 2014, Kobayashi

et al., 2006). Although this is a small concern regarding FIB milling as discussed in Chapter 2, it can be used to our advantage to study the effect of interfacial strength in otherwise similar nanolaminates. Using Al-Ga alloys of known compositions as the metallic layers could allow the mechanical properties to be determined as a function of interface strength. Additionally, solid solution strengthening of the Al layers in otherwise identical nanolaminates could help determine if the deformation mechanisms changes as a function of layer thickness (Misra et al., 2005), also discussed in Chapter 2, are affected by changes in the Peierls stress. Besides varying the alloy composition to investigate the fundamental science, new constituent phases could be employed to optimize a whole array of properties. These could include material combinations that are non-reactive at high temperatures or form stronger interfaces, ceramics that are less brittle, or metals that have higher yield strengths or creep resistance.

The current limitations of the processing approaches available is one of the biggest challenges to expanding the practical applications of these materials. Physical vapor deposition will never be a reasonable avenue for creating bulk structural components with these materials and even for coating applications, as the thickness increases above a few microns, layer waviness, porosity, and columnar boundaries become more and more prevalent.   Accumulative roll bonding has been used previously to develop metal-metal nanolaminates in the bulk (Carpenter et al., 2012, Han et al., 2014, Shingu et al., 2001), although this approach is not applicable to metal ceramic systems as the ceramic phase is too brittle. However, the marriage of hard and ductile materials in metal-ceramic combinations could be closely approximated by metal-intermetallic combinations. It

seems feasible that the use of accumulative roll bonding, to form the nanolaminate structure, combined with an appropriate thermal treatment, to develop intermetallic compounds at the interfaces, could yield a metal-intermetallic nanolaminate structure at the bulk scale. For coating applications, different deposition approaches could be attempted in order to reduce the amount of waviness and porosity that occurs currently. Techniques such as atomic layer deposition or liquid phase deposition or some other technique could potentially improve the quality of the layered structure.

REFERENCES

(Abadias et al., 2007) Abadias, G., Michel, A., Tromas, C., Jaouen, C., and Dub, S. (2007). Stress, interfacial effects and mechanical properties of nanoscale multilayered coatings. *Surface and Coatings Technology*, 202(4-7):844 – 853. 2007 34th International Conference and Metallurgical Coatings and Thin Films (ICMCTF 2007).

(Agarwal and Broutman, 1990) Agarwal, B. and Broutman, L. (1990). *Analysis and performance of fiber composites*. SPE monographs. Wiley.

(Anstis et al., 1981) Anstis, G., Chantikul, P., Lawn, B. R., and Marshall, D. (1981). A critical evaluation of indentation techniques for measuring fracture toughness: I, direct crack measurements. *Journal of the American Ceramic Society*, 64(9):533–538.

(Armstrong et al., 2011) Armstrong, D., Wilkinson, A., and Roberts, S. (2011). Micro-mechanical measurements of fracture toughness of bismuth embrittled copper grain boundaries. *Philosophical Magazine Letters*, 91(6):394–400.

(Ast et al., 2014) Ast, J., Przybilla, T., Maier, V., Durst, K., and Göken, M. (2014). Microcantilever bending experiments in nial–evaluation, size effects, and crack tip plasticity. *Journal of Materials Research*, 29(18):2129–2140.

(ASTM-E1820, 2015) ASTM-E1820 (2015). Standard test method for measurement of fracture toughness. astm international, west conshohocken, pa.

(Barshilia et al., 2005) Barshilia, H. C., Prakash, M. S., Jain, A., and Rajam, K. (2005). Structure, hardness and thermal stability of tialn and nanolayered tialn/crn multilayer films. *Vacuum*, 77(2):169 – 179.

(Bei et al., 2007) Bei, H., Shim, S., Miller, M. K., Pharr, G. M., and George, E. P. (2007). Effects of focused ion beam milling on the nanomechanical behavior of a molybdenum-alloy single crystal. *Applied Physics Letters*, 91(11):111915.

(Best et al., 2016)   Best, J. P., Zechner, J., Shorubalko, I., Obona, J. V., Wehrs, J., Morstein, M., and Michler, J. (2016). A comparison of three different notching ions for small-scale fracture toughness measurement. *Scripta Materialia*, 112:71 – 74.

(Bhattacharyya et al., 2011)   Bhattacharyya, D., Mara, N., Dickerson, P., Hoagland, R., and Misra, A. (2011). Compressive flow behavior of al–tin multilayers at nanometer scale layer thickness. *Acta Materialia*, 59(10):3804–3816.

(Carpenter et al., 2012)   Carpenter, J., Vogel, S., LeDonne, J., Hammon, D., Beyerlein, I., and Mara, N. (2012). Bulk texture evolution of cu-nb nanolamellar composites during accumulative roll bonding. *Acta Materialia*, 60(4):1576 – 1586.

(Casellas et al., 2007) Casellas, D., Caro, J., Molas, S., Prado, J. M., and Valls, I. (2007). Fracture toughness of carbides in tool steels evaluated by nanoindentation. *Acta Materialia*, 55(13):4277 – 4286.

(Chawla et al., 2012)   Chawla, N., Liaw, P., Lara-Curzio, E., Ferber, M., and Lowden, R. (2012). Effect of fiber fabric orientation on the flexural monotonic and fatigue behavior of 2d woven ceramic matrix composites. *Materials Science and Engineering: A*, 557(0):77 – 83. A Celebration of Prof. K.K. Chawla's Distinguished Contributions: Fibers, Foams, and Composites.

(Chawla et al., 2006)   Chawla, N., Sidhu, R., and Ganesh, V. (2006). Three-dimensional visualization and microstructure-based modeling of deformation in particle-reinforced composites. *Acta Materialia*, 54(6):1541 – 1548.

(Chawla et al., 2008)   Chawla, N., Singh, D., Shen, Y.-L., Tang, G., and Chawla, K. (2008). Indentation mechanics and fracture behavior of metal/ceramic nanolaminate composites. *Journal of Materials Science*, 43:4383–4390.

(Chen et al., 2010)   Chen, C., Pei, Y., and Hosson, J. D. (2010). Effects of size on the mechanical response of metallic glasses investigated through in situ tem bending and compression experiments. *Acta Materialia*, 58(1):189–200.

(Chen et al., 2012)   Chen, Y., Liu, Y., Sun, C., Yu, K., Song, M., Wang, H., and Zhang, X. (2012). Microstructure and strengthening mechanisms in cu/fe multilayers. *Acta Materialia*, 60(18):6312–6321.

(Chu and Barnett, 1995)   Chu, X. and Barnett, S. A. (1995). Model of superlattice yield stress and hardness enhancements. *Journal of Applied Physics*, 77(9):4403–4411.

(Danzer, 2006)   Danzer, R. (2006). Some notes on the correlation between fracture and defect statistics: Are weibull statistics valid for very small specimens? *Journal of the European Ceramic Society*, 26(15):3043 – 3049.

(Danzer et al., 2007)   Danzer, R., Supancic, P., Pascual, J., and Lube, T. (2007). Fracture statistics of ceramics: Weibull statistics and deviations from weibull statistics. *Engineering Fracture Mechanics*, 74(18):2919 – 2932. Reliability - Statistical Methods in Fracture and Fatigue.

(Daughton et al., 1994)   Daughton, J., Brown, J., Chen, E., Beech, R., Pohm, A., and Kude, W. (1994). Magnetic field sensors using gmr multilayer. *Magnetics, IEEE Transactions on*, 30(6):4608–4610.

(Delobbe et al., 2014) Delobbe, A., Salord, O., Hrncir, T., David, A., Sudraud, P., and Lopour, F. (2014). High speed tem sample preparation by xe fib. *Microsc. Microanal*, 20:3.

(Deng et al., 2005)   Deng, X., Chawla, N., Chawla, K. K., Koopman, M., and Chu, J. P. (2005). Mechanical behavior of multilayered nanoscale metal-ceramic composites. *Advanced Engineering Materials*, 7(12):1099–1108.

(Di Maio and Roberts, 2005) Di Maio, D. and Roberts, S. (2005). Measuring fracture toughness of coatings using focused-ion-beam-machined microbeams. *Journal of materials research*, 20(02):299–302.

(Ding et al., 2012)   Ding, R., Gong, J., Wilkinson, A. J., and Jones, I. P. (2012). Transmission electron microscopy of deformed ti-6al-4v micro-cantilevers. *Philosophical Magazine*, 92(25-27):3290–3314.

(Ding et al., 2014)   Ding, R., Gong, J., Wilkinson, A. J., and Jones, I. P. (2014). c + a dislocations in deformed ti-6al-4v micro-cantilevers. *Acta Materialia*, 76:127 − 134.

(El-Awady et al., 2009)   El-Awady, J. A., Woodward, C., Dimiduk, D. M., and Ghoniem, N. M. (2009). Effects of focused ion beam induced damage on the plasticity of micropillars. *Phys. Rev. B*, 80:104104.

(Farhat et al., 1996)   Farhat, Z., Ding, Y., Northwood, D., and Alpas, A. (1996). Effect of grain size on friction and wear of nanocrystalline aluminum. *Materials Science and Engineering: A*, 206(2):302 − 313.

(Freyman and Chung, 2008) Freyman, C. A. and Chung, Y.-W. (2008). Synthesis and characterization of hardness-enhanced multilayer oxide films for high-temperature applications. *Surface and Coatings Technology*, 202(19):4702 − 4708.

(Gong and Wilkinson, 2009) Gong, J. and Wilkinson, A. J. (2009). Anisotropy in the plastic flow properties of single-crystal titanium determined from micro-cantilever beams. *Acta Materialia*, 57(19):5693 − 5705.

(Gonzalez and LLorca, 2005) Gonzalez, C. and LLorca, J. (2005). Stiffness of a curved beam subjected to axial load and large displacements. *International Journal of Solids and Structures*, 42:1537 − 1545.

(Greer and Hosson, 2011)   Greer, J. R. and Hosson, J. T. D. (2011). Plasticity in small-sized metallic systems: Intrinsic versus extrinsic size effect. *Progress in Materials Science*, 56(6):654 − 724. Festschrift Vaclav Vitek.

(Greer et al., 2005)   Greer, J. R., Oliver, W. C., and Nix, W. D. (2005). Size dependence of mechanical properties of gold at the micron scale in the absence of strain gradients. *Acta Materialia*, 53(6):1821–1830.

124

(Greer et al., 2008)   Greer, J. R., Weinberger, C. R., and Cai, W. (2008). Comparing the strength of f.c.c. and b.c.c. sub-micrometer pillars: Compression experiments and dislocation dynamics simulations. *Materials Science and Engineering: A*, 493(1-2):21 – 25. Mechanical Behavior of Nanostructured Materials, a Symposium Held in Honor of Carl Koch at the TMS Annual Meeting 2007, Orlando, Florida.

(Guo et al., 2014)   Guo, E.-Y., Xie, H.-X., Singh, S. S., Kirubanandham, A., Jing, T., and Chawla, N. (2014). Mechanical characterization of microconstituents in a cast duplex stainless steel by micropillar compression. *Materials Science and Engineering: A*, 598:98 – 105.

(Han et al., 2014)   Han, W., Cerreta, E., Mara, N., Beyerlein, I., Carpenter, J., Zheng, S., Trujillo, C., Dickerson, P., and Misra, A. (2014). Deformation and failure of shocked bulk cu-nb nanolaminates. *Acta Materialia*, 63(0):150 – 161.

(Helmersson et al., 1987)   Helmersson, U., Todorova, S., Barnett, S. A., Sundgren, J., Markert, L. C., and Greene, J. E. (1987). Growth of single crystal tin/vn strained layer superlattices with extremely high mechanical hardness. *Journal of Applied Physics*, 62(2):481–484.

(Heyer et al., 2014)   Heyer, J.-K., Brinckmann, S., Pfetzing-Micklich, J., and Eggeler, G. (2014). Microshear deformation of gold single crystals. *Acta Materialia*, 62(0):225 – 238.

(Holleck et al., 1990) Holleck, H., Lahres, M., and Woll, P. (1990). Multilayer coatings: influence of fabrication parameters on constitution and properties. *Surface and Coatings Technology*, 41(2):179 – 190.

(Huang et al., 2014)   Huang, J., Xu, S., Yi, H., and Hu, S. (2014). Size effect on the compression breakage strengths of glass particles. *Powder Technology*, 268(0):86 – 94.

(Idrissi et al., 2011)   Idrissi, H., Turner, S., Mitsuhara, M., Wang, B., Hata, S., Coulombier, M., Raskin, J.-P., Pardoen, T., Van Tendeloo, G., and Schryvers, D. (2011). Point defect clusters and dislocations in fib irradiated nanocrystalline aluminum films: an electron tomography and aberration-corrected high-resolution adf-stem study. *Microscopy and Microanalysis*, 17(6):983.

(Iqbal et al., 2012)   Iqbal, F., Ast, J., Goken, M., and Durst, K. (2012). In situ micro-cantilever tests to study fracture properties of nial single crystals. *Acta Materialia*, 60(3):1193 – 1200.

(Jamison and Shen, 2014)   Jamison, R. and Shen, Y.-L. (2014). Indentation behavior of multilayered thin films: Effects of layer undulation. *Thin Solid Films*, 570, Part B:235 – 242. 2013 International Thin Films Conference.

(Jamison and Shen, 2015)   Jamison, R. D. and Shen, Y.-L. (2015). Indentation and overall compression behavior of multilayered thin-film composites: Effect of undulating layer geometry. *Journal of Composite Materials*.

(Jaya and Jayaram, 2014)   Jaya, B. N. and Jayaram, V. (2014). Crack stability in edge-notched clamped beam specimens: modeling and experiments. *International Journal of Fracture*, 188(2):213–228.

(Jaya et al., 2015)   Jaya, B. N., Kirchlechner, C., and Dehm, G. (2015). Can microscale fracture tests provide reliable fracture toughness values? a case study in silicon. *Journal of Materials Research*, 30(05):686–698.

(Jaya et al., 2012)   Jaya, N., Jayaram, V., and Biswas, S. K. (2012). A new method for fracture toughness determination of graded (pt, ni) al bond coats by microbeam bend tests. *Philosophical Magazine*, 92(25-27):3326–3345.

(Jiang and Chawla, 2010)   Jiang, L. and Chawla, N. (2010). Mechanical properties of cu6sn5 intermetallic by micropillar compression testing. *Scripta Materialia*, 63(5):480–483.

(Kedward, 1972)   Kedward, K. T. (1972). On the short beam test method. *Fibre Science and Technology*, 5(2):85–95.

(Kiener et al., 2007)   Kiener, D., Motz, C., Rester, M., Jenko, M., and Dehm, G. (2007). Fib damage of cu and possible consequences for miniaturized mechanical tests. *Materials Science and Engineering: A*, 459(1-2):262 – 272.

(Kim et al., 2009)   Kim, J.-Y., Jang, D., and Greer, J. R. (2009). Insight into the deformation behavior of niobium single crystals under uniaxial compression and tension at the nanoscale. *Scripta Materialia*, 61(3):300 – 303.

(Kobayashi et al., 2006)   Kobayashi, M., Toda, H., Uesugi, K., Ohgaki, T., Kobayashi, T., Takayama, Y., and Ahn, B.-G. (2006). Preferential penetration path of gallium into grain boundary in practical aluminium alloy. *Philosophical Magazine*, 86(28):4351–4366.

(Kupka and Lilleodden, 2012)   Kupka, D. and Lilleodden, E. (2012). Mechanical testing of solid–solid interfaces at the microscale. *Experimental Mechanics*, 52:649–658.

(Lauterbach and Gross, 1998)Lauterbach, B. and Gross, D. (1998). Crack growth in brittle solids under compression1. *Mechanics of Materials*, 29(2):81 – 92.

(Lekstrom et al., 2008)   Lekstrom, M., McLachlan, M. A., Husain, S., McComb, D. W., and Shollock, B. A. (2008). Using the in situ lift-out technique to prepare tem specimens on a single-beam fib instrument. *Journal of Physics: Conference Series*, 126(1):012028.

(Li et al., 2012)   Li, N., Mara, N., Wang, J., Dickerson, P., Huang, J., and Misra, A. (2012). Ex situ and in situ measurements of the shear strength of interfaces in metallic multilayers. *Scripta Materialia*, 67(5):479–482.

(Li et al.,)   Li, N., Wang, J., Misra, A., and Huang, J. Y. Direct observations of confined layer slip in cu/nb multilayers. *Microscopy and Microanalysis*, 18:1155–1162.

(Li et al., 2010)   Li, W., Kabius, B., and Auciello, O. (2010). Science and technology of biocompatible thin films for implantable biomedical devices. In *Engineering in Medicine and Biology Society (EMBC), 2010 Annual International Conference of the IEEE*, pages 6237–6242.

(Li and Bhushan, 2002)   Li, X. and Bhushan, B. (2002). A review of nanoindentation continuous stiffness measurement technique and its applications. *Materials Characterization*, 48(1):11 – 36.

(Liu et al., 2013a)   Liu, M., Huang, J., Fong, Y., Ju, S., Du, X., Pei, H., and Nieh, T. (2013a). Assessing the interfacial strength of an amorphous-crystalline interface. *Acta Materialia*, 61(9):3304 – 3313.

(Liu et al., 2013b)   Liu, S., Wheeler, J. M., Howie, P. R., Zeng, X. T., Michler, J., and Clegg, W. J. (2013b). Measuring the fracture resistance of hard coatings. *Applied Physics Letters*, 102(17):–.

(Llorca et al., 1991)   Llorca, J., Needleman, A., and Suresh, S. (1991). An analysis of the effects of matrix void growth on deformation and ductility in metal-ceramic composites. *Acta Metallurgica et Materialia*, 39(10):2317 – 2335.

(Lloyd and Molina-Aldareguia, 2003)   Lloyd, S. J. and Molina-Aldareguia, J. M. (2003). Multilayered materials: a palette for the materials artist. *Philosophical Transactions of the Royal Society of London A: Mathematical, Physical and Engineering Sciences*, 361(1813):2931–2949.

(Lotfian, 2014)   Lotfian, S. (2014). *High Temperature Mechanical Behavior of Al/SiC Nanoscale Multilayers*. PhD thesis, Universidad Carlos III de Madrid.

(Lotfian et al., 2014)   Lotfian, S., Mayer, C., Chawla, N., Llorca, J., Misra, A., Baldwin, J., and Molina-Aldaregua, J. (2014). Effect of layer thickness on the high temperature mechanical properties of al/sic nanolaminates. *Thin Solid Films*, 571, Part 2(0):260 – 267.

(Lotfian et al., 2012)   Lotfian, S., Molina-Aldareguia, J., Yazzie, K., Llorca, J., and Chawla, N. (2012). High-temperature nanoindentation behavior of al/sic multilayers. *Philosophical Magazine Letters*.

(Lotfian et al., 2013)   Lotfian, S., Rodriguez, M., Yazzie, K., Chawla, N., Llorca, J., and Molina-Aldareguia, J. (2013). High temperature micropillar compression of al/sic nanolaminates. *Acta Materialia*, 61(12):4439 – 4451.

(Mara et al., 2008)   Mara, N. A., Bhattacharyya, D., Dickerson, P., Hoagland, R. G., and Misra, A. (2008). Deformability of ultrahigh strength 5nm cu-nb nanolayered composites. *Applied Physics Letters*, 92(23):1–3.

(Martinez et al., 2003)Martinez, E., Romero, J., Lousa, A., and Esteve, J. (2003). Wear behavior of nanometric crn/cr multilayers. *Surface and Coatings Technology*, 164:571–577.

(Matoy et al., 2009)   Matoy, K., Schonherr, H., Detzel, T., Schoberl, T., Pippan, R., Motz, C., and Dehm, G. (2009). A comparative micro-cantilever study of the mechanical behavior of silicon based passivation films. *Thin Solid Films*, 518(1):247 – 256.

(Mayer et al., 2015a) Mayer, C., Li, N., Mara, N., and Chawla, N. (2015a). Micromechanical and in situ shear testing of al-sic nanolaminate composites in a transmission electron microscope (tem). *Materials Science and Engineering: A*, 621:229 – 235.

(Mayer et al., 2016a) Mayer, C., Yang, L., Singh, S., Llorca, J., Molina-Aldareguia, J., Shen, Y., and Chawla, N. (2016a). Anisotropy, size, and aspect ratio effects on micropillar compression of al-sic nanolaminate composites. Submitted to Acta Materialia.

(Mayer et al., 2016b) Mayer, C., Yang, L., Singh, S., Xie, H., Shen, Y.-L., Llorca, J., Molina-Aldareguia, J., and Chawla, N. (2016b). Orientation dependence of indentation behavior in al-sic nanolaminate composites. *Materials Letters*, 168:129 – 133.

(Mayer et al., 2015b) Mayer, C. R., Lotfian, S., Molina-Aldareguia, J., and Chawla, N. (2015b). High-temperature micropillar compression creep testing of constituent phases in lead-free solder. *Advanced Engineering Materials*.

(Misra et al., 2005)   Misra, A., Hirth, J., and Hoagland, R. (2005). Length-scale-dependent deformation mechanisms in incoherent metallic multilayered composites. *Acta Materialia*, 53(18):4817 – 4824.

(Misra et al., 2004)   Misra, A., Hirth, J., Hoagland, R., Embury, J., and Kung, H. (2004). Dislocation mechanisms and symmetric slip in rolled nano-scale metallic multilayers. *Acta Materialia*, 52(8):2387 – 2394.

(Moser et al., 2007)   Moser, B., Wasmer, K., Barbieri, L., and Michler, J. (2007). Strength and fracture of si micropillars: A new scanning electron microscopy-based micro-compression test. *Journal of Materials Research*, 22:1004–1011.

(Oliver and Pharr, 2004)   Oliver, W. and Pharr, G. (2004). Measurement of hardness and elastic modulus by instrumented indentation: Advances in understanding and refinements to methodology. *Journal of Materials Research*, 19(01):3–20.

(Pfetzing-Micklich et al., 2011)   Pfetzing-Micklich, J., Brinckmann, S., Dey, S., Otto, F., Hartmaier, A., and Eggeler, G. (2011). Micro-shear deformation of pure copper. *Materialwissenschaft und Werkstofftechnik*, 42(3):219–223.

(Pharr et al., 2009)   Pharr, G., Strader, J., and Oliver, W. (2009). Critical issues in making small-depth mechanical property measurements by nanoindentation with continuous stiffness measurement. *Journal of Materials Research*, 24:653–666.

(Qidwai et al., 2009)   Qidwai, M. S., Lewis, A. C., and Geltmacher, A. B. (2009). Using image-based computational modeling to study microstructure-yield correlations in metals. *Acta Materialia*, 57(14):4233 – 4247.

(Quinn and Quinn, 2010)   Quinn, J. B. and Quinn, G. D. (2010). A practical and systematic review of Weibull statistics for reporting strengths of dental materials. *Dental Materials*, 26, 135-147.

(Rajagopalan et al., 2014)   Rajagopalan, M., Bhatia, M., Tschopp, M., Srolovitz, D., and Solanki, K. (2014). Atomic-scale analysis of liquid-gallium embrittlement of aluminum grain boundaries. *Acta Materialia*, 73:312 – 325.

(Romero et al., 2004)   Romero, J., Esteve, J., and Lousa, A. (2004). Period dependence of hardness and microstructure on nanometric cr/crn multilayers. *Surface and Coatings Technology*, 188-189:338 – 343. Proceedings of the 31st International Conference on Metallurgical Coatings and Thin Films.

(Schlogl et al., 2013)   Schlogl, M., Kirchlechner, C., Paulitsch, J., Keckes, J., and Mayrhofer, P. (2013). Effects of structure and interfaces on fracture toughness of crn/aln multilayer coatings. *Scripta Materialia*, (0).

(Schmidt et al., 2002) Schmidt, S., Sigle, W., Gust, W., and Ruhle, M. (2002). Gallium segregation at grain boundaries in aluminium. *Zeitschrift fuer Metallkunde/Materials Research and Advanced Techniques*, 93(5):428–431. cited By 19.

(Sebastiani et al., 2015) Sebastiani, M., Johanns, K., Herbert, E. G., Carassiti, F., and Pharr, G. (2015). A novel pillar indentation splitting test for measuring fracture toughness of thin ceramic coatings. *Philosophical Magazine*, 95(16-18):1928–1944.

(Shim et al., 2009) Shim, S., Bei, H., Miller, M., Pharr, G., and George, E. (2009). Effects of focused ion beam milling on the compressive behavior of directionally solidified micropillars and the nanoindentation response of an electropolished surface. *Acta Materialia*, 57(2):503 – 510.

(Shingu et al., 2001) Shingu, P., Ishihara, K., Otsuki, A., and Daigo, I. (2001). Nano-scaled multi-layered bulk materials manufactured by repeated pressing and rolling in the cu-fe system. *Materials Science and Engineering: A*, 304-306(0):399 – 402. RQ10, Tenth International Conference on Rapidly Quenched and Metastable Materials.

(Shinn et al., 1992) Shinn, M., Hultman, L., and Barnett, S. (1992). Growth, structure, and microhardness of epitaxial tin/nbn superlattices. *Journal of Materials Research*, 7:901–911.

(Sidhu and Chawla, 2006) Sidhu, R. and Chawla, N. (2006). Three-dimensional (3d) visualization and microstructure-based modeling of deformation in a sn-rich solder. *Scripta Materialia*, 54(9):1627 – 1631.

(Singh and Chawla, 2012) Singh, D. and Chawla, N. (2012). Scratch resistance of al/sic metal/ceramic nanolaminates. *Journal of Materials Research*, 27:278–283.

(Singh et al., 2010a) Singh, D., Chawla, N., and Shen, Y.-L. (2010a). Focused ion beam (fib) tomography of nanoindentation damage in nanoscale metal/ceramic multilayers. *Mater Char*, 61(4):481–488.

(Singh et al., 2010b)   Singh, D., Chawla, N., Tang, G., and Shen, Y.-L. (2010b). Micropillar compression of al/sic nanolaminates. *Acta Materialia*, 58(20):6628–6636.

(Singh et al., 2010c)   Singh, D., Deng, X., Chawla, N., Bai, J., Hubbard, C., Tang, G., and Shen, Y.-L. (2010c). Residual stress characterization of al/sic nanoscale multilayers using x-ray synchrotron radiation. *Thin Solid Films*, 519(2):759 – 765. Special Section: Romanian Conference on Advanced Materials 2009.

(Singh et al., 2014)   Singh, S. S., Schwartzstein, C., Williams, J. J., Xiao, X., Carlo, F. D., and Chawla, N. (2014). 3d microstructural characterization and mechanical properties of constituent particles in al 7075 alloys using x-ray synchrotron tomography and nanoindentation. *Journal of Alloys and Compounds*, 602:163 – 174.

(Singh et al., 2016)   Singh, S. S., Williams, J. J., Stannard, T. J., Xiao, X., Carlo, F. D., and Chawla, N. (2016). Measurement of localized corrosion rates at inclusion particles in aa7075 by in situ three dimensional (3d) x-ray synchrotron tomography. *Corrosion Science*, 104:330 – 335.

(Soler et al., 2014)   Soler, R., Wheeler, J. M., Chang, H.-J., Segurado, J., Michler, J., Llorca, J., and Molina-Aldareguia, J. M. (2014). Understanding size effects on the strength of single crystals through high-temperature micropillar compression. *Acta Materialia*, 81:50 – 57.

(Stearns et al., 1993)   Stearns, D. G., Rosen, R. S., and Vernon, S. P. (1993). Multilayer mirror technology for soft-x-ray projection lithography. *Appl. Opt.*, 32(34):6952–6960.

(Sun et al., 2010)   Sun, P., Chu, J., Lin, T., Shen, Y., and Chawla, N. (2010). Characterization of nanoindentation damage in metal/ceramic multilayered films by transmission electron microscopy (tem). *Materials Science and Engineering: A*, 527(12):2985–2992.

(Tang et al., 2008)   Tang, G., Shen, Y.-L., and Chawla, N. (2008). Plastic deformation during indentation unloading in multilayered materials. *Journal of Applied Physics*, 104(11):116102.

(Tang et al., 2010a)   Tang, G., Shen, Y.-L., Singh, D., and Chawla, N. (2010a). Indentation behavior of metal-ceramic multilayers at the nanoscale: Numerical analysis and experimental verification. *Acta Materialia*, 58(6):2033–2044.

(Tang et al., 2010b)   Tang, G., Shen, Y.-L., Singh, D., and Chawla, N. (2010b). Indentation behavior of metal-ceramic multilayers at the nanoscale: Numerical analysis and experimental verification. *Acta Materialia*, 58(6):2033 – 2044.

(Thompson and Chesnutt, 1979)   Thompson, A. W. and Chesnutt, J. C. (1979). Identification of a fracture mode: the tearing topography surface. *Metallurgical Transactions A*, 10(8):1193–1196.

(Tomus and Ng, 2013)   Tomus, D. and Ng, H. P. (2013). In situ lift-out dedicated techniques using fib-sem system for tem specimen preparation. *Micron*, 44(0):115 – 119.

(Tschopp and McDowell, 2008)   Tschopp, M. and McDowell, D. (2008). Grain boundary dislocation sources in nanocrystalline copper. *Scripta Materialia*, 58(4):299 – 302.

(Uchic and Dimiduk, 2005)   Uchic, M. D. and Dimiduk, D. M. (2005). A methodology to investigate size scale effects in crystalline plasticity using uniaxial compression testing. *Materials Science and Engineering: A*, 400–401(0):268–278.

(Uchic et al., 2009)   Uchic, M. D., Shade, P. A., and Dimiduk, D. M. (2009). Plasticity of micrometer-scale single crystals in compression. *ANNUAL REVIEW OF MATERIALS RESEARCH*, 39:361–386.

(Verma and Jayaram, 2014)   Verma, N. and Jayaram, V. (2014). Role of interface curvature on stress distribution under indentation for zrn/zr multilayer coating. *Thin Solid Films*, 571, Part 2(0):283 – 289. Multilayers 2013.

(Volkert and Lilleodden, 2006)   Volkert, C. A. and Lilleodden, E. T. (2006). Size effects in the deformation of sub-micron au columns. *Philosophical Magazine*, 86(33-35):5567–5579.

(Wang and Misra, 2011)   Wang, J. and Misra, A. (2011). An overview of interface-dominated deformation mechanisms in metallic multilayers. *Current Opinion in Solid State and Materials Science*, 15(1):20 – 28.

(Was and Foecke, 1996)   Was, G. and Foecke, T. (1996). Deformation and fracture in microlaminates. *Thin Solid Films*, 286(1-2):1–31.

(Weber et al., 2016)   Weber, J., Barthel, J., Brandt, F., Klinkenberg, M., Breuer, U., Kruth, M., and Bosbach, D. (2016). Nano-structural features of barite crystals observed by electron microscopy and atom probe tomography. *Chemical Geology*, 424:51 – 59.

(Wiklund et al., 1997) Wiklund, U., Hedenqvist, P., and Hogmark, S. (1997). Multilayer cracking resistance in bending. *Surface and Coatings Technology*, 97(1-3):773 – 778.

(Williams et al., 2002)   Williams, J., Piotrowski, G., Saha, R., and Chawla, N. (2002). Effect of overaging and particle size on tensile deformation and fracture of particle-reinforced aluminum matrix composites. *Metallurgical and Materials Transactions A*, 33(12):3861–3869.

(Wolfe et al., 2002)   Wolfe, D. E., Singh, J., and Narasimhan, K. (2002). Synthesis of titanium carbide/chromium carbide multilayers by the co-evaporation of multiple ingots by electron beam physical vapor deposition. *Surface and Coatings Technology*, 160(2-3):206 – 218.

(Wong et al., 2006)   Wong, T., Wong, R. H., Chau, K., and Tang, C. (2006). Microcrack statistics, weibull distribution and micromechanical modeling of compressive failure in rock. *Mechanics of Materials*, 38(7):664 – 681.

(Wu et al., 2006)   Wu, Z., Zhang, G., Wang, M., Fan, X., Yan, P., and Xu, T. (2006). Structure and mechanical properties of al/aln multilayer with different aln layer thickness. *Applied Surface Science*, 253(5):2733 – 2738.

(Wurster et al., 2012) Wurster, S., Motz, C., and Pippan, R. (2012). Characterization of the fracture toughness of micro-sized tungsten single crystal notched specimens. *Philosophical Magazine*, 92(14):1803–1825.

(Yang et al., 2014)   Yang, H., Zhang, P., Pei, Y., Zhang, Z., and Hosson, J. T. D. (2014). In situ bending of layered compounds: The role of anisotropy in ti2alc microcantilevers. *Scripta Materialia*, 89:21 – 24.

(Yang et al., 2015)   Yang, L., Mayer, C., Chawla, N., LLorca, J., and Molina-Aldareguía, J. M. (2015). Deformation mechanisms of ultra-thin al layers in al/sic nanolaminates as a function of thickness and temperature. submitted article.

(Yang and Molina-Aldaregua, 2016) Yang, L. and Molina-Aldaregua, J. (2016). Tem study of ga distribution in al-sic nanolaminates. Unpublished work.

(Yashar et al., 1999)   Yashar, P. C., Barnett, S. A., Hultman, L., and Sproul, W. D. (1999). Deposition and mechanical properties of polycrystalline y2o3/zro2 superlattices. *Journal of Materials Research*, 14:3614–3622.

(Zhang and Lin, 1990)   Zhang, D. and Lin, J. (1990). A general formula for three-point bend specimen j-integral calculation. *Engineering Fracture Mechanics*, 36(5):789 – 793.

(Zhang et al., 2013a)   Zhang, G., Fan, T., Wang, T., and Chen, H. (2013a). Microstructure, mechanical and tribological behavior of monx/sinx multilayer coatings prepared by magnetron sputtering. *Applied Surface Science*, 274(0):231 – 236.

(Zhang et al., 2014)   Zhang, J., Liang, X., Zhang, P., Wu, K., Liu, G., and Sun, J. (2014). Emergence of external size effects in the bulk-scale polycrystal to small-scale single-crystal transition: A maximum in the strength and strain-rate sensitivity of multicrystalline cu micropillars. *Acta Materialia*, 66:302 – 316.

(Zhang et al., 2013b)   Zhang, J., Liu, G., and Sun, J. (2013b). Comparisons between homogeneous boundaries and heterophase interfaces in plastic deformation: Nanostructured cu micropillars vs. nanolayered cu-based micropillars. *Acta Materialia*, 61(18):6868 – 6881.

(Zhu and Joyce, 2012)Zhu, X.-K. and Joyce, J. A. (2012). Review of fracture toughness (g, k, j, ctod, ctoa) testing and standardization. *Engineering Fracture Mechanics*, 85:1–46.

(Zweben et al., 1979) Zweben, C., Smith, W., and Wardle, M. (1979). Test methods for fiber tensile strength, composite flexural modulus, and properties of fabric-reinforced laminates. In *Composite materials: testing and design (fifth conference), ASTM STP*, volume 674, pages 228–262.

APPENDIX A

TENSION-COMPRESSION ASYMMETRY

In Chapter 5, micropillar compression experiments on Al-SiC nanolaminates with individual

layer thicknesses of 50 nm were shown to have a significant size effect, where smaller pillars

showed higher strengths. This effect was attributed to flaw dependent fracture, where smaller

samples will have a lower probability of containing a strength limiting flaw, and therefore higher

apparent strengths. Using Weibull statistics, the increase in strength was shown to be completely

accounted for by the sample volume term in the 2 parameter Weibull equation, providing

evidence for this hypothesis. Another byproduct of flaw dependent fracture is a significant

amount of tension compression asymmetry. This asymmetry arises from the fact that tensile

stresses load pre-existing flaws directly in Mode I, while compressive stresses load flaws

indirectly, either in Mode I through the circumferential tensile stress, or in Mode II through a

resolved shear stress, both of which require higher applied stresses to activate. Therefore, if the

tensile strength measured is significantly lower than the compressive strength, the results would

provide further evidence for flaw dominated fracture.

Microcantilever beams were fabricated and fractured as described in Chapter 7, excluding the

notching step. Using the raw load-displacement data as well as the dimensions of the beam, the

stress and strain are able to be calculated according to the following expressions:

$$\sigma = \frac{3.25PL}{BW^2} \quad , \quad \epsilon = \frac{0.63DW}{L^2}$$

$$(A17)$$

where P is the load and D is the displacement (B,W, and L are defined in Chapter 7). The scaling

coefficients for the stress and strain were determined using the linear elastic finite element model

used in Appendix B. The resultant flexural stress strain curves and 2 parameter Weibull plot are
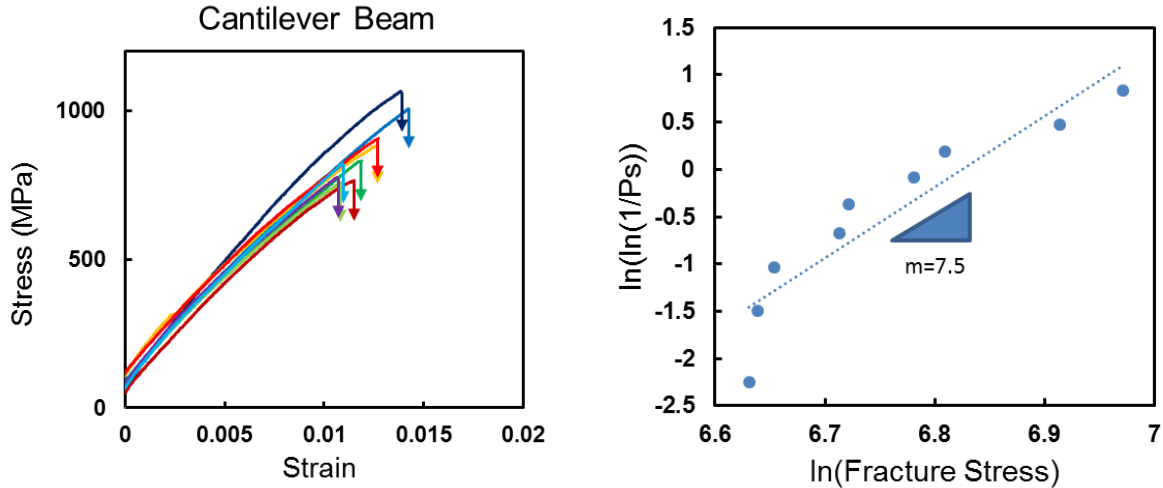
shown in Figure A1.

Figure A1. (Left) Stress strain curves from the cantilever beams without notches. The response is approximately linear and shows a significant amount of scatter in the fracture strengths. (Right) Two parameter Weibull plot showing a Weibull modulus of 7.5

From Figure A1 it can be seen that the stress strain curves display linear deformation and then

brittle fracture over a fairly wide distribution of stresses, yielding a fairly low Weibull modulus,

m, of 7.5. Comparing the flexural strengths with the pillar compression results from Chapter 5,

as shown in Figure A2, we can see that the strength in compression is significantly higher than

the flexural strength. Additionally, the measured flexural strength of 868 MPa is fairly close to

the macroscopic tensile strength determined by Deng et al. [Deng et al., 2005] of 711 MPa.

However, direct comparison of this work to Deng's study should be done with caution as the

volume of material tested and the defect density are expected to vary significantly due to the

differences in testing method and total multilayer thickness.

The volume of material tested using the cantilever beams is also expected to be different than in compression. However, this difference can be accounted for using the concept of an equivalent volume. The equivalent volume for the pillar compression geometry is simply the volume of the pillar because the stress state is approximately uniform throughout the whole sample. As only a small area of the bending geometry is under a significant amount of stress, the equivalent volume in this geometry is quite small and can be calculated according to the expression $V_{eq}=LBW/(m+1)^2$ (Quinn and Quinn, 2010). This expression was developed for the 3 point bending geometry, however, by comparing the two geometries and noting that the span in 3 point bending is equivalent to twice the cantilever length, as done in Chapter 7 for the f and η parameters, it can be adapted to provide a good approximation for the cantilever beam geometry. The equivalent volumes for the 1x2 and 2x4 μm pillars are 1.6 and 12.6 μm^3, respectively, while the equivalent volume for the cantilever beams is 3.5 μm^3. As the flexural strength is still much lower than the 2x4 μm pillars, this shows that there is a significant amount of tension compression asymmetry, which is indicative of flaw dependent fracture.
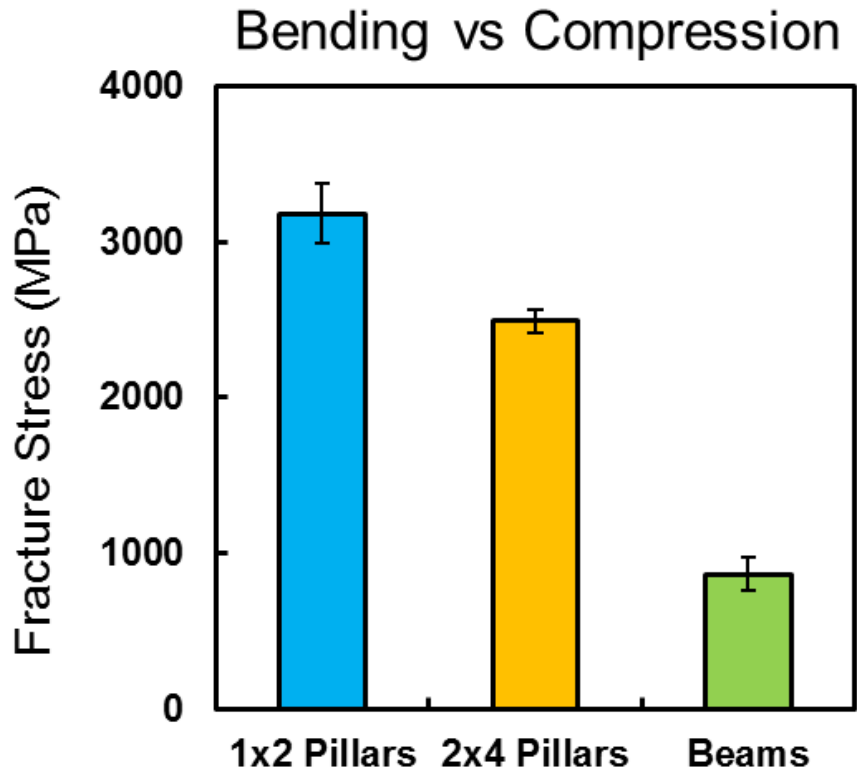
Figure A2. Comparison of compressive strength to flexural strength, showing significantly stronger behavior under compressive loads, which is indicative of flaw dependent fracture.

APPENDIX B

SHEAR STRESS IN CANTILEVER BEAM TESTING

One concern regarding the use of cantilever beams to determine the tensile or fracture toughness behavior is the additional shear stress which develops during bending. The magnitude of this shear stress is dependent on the geometry of the beam and therefore ASTM testing standards for fracture toughness testing using 3 point bending dictate that the sample height be less than 4 times the span (ASTM E1820, 2015). This same $L/W \geq 4$ relation has been adopted in the cantilever beam literature as well (Jaya et al, 2015) as a means of reducing the shear component of the stress. However, noting that $L_{3pt}=2L_{CB}$ by comparing the 3 point bending and cantilever beam geometries as in Chapter 7, a more appropriate equivalent relation for the cantilever beam geometry should be $L/W \geq 2$, as used in Chapter 7 and Appendix A. Using the more conservative relation should yield equally accurate results, but fabricating shorter cantilevers requires significantly less FIB time.

Finite element models were developed in order to determine the relative magnitude of the shear stress as a function of the beam span. A linear elastic 5x5x20 μm cantilever beam was modeled with a modulus and poisson's ratio of 70 GPa and 0.33, respectively. Loads of 3.5, 7, 10.5, and 14 μN were applied at 20, 15, 10, and 5 μm from the beam attachment point, respectively, in order to maintain an approximately equivalent tensile stress (~3 GPa) at the outer fiber. The stress along the length of the beam (σ_{11}) and the shear stress on the beam section (σ_{13}) was measured at the midplane of the beam, as shown in Figure B1. Beams with 20, 15, and 10 μm spans show qualitatively similar behavior with only a small magnitude shear stress. At 5 um span length, the shear stress increases significantly up to approximately 1 GPa (disregarding the stress concentrations at the loading point and beam attachment). Whether or not this shear stress is will affect the fracture behavior depends on the relative magnitude of the shear stress where the beam

fails, which is expected to be at the point of maximum principal stress. For all four span lengths, this point of maximum principal stress still occurs on the top surface of the pillar, where the shear stress must equal zero. This indicates that although there are higher shear stresses associated with shorter spans, the tensile stresses which develop at the top of the beam still dictate the behavior even at relatively short spans (L/W=1).
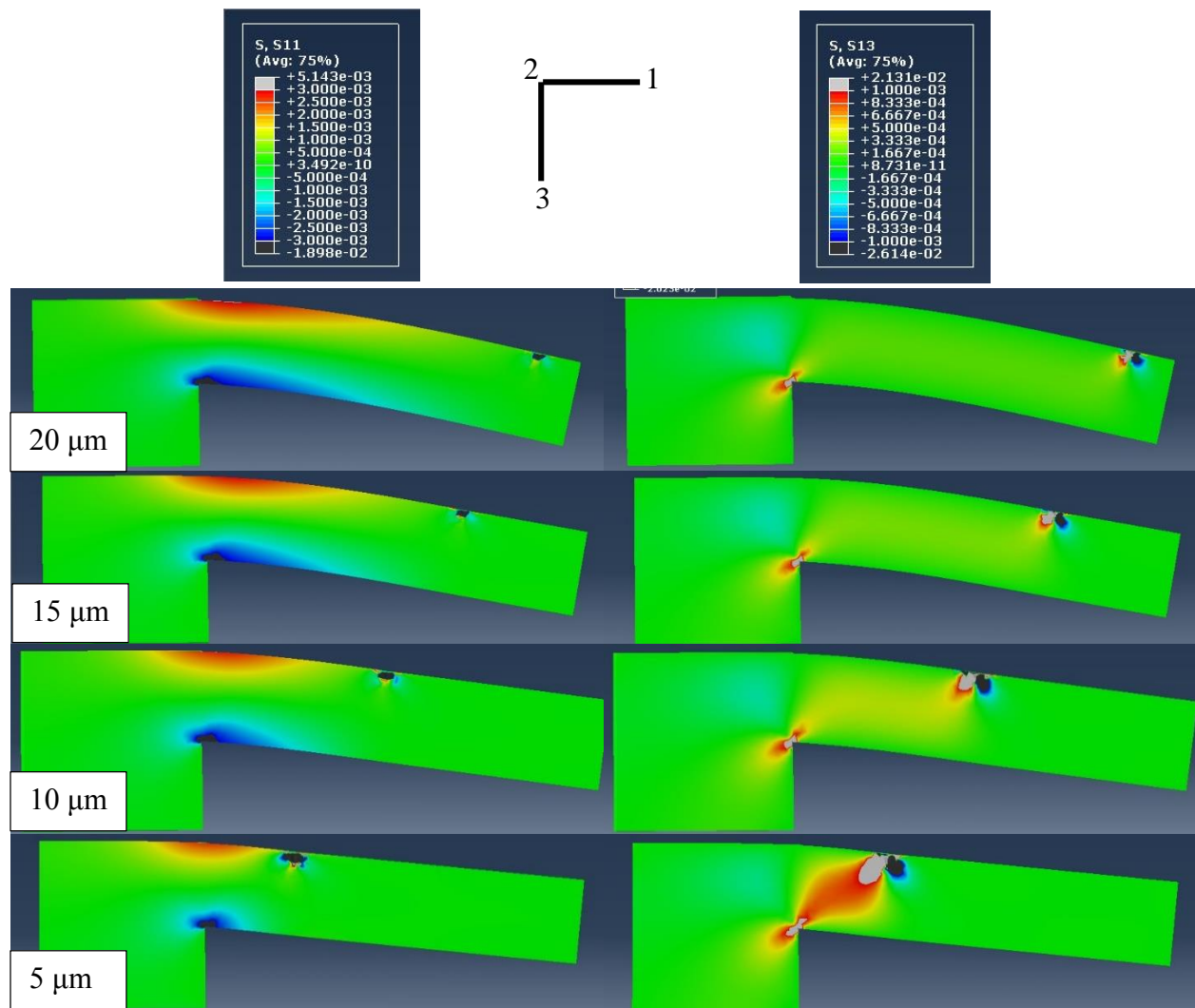

Figure B1. Finite element models showing the effect of the span on the tensile (σ_{11}, left) and shear shear (σ_{13}, right) stresses which develop in the beams, showing minimal differences above 10 μm span.